Neuromuscular junction endplate morphology, acetylcholine receptor aggregation and accessory protein co-localisation during regeneration of a skeletal muscle crush injury

Tayla Sasha Faulmann

Thesis presented in partial fulfilment of the requirements for the degree of Master of Physiological Sciences in the Faculty of Science at Stellenbosch University.

The financial assistance of the National Research Foundation (NRF) towards this research is hereby acknowledged. Opinions expressed and conclusions arrived at, are those of the author and are not necessarily to be attributed to the NRF.

Supervisor: Prof Kathryn H. Myburgh

April 2019

DECLARATION

By submitting this thesis electronically, I declare that the entirety of the work contained therein is my own, original work, that I am the sole author thereof (save to the extent explicitly otherwise stated), that reproduction and publication thereof by Stellenbosch University will not infringe any third-party rights and that I have not previously in its entirety or in part submitted it for obtaining any qualification.

Tayla Sasha Faulmann

February 2019

ABSTRACT

At the neuromuscular junction (NMJ), peripheral nerves innervate the skeletal muscle to relay neural transmission. The acetylcholine receptors (AChRs) are located on the post-synaptic membrane and have auxiliary post-synaptic proteins required for the complex. Rapsyn, MuSK, LRP4 and Dok7 are all involved in ensuring the NMJ functions appropriately. Disruptions to these proteins, the AChRs and the interactions between them occur during various instances of endogenous or exogenous complications.

The current study utilised a contusion injury model and aimed to establish morphology of the skeletal muscle tissue and the post-synaptic NMJ in healthy adult mice before qualitatively and quantitatively assessing the changes that occurred in response to injury. A timeline of muscle function was also assessed at pre- and several post-injury time points.

Mice were split into control (D0) or one of three injury groups that were sacrificed at different time points post-injury, namely after 3 (D3), 7 (D7) or 14 (D14) days. Muscle force/stimulation frequency testing was conducted at baseline and followed immediately by induction of the muscle crush injury in the injury experimental groups. Muscle force testing was conducted again at the respective time points prior to sacrifice.

After severing the aorta, blood samples were collected by draining the thoracic cavity, and plasma isolated for MuSK ELISA analysis. *Gastrocnemius* muscle samples were harvested, mounted on cork either cross-sectionally or longitudinally, and frozen in liquid nitrogen cooled isopentane. Samples were cryo-sectioned and initially stained with haematoxylin and eosin (H&E) to assess morphology. At all four time points, immunohistochemistry (IHC) with combinations of antibodies was used to identify the AChR (α-Btx) co-stained with each associated post-synaptic protein mentioned above.

Fluorescence images were acquired using a confocal microscope and selection criteria were applied to images to identify *en face* NMJs to analyse. Image analysis using ImageJ software assessed the total outlined area (TOA), total stained area (TSA), staining intensity (SI) and co-localisation.

Injury caused a general decrease in force production that was still significantly lower at D14 ($P < 0.0001$). H&E staining confirmed that the contusion injury resulted in substantial destruction to the muscle tissue. Plasma MuSK concentrations rose exponentially in response to injury, peaking at D14 ($P < 0.0001$), confirming damage to the post-synaptic NMJ.

IHC staining established clear co-occurrence and correlation between the AChR and its associated post-synaptic proteins at D0. Co-localisation of the AChR with the post-synaptic proteins was affected severely by injury, with a general trend for a nadir at D3 ($P < 0.01$), before a return to baseline was initiated by D7. Although all four post-synaptic auxiliary proteins responded to injury with widespread dispersion from baseline (both TOA and TSA) and a loss of structure, this was the most severe for LRP4 and MuSK, and least severe for rapsyn. By D14 there was noticeable improvement across protein sub-groups, but least improvement in LRP4.

In conclusion, the contusion injury affected both the structural integrity and functional capacity of the NMJ negatively. Only partial recovery was achieved by D14, and not all auxiliary proteins followed the same time course.

OPSOMMING

Perifere senuwese bewaar die skeletspier-motoriese eenhede by die neuromuskulêre-aansluiting (NMA) om neurale transmissie te herleef. Die asetielcholienreseptore (AChRs) is geleë op die post-sinaptiese membraan en het hulp-na-sinaptiese proteïene wat benodig word vir die kompleks. Rapsyn, MuSK, LRP4 en Dok7 is almal betrokke om die NMJ-funksies behoorlik te verseker. Ontwrigting van hierdie proteïene, die AChRs en die interaksies tussen hulle vind plaas tydens verskeie gevalle van endogene of eksogene komplikasies.

Die huidige studie het 'n kontusie-beserings model gebruik en daarop gemik om kwalitatiewe morfologie van die skeletspierweefsel en die post-sinaptiese NMJ in gesonde volwasse muise te vestig. Veranderinge wat plaasgevind het as gevolg van geïnduseerde besering, was beoordeel. 'n Tydlyn van spierfunksie is ook geassesseer op voor- en verskeie na-beserings tydspunte.

Muise is verdeel in kontrolegroep (D0) of een van drie beseringsgroepe wat op verskillende tydspunte na besering geoffer is. Groepe is geoffer op 3 (D3), 7 (D7) of 14 (D14) dae na besering. Spierkrag/stimulasie frekwensietoetsing is by basislyn uitgevoer en onmiddellik gevolg deur die spierverliesbesering in die beserings eksperimentele groepe. Spierkragtoetsing is weer uitgevoer op die onderskeie tydspunte net voor opoffering.

Nadat die aorta gesny is, is bloedmonsters versamel deur die torakale holte te dreineer, en plasma geïsoleer vir MuSK ELISA-analise. Die *gastrocnemius* spiermonsters is geoes en dwarsdeursnit of lengte gemonteer op kurk. Dit is gevries in vloeibaar stikstofgekoelde isopentaan en dan in afdelings gesny. Die afdelings is gekleur met H & E om die weefselmorfologie te assesseer. Op al vier tydspunte is immunohistochemie (IHC) met kombinasies van teenliggaampies gebruik om die AChR (α-Btx) saamgekleur met elkeen van die geassosieerde post-sinaptiese proteïene hierbo genoem.

Fluorescentie beelde is verkry met behulp van ‘n konfokale mikroskoop. Seleksiekriteria is toegepas op beelde om 'n gesig NMJ te identifiseer om te analiseer. Beeldontleding met behulp van ImageJ-sagteware het die totale uiteenlopende area (TUA), totale gekleurde area (TGA), vlekintensiteit (VI) en ko-lokalisering beoordeel.

Besering het 'n algemene afname in kragproduksie veroorsaak wat nog beduidend laer was by D14 ($P < 0,0001$). H & E-kleuring het bevestig dat die kontusie-besering spiervernietiging veroorsaak. Plasma MuSK konsentrasies het eksponensieel gestyg in reaksie op besering en beriek by D14 ($P < 0,0001$). Dit bevestig skade aan die post-sinaptiese NMJ.

IHC-kleuring het duidelike mede-voorkoms en korrelasie tussen die AChR en sy gepaardgaande post-sinaptiese proteïene by D0 gevestig. Kolokalisering van die AChR met die postsynaptiese proteïene is ernstig geraak deur besering en het beduidend afgeneem by D3. Herstel het by D7 begin. Al vier post-sinaptiese hulpproteïene het gereageer op beserings met uitgebreide verspreiding vanaf hul basislyn (beide TOA en TSA) en 'n verlies aan struktuur. Verspreiding was die ergste vir LRP4 en MuSK, en die minste vir rapsyn. By D14 was daar merkbare verbeteringe in die proteïene-subgroepe, maar die minste verbetering in LRP4.

Ten slotte het die kontusie-beserings negatiewe uitwerkings op beide die strukturele integriteit en funksionele kapasiteit van die NMJ gehad. Slegs gedeeltelike herstel is deur D14 behaal, en nie alle hulpproteïene het dieselfde tydskursus gevolg nie.

ACKNOWLEDGMENTS

To my parents, Maud and Michael, who have gifted me with every opportunity I could have ever hoped for, thank you for never doubting me. You believed and supported my ambitions through any setback I faced and I am eternally grateful for the support system you provided for me. You may never have had the fortune to dream of a future the way I did, but you have always inspired me to pursue a life of success and happiness. What you lack in formal education, you make up for in intelligence, perseverance and passion. This degree is as much yours as it is mine. I love you.

To my partner, Jake, your love has consumed and revived me. I will forever be grateful for the selfless way in which you gave me your time when I was in need. Thanking you for changing the course of my life and allowing me to recognise that it's ok to ask for help. Every moment has been better with you in it.

To my brother and sister, Lucian and Tarryn, you have always and continue to shower me with love and acceptance. Thank you for nurturing a safe space that I can always retreat to.

To my incredible supervisor, Prof. Kathryn Myburgh, your resolute faith in my abilities has kept me going when I doubted myself the most. It is fortuitous that I had the privilege of working under a supervisor as accomplished and respected as you, but I am most thankful for your empathy and kindness. You have shown me what it means to be unapologetic in what you stand for and most of all, to believe in myself.

To Kiran, thank you for selflessly making time to always help when needed. You are incredibly gifted and I wish you all the best in your future in research.

To Tracey and Cameron, your friendship will always be cherished. There were many occasions when your company was instrumental in keeping me going and I appreciate our time spent together.

To Tope, Niccolo, Yigael, Kelly and Jurgen, thank you for always putting a smile on my face and keeping my mind off of science when I needed to. You will all be missed.

To Elré Taai, I am immensely proud of us both. You will go on to do great things. Thank you for being as understanding as you are. You will always be close to my heart.

To Professor Kidd, Lize Engelbrecht, Ashwin Isaacs, Judy Farao and Elizabeth Louw, thank you for technical assistance and always making yourselves available in times of need.

To the MRG, you have made my time spent as a post-graduate fulfilling and enjoyable. Thank you for all the ideas, help, constructive criticism and positive energy that you have given me.

Thank you to the NRF and Stellenbosch University for financial and academic support. Thank you to the NSC and the PPSS for always representing our best interests as Physiology students.

Abbreviations

α-Btx	α-Bungarotoxin
ACh	Acetylcholine
AChE	Acetylcholine Esterase
AChR	Acetylcholine Receptor
ALS	Amyotropic Lateral Sclerosis
ANOVA	Analysis of Variance
AU	Arbitrary Units
AUC	Area Under Curve
BoNT-A	Botulinum Neurotoxin A
BSA	Bovine Serum Albumin
ChAT	Choline Acetyltransferase
CMAP	Compound Muscle Action Potential
CMS	Congenital Myasthenic Syndromes
CNM	Central Myonuclei Myopathies
DAPI	4', 6-diamidino-2-phenylindole
DMC	Dynamic Muscle Control
DNA	Deoxyribonucleic Acid
Dok7	Downstream of Tyrosine Kinases 7
EDTA	Ethylenediaminetetraacetic Acid
ELISA	Enzyme-Linked Immunosorbent Assay
EMG	Electromyography
FFR	Force-Frequency Relation
$\overline{G}$	Mean Intensity of Green Channel
G_i	Specific Intensity of Green Channel, for Pixel i.
H&E	Hematoxylin & Eosin
IgG	Immunoglobulin G
IHC	Immunohistochemistry
LRP4	Low Density Lipoprotein Receptor-Related Protein 4
LSD	Least Significant Difference
LSM	Laser Scanning Microscope
mAChR	Muscarinic Acetylcholine Receptor
MG	Myasthenia Gravis
MMP3	Matrix Metalloproteinase 3
MOC1	Mander's Overlap Coefficient 1
MOC2	Mander's Overlap Coefficient 2

MRFs	Muscle Regulatory Factors
mRNA	Micro Ribonucleic Acid
MuSK	Muscle-Specific Kinase
nAChR	Nicotinic Acetylcholine Receptor
NMJ	Neuromuscular Junction
OCT	Optimal Cutting Temperature
OD	Optical Density
PC	Personal Computer
PCC	Pearson's Correlation Coefficient
PBS	Phosphate-Buffered Saline
PFA	Paraformaldehyde
PNI	Peripheral Nerve Injury
$\overline{R}$	Mean Intensity of Red Channel
R_i	Specific Intensity of Red Channel, for Pixel i.
ROI	Region of Interest
RT	Room Temperature
SD	Standard Deviation
SI	Staining Intensity
TOA	Total Outline Area
TOP	Total Outline Perimeter
TSA	Total Stained Area
UV	Ultra Violet
2D	2 Dimensional

Table of Contents

List of Figures

List of Tables

CHAPTER 1: LITERATURE REVIEW

1.1 Introduction

Human movement relies on the complex relationship and interactions between the nervous system and the muscular system (Eston & Reilly, 2009). These systems in tandem form a circuit consisting of sensory neurons, motor neurons, and skeletal muscle fibres (Ko, 2001). In the simplest of terms, neural outputs generate a desired movement pattern by means of muscular system stimulation (Heckman & Enoka, 2012). This controlled activation of the neuromuscular pathway has been investigated for decades in experimental research (Brazier, 1959) (Karczmar, 1967) (Pick, 1954). The anatomical components of the central and peripheral nervous systems were fairly well established before any consideration was given to the cellular and molecular mechanisms that governed their interactions (Karczmar, *et al*., 2007).

A breakthrough understanding of the neuromuscular pathway's molecular composition was when the nicotinic acetylcholine receptor (nAChR) was first biochemically isolated and characterised. The nAChR is a fundamental element in neuronal communication at the neuromuscular junction (NMJ). Its conversion of acetylcholine (ACh) – a neurotransmitter released at the axon terminal – into the depolarisation of the post-synaptic membrane, facilitates the stimulation of the skeletal muscle contraction by the motor neuron. The nAChR was first described as a protein (Nachmansohn, 1955), before being later characterised by Changeux, Kasai & Lee (1970) as a cholinergic receptor (Corringer & Changeux, 2008).

The NMJ is comprised of several components that occupy the pre-, intra-, and post-synaptic region. The research project will more specifically target the post-synaptic region; hence this chapter will focus on the nAChR and its role in the NMJ, along with its closely associated post-synaptic membrane proteins. Of particular interest is the dynamic expression of the post-synaptic constituents that vary between healthy and diseased/injured states. Literature on models of NMJ injury and pathologies will be included to elucidate current knowledge of the NMJ under these changing conditions. The developmental myogenic path will also be reviewed to determine whether regeneration may follow a similar pattern.

"I move, therefore I am." – (Murakami, 2011)

1.2 The Neuromuscular Junction

1.2.1 Introduction to the NMJ

The motor neurons of the peripheral nervous system innervate the skeletal muscle at a specialised synapse called the neuromuscular junction (NMJ). The NMJ interface is comprised of three distinct zones: pre-synaptic, intra-synaptic and post-synaptic. The pre-synaptic region consists of the motor nerve terminal with its bulb-shaped synaptic bouton. The post-synaptic region refers to the sub-synaptic sarcolemma, a specialised muscle membrane with densely arranged nAChRs. The membrane of the nerve terminal is richly populated with voltage-gated calcium channels and vesicles containing ACh (Punga & Reugg, 2012). Neural signalling is propagated via an action potential along the motor neuron until it reaches the nerve terminal. Choline acetyltransferase (ChAT) synthesises ACh and it is packaged in vesicles stored at the nerve terminal. Voltage-dependent calcium channels are opened, calcium ions flood into the nerve terminal and this subsequently triggers the release of the ACh-filled vesicles into the synaptic cleft (Patton, 2003).

The intra-synaptic region is predominantly comprised of extracellular matrix in the form of the synaptic basal lamina that provides stability to the post-synaptic region (Patton, 2003). This synaptic basal lamina is morphologically identifiable and highly structured (Sanes & Chiu, 1983). The basal lamina creates a sheath around the entire muscle fibre, but the synaptic and extra-synaptic parts of the basal lamina differ in molecular composition and function (Chiu & Sanes, 1984). Junctional folds are created at the NMJ by the basal lamina that invaginate the sarcolemma at this site (Patton, 2003). Therefore, the sub-synaptic sarcolemma is considered to be a specialised part of the muscle membrane and since it is below the neuron and separated from it, it is referred to as the post-synaptic region. Its most striking feature is the densely arranged embedded nAChRs. The folds in which they are situated are vital for increasing the surface area available for neural transmission to be received since they allow for a much larger number of AChRs and their associated post-synaptic proteins.

The nAChR as we know it now was first theorised in 1905 by a physiologist named John Newport Langley. He claimed that muscle tissue possessed a component that "receives a stimulus and transmits it" and subsequently named it the "receptive substance". The following 50 years saw pharmacological, electrophysiological and chemical approaches taken to further elucidate the nature and inner workings of this elusive receptor (Changeux, 2012). Chang & Lee were the first to discover that a toxin found in the venom of a Taiwanese snake (*Bungarus multicinctus*) could cause irreversible neuromuscular blocking effects (1963). This toxin, α-Bungarotoxin (α-Btx), was found to be completely unrelated in structure to ACh, yet still interacted in an identical manner with the cholinergic receptor (Changeux, *et al*., 1970). The discovery of the toxin was vital in allowing further chemical research to be conducted on the AChR.

The AChR structure was further described after the first ever images of a neurotransmitter receptor structure were generated using electron microscopy (Nickel & Potter, 1973). The receptor appeared as ring-like particles surrounding a hydrophilic core (Cartaud, *et al.*, 1973). It was established that it consisted of a number of subunits (five to six) that were closely packed. This depiction would go on to be elaborated on and modified extensively (Unwin, 2005). Soon after the structure was first described, the pentameric arrangement of the subunits was established (Raftery, *et al.*, 1974) (Weill, *et al.*, 1974). The heteropentamer assumed a $2\alpha_1\beta_1\gamma\delta$ formation (Lindstrom, *et al*., 1979) and subunits were divided into four specific types that differed in molecular mass (Saitoh, *et al.*, 1980).

After depolarisation of the nerve terminus, a quanta of ACh molecules get released and move across the synaptic cleft where they bind to the nAChRs on the post-synaptic membrane (Punga & Reugg, 2012). A conformational change in the structure of each AChR occurs when the ACh binds to the receptor's binding site. This chemical reaction is converted back into an action potential as voltage-gated sodium channels adjacent to the folds are opened and allow an influx of sodium (and other cations) ions to depolarise the sarcolemma. The neural action potential is therefore continued on the muscular side of the NMJ and indeed, further propagated away from the NMJ along the sarcolemma.

Also present in the specialised region is acetylcholinesterase (AChE) which hydrolyses ACh once the chemical reaction is converted to prevent prolonged depolarisation of the sarcolemma (Punga & Reugg, 2012). This is how the NMJ acts as the bridge between the nerve and the muscular systems to facilitate effective and reliable communication. However, this bridge is a more complex signalling network that is highly regulated and sensitive to feedback (Gonzalez-Freire, *et al.*, 2014).

1.2.2 Post-synaptic Anatomy

The arrangement of the post-synaptic membrane proteins is complex and has only been elucidated more recently. Muscle specific tyrosine kinase (MuSK), low-density lipoprotein receptor-related protein 4 (LRP4) are transmembrane proteins with synaptic components, while rapsyn and downstream of kinase 7 (Dok7) are sub-synaptic proteins associated with the nAChR. The exact interactions between the molecules have only become a focus in NMJ research recently, opening the door to a whole spectrum of experimental objectives. There are several diagrammatic depictions illustrated by various authors and all differ somewhat from one another.

AChR – As mentioned in Section 1.2.1, the cholinergic receptor activated by ACh (nicotinic AChRs [nAChRs]) is the crucial link in the translation of neural transmission to the myofibre *(*Albuquerque, *et al.*, 2009). Decades of research dedicated to this molecule have paved the way to a good understanding of its significance in the NMJ, as well as NMJ formation and maintenance (Nickel & Potter, 1973) (Raftery, *et al.*, 1974) (Saitoh, *et al.*, 1980).

Table 1.1 nAChR subtypes and their respective types of subunit composition.

Neuronal Subtype					Muscle Subtype
I	II	III			IV
		1	2	3	
α_9, α_{10}	α_7, α_8	α_2, α_3, α_4, α_6	β_2, β_4	α_5, β_3	α_1, β_1, δ, γ, ε

The nAChR (often referenced simply as AChR) directly influences the ion channels of the sarcolemma without the use of second messenger proteins. Due to the direct link, the nAChRs react at incredibly fast rates, often within micro- to sub-micro seconds (Purves, *et al.*, 2011). The nAChR can be divided into neuronal- and muscle type receptors, where the subtypes differ in subunit composition *(Wang, et al.*, 1996). There are seventeen different subunits that exist across both subtypes of the nAChR (see Table 1.1) (Albuquerque, *et al.*, 2009). The muscle type nAChR that will be the primary focus of the research project, consists of four different types of subunits in a symmetric heteropentamer arrangement (Lindstrom, *et al.*, 1979) (Saitoh, *et al.*, 1980). A central pore is created that acts as a cation channel to facilitate membrane permeabilisation (see protein designated purple in Figure 1.2). The $2\alpha_1\beta_1\gamma\delta$ formation is true for foetal mammalian muscle tissue, with the γ subunit substituted for the ε subunit in adult mammalian muscle tissue (see Figure 1.1) (Witzemann, *et al.*, 1991). The ACh-binding site can be found between the α_1 and γ/ε subunits, or the α_1 and δ subunits (Wang, *et al.*, 1996). The receptors are located along the junctional folds of the sarcolemma and often aggregate in clusters (Patton, 2003). They are structurally stabilised by cellular scaffolding, notably rapsyn (see protein designated yellow in Figure 1.2), a sub-sarcolemma anchor protein (Takamori, 2012).

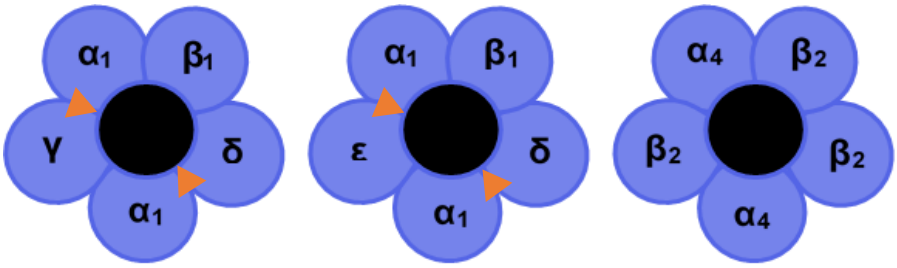

Figure 1.1 nAChR subunit arrangement for adult and foetal muscle type receptors, and the $\alpha_4\beta_2$ neuronal receptor. Subunits are arranged in a heteropentamer structure around a central cation channel. Orange triangles indicate binding sites for ACh located between specific subunits A: The foetal nAChR in $2\alpha_1\beta_1\gamma\delta$ formation. B: The adult nAChR in $2\alpha_1\beta_1\varepsilon\delta$ formation. C: The neuronal nAChR in $2\alpha_4 3\beta_2$ formation. Image modified and reproduced without permission (Wang, et al., 1996).

Rapsyn – As previously mentioned, rapsyn is a cytoplasmic membrane-associated scaffolding protein of importance that is vital in the maintenance of AChR structural integrity and subsequent function. Rapsyn is critical in AChR clustering and post-synaptic cytoskeletal organisation (Apel, *et al.*, 1997) (Ramarao, *et al.*, 2001). It was originally named the 43K protein and was shown to co-localise precisely with the AChR in vivo (Froehner, *et al.*, 1981) (Sealock, et al., 1984). Rapsyn binds to the cytoplasmic domains of the AChR (Ramarao, *et al.*, 2001) and is estimated to be distributed in an approximately 1:1 stoichiometry with the receptor (Brockhausen, *et al.*, 2008). Interestingly, rapsyn is present at the intracellular synaptic site of foetal AChR clusters immediately as they form (Noakes, *et al.*, 1993). In contrast, rapsyn knock-out mice are unable to form AChR clusters (Gautam, *et al.*, 1995).

Literature also points to a direct relationship between the supply of rapsyn at the synaptic site and the number of AChR clusters (Brockhausen, *et al.*, 2008) (Gervasio & Phillips, 2005) (Martinez-Martinez, *et al.*, 2009). The molecular mechanisms that rapsyn employs to localise the AChR has yet to be elucidated and its precise site of interaction on the receptor is unknown (Lee, *et al.*, 2009).

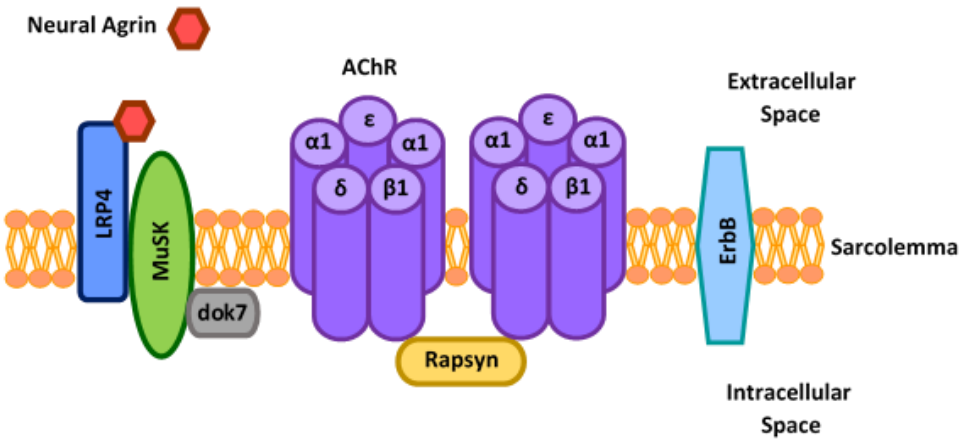

Figure 1.2 nAChR and its associated post-synaptic components of the NMJ. The muscle type nAChR forms a heteropentamer cation channel at the sub-synaptic sarcolemma. It is stabilised by the intracellular anchor protein, rapsyn. LRP4 and MuSK are transmembrane proteins that regulate NMJ formation, clustering and maintenance. Neural agrin binds directly to the LRP4 which acts as a co-receptor to MuSK. MuSK activation and downstream signalling is also facilitated by Dok7, an intracellular adaptor protein. Erb tyrosine kinases (ErbB) initiate AChR recycling. Image modified and reproduced without permission (Lewis, 2013).

MuSK – Like rapsyn, the transmembrane muscle-specific receptor tyrosine kinase is responsible for formation and stabilisation of NMJs (Hubbard & Gnanasambandan, 2013). At first it was thought to be selectively expressed in skeletal muscle (Valenzuela, *et al.*, 1995); however, it has since been found to be expressed in other mammalian tissues as well, including central nervous system neurons and sperm (Garcia-Osta, *et al.*, 2006) (Kumar, *et al.*, 2006). In addition to its role in the sub-synaptic complex (see protein designated green in Figure 1.2), it also regulates gene transcription in sub-synaptic nuclei *(Strochlic, et al.*, 2005).

MuSK activation is complex and involves numerous other synaptic proteins. Neural agrin, a glycosylated proteoglycan derived from the motor neuron, is the neural signal responsible for phosphorylation and subsequent activation of MuSK (Kim & Burden, 2008). Downstream signalling results in re-organisation of the actin cytoskeleton and AChR cluster recruitment (Glass, *et al.*, 1996) (Strochlic, *et al.*, 2005). Thus, the neural agrin/MuSK pathway is responsible for stabilising AChR clusters at the NMJ (Gervásio, et al., 2007). Although neural agrin was first thought to be a ligand for MuSK, no direct interaction between agrin and MuSK has been proved (Glass, *et al.*, 1996). This led to the discovery of LRP4 as key component of the agrin-MuSK activation complex.

LRP4 – Another relevant transmembrane protein is a member of the low density lipoprotein receptor (LDLR) family and acts as a receptor for agrin with this complex then influencing MuSK activation (Zhang, *et al.*, 2008). As such, it has a vital role in the agrin/MuSK signalling pathway for NMJ development, and further roles identified include involvement in the development of the limbs, lungs, kidneys and ectodermal organs (Johnson, *et al.*, 2005) (Simon-Chazottes, *et al.*, 2006). Its expression is concentrated at the NMJ and neural agrin binds directly to the extracellular domain of LRP4 (see proteins designated red and blue in Figure 1.2).

LRP4 and MuSK can interact in the absence of agrin, but agrin behaves as an allosteric regulator and creates an enhanced interaction of the LRP4/MuSK complex (Zhang, *et al.*, 2008). This basal interaction is sufficient for partial continuous activation of MuSK. Decreased LRP4 expression creates a knock-on effect of decreased agrin binding, MuSK activation and AChR clustering (Hubbard & Gnanasambandan, 2013). Integral to the agrin/LRP4/MuSK axis is another protein Dok7 (Punga & Reugg, 2012).

Dok7 – Classified as a cytoplasmic adaptor protein, Dok7 is expressed in the heart and, more notably, at the NMJ of skeletal muscle (see protein designated grey in Figure 1.2) (Muller, *et al.*, 2010). It performs a dual role as an upstream activator and a downstream substrate of MuSK (Hubbard & Gnanasambandan, 2013). Together neural agrin, LRP4, MuSK and Dok7 create a signalling cascade that is vital in AChR clustering at the post-synaptic membrane.

The dual activation of MuSK from the inside (Dok7) and outside (agrin/LRP4) allows for different degrees of MuSK activity. Non-agrin mediated MuSK activation that occurs intracellularly via Dok7 represents basal MuSK activity. Activation of MuSK by neural agrin is also impaired when there is a lack of Dok7 present at the synapse (Inoue, *et al*., 2009). Dok7 gene mutations result in defective NMJ structure, and not only a decreased AChR density as a result of decreased gene regulation. This could allude to Dok7 having a more complex functional role in NMJ development and maintenance (Muller, *et al*., 2010).

1.2.3 Formation and Maintenance of the NMJ

Due to the complex nature of synaptic transmission, developmental synaptogenesis involves an elaborate process of pre- and post-synaptic arrangement and rearrangement until optimal structure is achieved. The primary objective during synapse formation is to generate regions of densely packed AChRs that will subsequently be effectively innervated by pre-synaptic nerve terminals (Cossins, *et al*., 2006). The AChRs are distributed across the entirety of the sarcolemma, with synaptic AChRs only occupying around 1% of the total sarcolemmal surface area but constituting 90% of the muscle's AChRs (Colledge & Froehner, 1998). This synaptic region is densely populated with nAChRs clusters of 10 000 – 20 000/μm^2, whereas the remaining 99% of the sarcolemma has a cluster density of around 10/ μm^2 (Gervásio, *et al.*, 2007). Apart from their distribution patterns, synaptic AChRs are also more metabolically stable than their non-synaptic counterparts, with sub-synaptic myonuclei transcribing AChR genes at faster rates (Punga & Reugg, 2012).

Recent literature on synaptogenesis has challenged the previously believed notion that the pre-synaptic motor neuron dictates where AChR clustering occurs and therefore that the motor neuron induces post-synaptic differentiation. New findings have suggested that partial activation of MuSK, even without agrin, is responsible for pre-patterning of AChR clusters and that this occurs before innervation (Arber, *et al*., 2002) (Kummer, *et al.*, 2006). MuSK gene expression and location at the basal lamina is itself independent of innervation and its spatial pattern dictates where synapses may form. This intrinsic muscle pre-patterning via cytoplasmic activation of MuSK is said to influence the final growth pattern of motor axons and therefore to control innervation sites (Arber, *et al*., 2002).

The release of neural agrin by motor neurons attracted to pre-patterned sites initiates a signalling cascade that also activates MuSK (as previously described in section 1.2.2) and results in further AChR clustering and stabilisation (Cossins, *et al*., 2006). This dual activation of MuSK, both independent and dependent of the release of neural agrin by nerve terminals, is key for final AChR clustering *(Okada, et a*l., 2006). Effective synaptic transmission requires both synaptic clustering and concurrent innervation.

Synaptogenesis furthermore requires a combination of positive signals that promote the stabilisation of the newly formed NMJ, and negative signals that disperse and recycle AChRs that do not form an effective connection (Lin, *et al*., 2005). The extensive sources and mechanisms of both positive and negative signals have yet to be elucidated; however, literature suggests that the navigating nerve during early development may provide both positive and negative signals (Lin, *et al*., 2001).

ACh itself has been suggested as a possible negative signal via a pathway independent of MuSK (Lin, *et al*., 2005) (Punga & Reugg, 2012). Lin *et al*. described ACh release as being responsible for disassembling the post-synaptic apparatus that were unable to form stable connections with pre-synaptic nerve terminals (Lin, *et al*., 2005). Although neural agrin is not responsible for prepatterning on the muscle fibre side of the NMJ, it was identified as a positive signal promoting pre-synaptic specialisation of nerve terminals and along with the LRP4/MuSK/Dok7 signalling complex to play a role in stabilisation of the pots-synaptic apparatus (Gautam, *et al*., 1996).

Due to its role as an activator and a substrate, Dok7 is necessary for both pre-clustering of AChRs facilitated via cytoplasmic MuSK activation, and for subsequent neural agrin-induced AChR clusters (Okada, *et al*., 2006). Neural agrin-induced MuSK activation is carried out extracellularly upon innervation of the muscle to bring about AChR clusters (Muller, *et al*., 2010). Once clustering is achieved, post-synaptic stabilisation occurs as a result of AChRs anchoring (Bezakova & Reugg, 2003) (Campagna & Fallon, 2006). Secreted agrin binds to laminin-221 in the intra-synaptic cleft to facilitate incorporation into the extracellular basal lamina (Punga & Reugg, 2012). Neurotrypsin, a serine protease, then targets neural agrin and renders it inactive by cleaving it at two sites and initiating the disassembly of the adult NMJ (Bolliger, *et al.*, 2010). This local cleavage at the synapse suggests that neurotrypsin/agrin cycling is vital in regulating synaptic reorganisation (Stephan, *et a*l., 2008).

The direct binding of rapsyn to the AChR on the intracellular side is also essential in facilitating stabilisation (Gautam, *et al*., 1995) (Ramarao, *et al*., 2001). An interaction between MuSK and rapsyn has therefore also been postulated, as both MuSK activation and rapsyn are vital in maintaining synaptic structure and AChR aggregation (Sanes & Lichtman, 2001). As previously described, the C-terminus of neural agrin binds to the extracellular domain of the LRP4 (Zhang, *et al*., 2008). Agrin behaves as an allosteric regulator of the LRP4/MuSK complex, and its binding to LRP4 subsequently induces a conformational change. LRP4 acts as a co-receptor providing a mechanism for agrin to activate MuSK, so that this agrin-induced activation of MuSK results in subsequent phosphorylation events (Hubbard & Gnanasambandan, 2013). While Dok7 may function as a cytoplasmic activator of MuSK, its role in the agrin-dependent signalling pathway is that of a downstream substrate of MuSK (Inoue, *et al*., 2009) (Muller, *et al*., 2010).

In developing synapses, the AChR complex is notably less stable when compared to its mature counterpart (Fambrough, 1979). The developing NMJs undergo dramatic restructuring, and continuous renovation at the basal lamina supports the notion that the synaptic basal lamina is not assembled as a unit, but rather that components may be added, removed or modified during the formation and maintenance of the NMJ (Chiu & Sanes, 1984). Young AChRs are discarded on the basis of their activity with pre-synaptic factors (Gervásio, *et al*., 2007). However, AChRs at newly formed synapses are clustered and stabilised at a rapid turnover rate, while the AChR turnover rate in mature synapses is relatively slow, so that the adult NMJ takes on a morphology that is quite different from that of the early postnatal days (see Figure 1.3) (Fambrough, 1979) (Shi, *et al*., 2012).

Functional neural transmission is required for the final adaptation of muscle-specific synapses (see Figure 1.3) that are capable of responding to altered synaptic activity states (Santos & Caroni, 2003). These altered states include denervation and pharmacological toxins such as Botulinum Toxin A (Bruneau, *et al*., 2005).

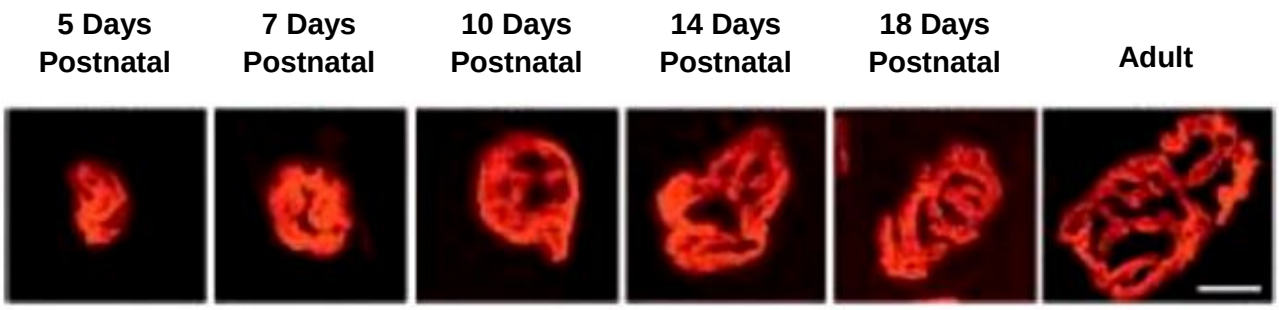

Figure 1.3 Morphological changes in the NMJ of a mouse from 5 days postnatal. The morphology of early postnatal AChRs labelled with α-Btx (red) was documented over the first three postnatal weeks. The AChR appears to transform from a dense oval-shaped structure to the distinct coral-like architecture by the time it reaches maturation. Scale bar = 10μm. Image modified and reproduced without permission (Shi, *et al.*, 2012).

Postnatal stabilisation of the AChRs relies on appropriate pre-synaptic overlapping morphology so that signalling can occur adequately and efficiently (see Figure 1.4) (Mori, et al., 2017). Extra-synaptic AChRs are dispersed and discarded if there is a lack of effective transmission (Shi, *et al*., 2012). The mature and stabilised endplate does not continuously express the receptor proteins' mRNA at full capacity, however the muscle cell is able to regulate expression in response to stimuli (denervation etc.) (Yampolsky, *et al.*, 2010).

Endplate restructuring and AChR recycling are still present in mature synapses, particularly in response to events such as disease and denervation. In adult muscle tissue, motor neurons that are disconnected from their respective muscle fibre as a result of injury to the peripheral nerve, have the ability to regenerate and reconnect with the muscle fibre. Once axons locate the previous site of innervation, remodelling of the synapse occurs. The extent of remodelling is controlled by the time taken for reinnervation to take place. If reinnervation is fast enough only minor remodelling occurs, otherwise it may be a long and extensive process (Kang, *et al*., 2014).

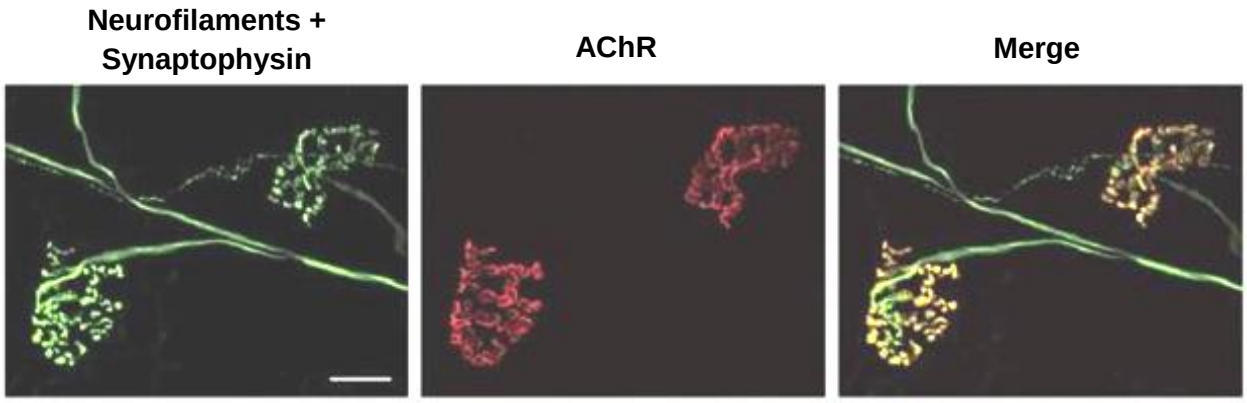

Figure 1.4 Axons and nerve terminals stained in conjunction with the post-synaptic AChR. Whole *soleus* muscles from mice were mounted for staining. Pre-synaptic axons and the membranes of synaptic vesicles at nerve terminals labelled using anti-neurofilament and anti-synaptophysin antibodies respectively and green fluorescent secondaries. AChRs labelled with α-Btx conjugated to rhodamine (red). Scale bar = 20μm. Image modified and reproduced without permission (Mori, *et al*., 2017).

In contrast, when damage occurs to the post-synaptic membrane that results in subsequent denervation, rapid reinnervation is more likely to occur. Notably, the regenerated synapse has a distinct new morphology. While the nerve terminal remains intact during the post-synaptic degeneration, it too begins to change its morphology once the synapse begins to regenerate (Li & Thompson, 2011). Hence, regardless of the method of denervation, reinnervation appears to involve the development of new synapses at the original synaptic sites on the post-synaptic membrane (Kang, *et al.*, 2014) (Yampolsky, *et al*., 2010).

1.3 NMJ Injury Models

Various models of peripheral nerve and/or NMJ injury have been utilised in an effort to better understand the mechanisms of regeneration and the potential of therapeutic strategies (Pratt, *et al*., 2013) (Shen, *et al*., 2006). Injury to either the pre- or post-synaptic components, or both, impairs neuromuscular transmission and can decrease voluntary muscle function. A return to normal function over time is expected in most cases due to the functional plasticity that is maintained to a certain extent from development to maturation (Magill, 2009).

This allows for continual remodelling in response to changes in the NMJ niche (Ferre, et al., 1987). These include endogenous changes such as ageing (Jang & Van Remmen, 2006) and disease states (Kulakowski, *et al*., 2011), or exogenous challenges such as mechanical injury (Kawabuchi, *et al*., 2011), toxins (Shen, *et al*., 2006) or physical activity levels (Fahim, 1997) (Wilson & Deschenes, 2005). A return to normal function over time is expected in most cases and the components of the NMJ affected can be monitored by replicating the challenges using various *in vivo* models (Li & Thompson, 2011).

Rodent models are most often favoured due to the cost effectiveness of housing and feeding small animals as opposed to larger mammals (Alvites, *et al*., 2018). While the rat model is preferred over the mouse model due to its larger dimensions and greater ease of handling, the mouse model is useful in attaining specific outcomes that rely on the use of genetically modified animals (Tos, *et al*., 2009). However, both species of rodents have an extremely high neuroregenerative capacity in comparison to humans where neuroregeneration is relatively poor. This makes translation difficult in the case of therapeutic strategies (Myckatyn & Mackinnon, 2004).

1.3.1 Pre-synaptic Nerve Injury

Peripheral nerve injury (PNI) models can be defined as those that induce pre-synaptic trauma to the NMJ. They are effective in eliciting an adaptive response at the NMJ, and they hold practical relevance since PNI are often seen in a clinical setting (Menorca, *et al.*, 2013). Various PNI models are used and produce different kinds of injuries, with a spectrum of pathophysiological symptoms and biological consequences (Alvites, *et al.*, 2018).

The extent of the injuries sustained in clinical settings or induced by the different experimental models can be described by categorising the grade of injury. The first classification system was established in 1943 by Seddon and took into consideration the degree of damage sustained by the axons and by the tissues that enclosed them (Seddon, 1943).

Neuropraxia **–** The first class in Seddon's grading system is the mildest form of PNI, specifically with no loss of nerve continuity occurring (Seddon, 1943). While anatomical integrity of the motor neurons is usually maintained with no disruption to the axons, the myelin sheath may be damaged. Although these injured nerves may remain intact, they still become dysfunctional and lose their ability to effectively transmit electrical impulses. Impaired muscle function may occur as a result of the transmission interference, but once the compressive force that is used to induce the myelin damage is removed from the site of the nerve injury, complete recovery is expected (Choi, *et al*., 2016). This recovery process can last from a few days to weeks for the structural integrity and functional capacity to fully return.

Axonotmesis **–** The second class of the grading system refers to crush injuries and usually entails a disruption in both the axon and myelin sheath (Seddon, 1943). The outer connective tissues of the peripheral nerve are generally preserved and ensure the anatomical shape of the nerve is maintained. One can expect a good prognosis from this class of PNI and complete recovery is also expected. The time course of repair is dependent on the degree of disorganisation within the nerve and the distance from the site of injury to the target organ (Burnett & Zager, 2004).

Neurotmesis **–** The third class of injury is characterised by a total separation of two portions of the affected nerve, with disruption to the axon, myelin sheath and all connective tissue layers (Seddon, 1943). The disconnection of the nerve results in total functional loss as transmission cannot be relayed to the muscle tissue. Due to the loss of the collagen-rich connective tissue and its guiding role in the regrowth of the axon, the normal regenerative sequence is impaired. As a result, surgical intervention is inevitable before any reversible damage can repair (Campbell, 2008). This type of injury is usually caused by injection of toxic substances (Botulinum Toxin A), excessive pulling forces (eccentric contractions) or penetrating injuries (lacerations) (Alvites, *et al*., 2018).

Modified classification systems were also later introduced to expand on the 3 categories already described (see Figure 1.5) (Alvites, *et al.*, 2018). In 1951 Sunderland proposed a classification system with 5 categories, where the axonotmesis injury was divided into 3 further sub-divisions (Sunderland, 1951). Finally, in 1988 Mackinnon and Dellon suggested an additional 6th category that included mixed injuries (Mackinnon & Dellon, 1988). This last degree of injury takes into consideration that a single nerve can present with different distinct types of damage throughout its length. This is often the case in bone fractures that occur near peripheral nerves or in penetrating traumas (Chhabra, *et al*., 2014).

In animal experimental models, different classifications of pre-synaptic nerve injury are studied according to the manner in which the injury is induced. Typically, the nerve is either crushed or transected.

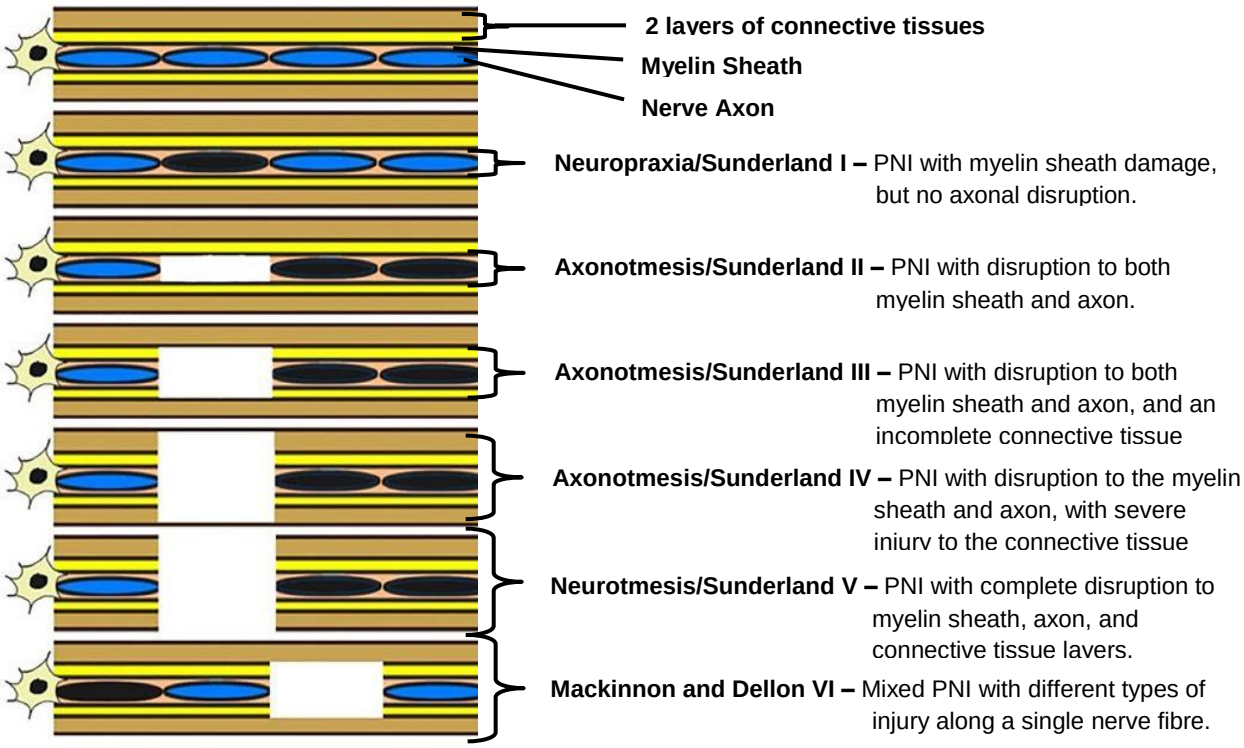

Figure 1.5 Schematic representation of the Seddon, Sunderland, and Mackinnon and Dellon grading systems for a peripheral nerve injury. Image modified and reproduced without permission (Alvites, *et al.*, 2018).

1.3.1.1 Nerve Crush Injury Models

Experimentally; induced nerve crush injuries can present with the characteristic markers of any of the injury grading categories (Seddon, 1943) (Sunderland, 1951). However, nerve compression is generally limited to neuropraxia or axonotmesis (Burnett & Zager, 2004). Interruption of the axon is expected, accompanied by maintenance of the surrounding connective tissue (Sarikcioglu, *et al.*, 2007). Rodent models that utilise the nerve crush injury rely on an acute traumatic compression of the nerve, usually administered by clamp or forceps, which does not result in complete transection (Menorca, *et al.*, 2013). Crushing lesions are less severe than complete nerve transection due to the surrounding connective tissue and sometimes the myelin sheath remaining intact (Zimmerman & Granger, 1994). When the crushing force is relatively low, the extent of injury is dependent on the duration of the applied compressive forces (Algora, *et al.*, 1996). Short-term paralysis may be experienced when the duration of crushing is around 10 minutes. However, anything within the range of 2 to 6 hours may induce long-term paralysis (Schmelzer, *et al.*, 1989).

Several surgical models of nerve crush injury have been developed over the years that make use of a number of different surgical instruments (Bain, *et al*., 1989). Haemostatic forceps were one of the first instruments used in nerve crush injuries, however they were unable to provide exact quantification of force produced. Tourniquets have also been used to induce injury, and while they are quantitative, they do not provide a direct compressive force to the nerve (Chen, *et al.*, 1992).

A compression box was eventually developed to control the magnitude and duration of the application of the crushing force (Rydevik & Lundborg, 1977). First established in larger animal models like the rabbit, the compression box was later adapted to cater to the smaller dimensions of the rat (Chen, *et al.*, 1992). In 2001, a medical research group from Switzerland developed a device that was able to apply predetermined forces to nerves with a non-serrated clamp (Beer, *et al.*, 2001). Both the force exerted, and duration of the crush could be controlled and therefore the clamp was able to produce standardised and reproducible injury conditions (Ronchi, *et al.*, 2009). The clamp is now commercially available and has been successfully applied in several different nerve injury studies, most notably the sciatic nerve injury model in rats (Varejão, *et al.*, 2004).

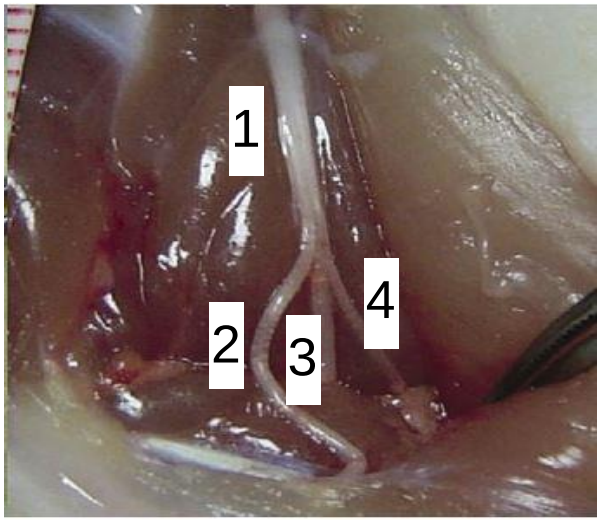

Figure 1.6 Identification of the sciatic nerve and its terminal branches in a Wistar rat. 1: The sciatic nerve. 2: The fibular nerve. 3: The tibial nerve. 4: The sural nerve. Image modified and reproduced without permission (Silva, *et al*., 2010).

Most studies in animals utilising the nerve injury model rely on the sciatic nerve and its terminal branches due to its large size (see Figure 1.6) and the numerous functional tests available for the nerve (Ronchi, *et al*., 2009). Induced nerve compression of the sciatic nerve is one of the most commonly performed nerve crush injuries, however the femoral (Robinson & Madison, 2009), tibial (Apel, *et al*., 2009) and peroneal (Alluin, *et al*., 2009) nerves have also been explored as alternative options.

The sciatic nerve is accessed through precise dissection of the gluteal muscles and application of soft tissue retractors, before it is suitably exposed (see Figure 1.7 A) (Alvites, *et al.*, 2018). The crush is then administered according to the desired method (see Figure 1.7 B). The crushed area of the nerve appears flattened, but still intact following the induction of the injury (see Figure 1.7 C) (Tos, *et al.*, 2009). A disadvantage of this technique is the major invasiveness of the surgical procedure which could have local side effects. An advantage is that the contralateral limb is usually not operated on and may be used as a control (Ozturk, 2015).

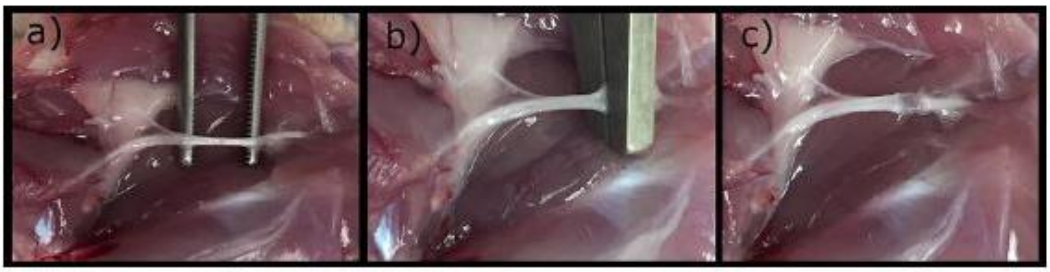

Figure 1.7 Induction of an axonotmesis injury in sciatic nerve of Wistar rat. A: Sciatic nerve isolated from surrounding tissues. B: Compressive force applied to nerve to induce crush injury. C: Anatomical flattening of sciatic nerve post-injury. Image reproduced without permission *(Alvites, et al.*, 2018).

1.3.1.2 Nerve Transection Models

Nerve transection injuries differ from nerve crush injuries in that they are categorised as neurotmesis and are characterised by complete disconnection of the nerve and its surrounding connective tissue (Menorca, *et al.*, 2013). Transection of the peripheral nerve leads to destruction of the axon with accompanying systemic responses (Vargas & Barres, 2007). Following denervation, distinct differences in muscle samples can be seen when compared to the innervated counterparts. AChRs are more widely dispersed, but due to the fragmented appearance the actual volume covered by AChRs is decreased (Chan, *et al.*, 2017). Neurogenic atrophy also occurs in the skeletal muscle tissue as fibres shrink and hypertrophy is prevented, along with other morphological changes (Krarup, *et al.*, 2016). The extent of these changes is dependent on the time period of denervation. The extent and time course of degeneration is also dependent on timing of harvesting denervated muscle samples (Chan, *et al.*, 2017). When the duration of denervation is prolonged, AChRs redistribute along the post-synaptic membrane of the muscle fibre (Kang, *et al.*, 2011). This disrupts the usual regeneration pattern after denervation.

As mentioned before, the peripheral nervous system retains its ability to regenerate components following injury. Peripheral motor neurons separated from the muscle fibre generally regenerate their axons by following the pre-existing endoneural tubes (Nguyen, *et al.*, 2002). Newly established axon terminals are attracted to the original synaptic sites; however, the post-synaptic components must also undergo remodelling once reinnervated, hence muscle regeneration is delayed (Balice-Gordon & Lichtman, 1994). Functional recovery in adult humans remains limited once neural repair is completed (Kang, *et al*., 2011) and it has been suggested that this incomplete functional recovery could be attributed to motor endplate degradation following denervation with a relative lack of subsequent remodelling ability (Kang, *et al.*, 2014). Therefore, it remains important to continue with research on the regeneration of the post-synaptic aspect of the NMJ. Nevertheless, even when considering mainly the post-synaptic aspect, the type of nerve injury model used will influence regeneration process.

Nerve transection injuries, much like nerve crush injuries, are predominantly conducted on the sciatic nerve and its terminal branches (Pavic, *et al.*, 2011). There are various versions of sciatic nerve transection injury that aim to address different objectives within the field of regenerative research. The effects of different times of reparative intervention can be assessed by comparing a model that induces nerve injury and then immediately repairs it as part of the experimental intervention (e.g. with sutures or fibrin glue) (Silva, *et al.*, 2010) (Sakuma, *et al*., 2016) (Sarica & Altun, 2018) versus a model that severs the nerve and leaves it as is with no nerve repair (only wound closure) (Guo, *et al.*, 2018).

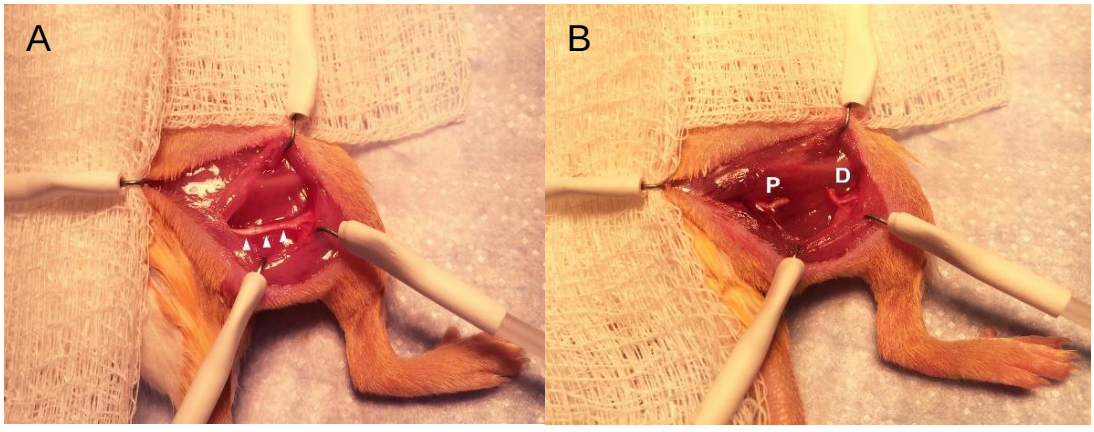

Figure 1.8 Nerve transection of the sciatic nerve of Wistar rat. A: Sciatic nerve along the femur exposed. B: 5 mm segment of nerve removed during transection injury. The proximal sciatic nerve stump is indicated by P and the distal sciatic nerve stump by D. Image modified and reproduced without permission (Mohammadi, *et al.*, 2016).

Nerve injury and repair models include variations to how the nerve is repaired. Repair can be carried out via end to end anastomosis (Cheng, *et al.*, 2015) (Sakuma, *et al.*, 2016) (Sarica & Altun, 2018) or end to side anastomosis (Silva, *et al*., 2010). Some experimental nerve injuries without repair may even conduct a complete removal of a small (usually 10 mm) section of the nerve (see Figure 1.8) *(Chao, et al*., 2013) (Ikeda & Oka, 2012) (Mohammadi, *et al.*, 2016).

As mentioned earlier, the use of mice allows for development of transgenic models that focus on the role of a particular protein in the regeneration process. Chao *et al*. carried out a denervation study comparing the responses of wild-type and matrix metalloproteinase 3 null (MMP3) mice (Chao, *et al*., 2013). A 10 mm segment was excised from the right sciatic nerve of 6 week old male mice. AChR degradation progressively worsened, coupled with increased AChR dispersion over time following denervation (see Figure 1.9) (Chao, *et al*., 2013). For the purpose of this thesis, MMP3 was not a main focus, but the assessment methods used by Chao *et al*. were found to be informative.

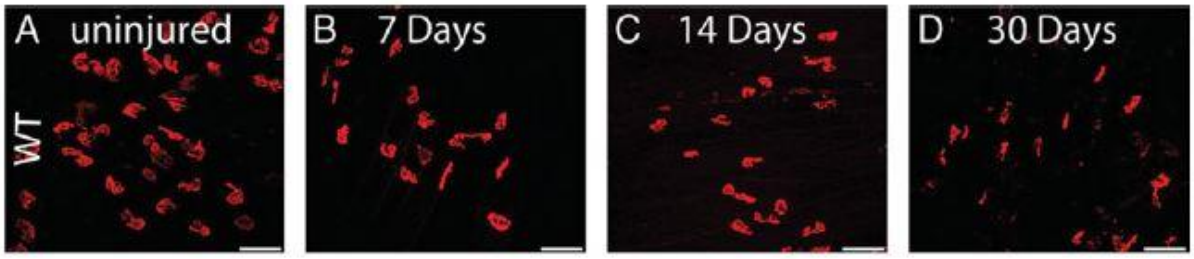

Figure 1.9 Wild-type mouse skeletal muscle tissue stained with α-Btx (red) to label AChRs following nerve transection injury. A – D: Images of AChRs at baseline and various time points post-denervation. 40X magnification; scale bars = 15 μm. Image reproduced without permission *(*Chao, *et al*., 2013).

AChR area and pixel density were calculated and comparison was made between the wild-type and MMP3 groups over time following denervation. AChR area and pixel density both decreased post-denervation in the wild-type group where the lowest percentage of the respective variables were seen at 30 days post-injury (see Figure 1.10). This indicated that AChRs complexes decreased in size and the pixel intensity of AChR staining also decreased over the same time course following denervation. The MMP3 group appeared to exhibit a protective element when compared to the wild-type group (see Figure 1.10) (Chao, *et al.*, 2013).

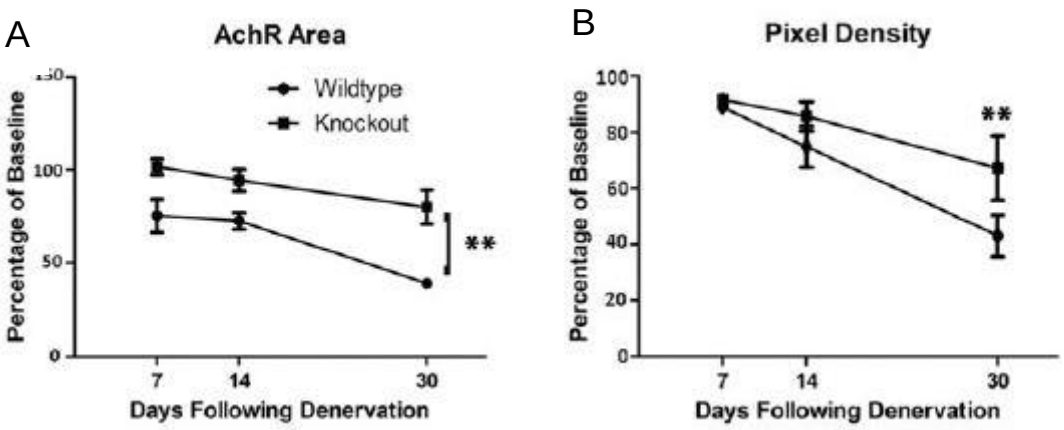

Figure 1.10 AChR area and pixel density over time of wild-type and MMP3 null mice following nerve transection injury. A: AChR stained area in the wild-type and MMP3 groups at baseline and various time points post-denervation. B: Pixel density (stained area/staining intensity) in the wild-type and MMP3 groups at baseline and various time points post-denervation. **p < 0.01. Image reproduced without permission (Chao, *et al*., 2013).

1.3.2 Biological Toxins

Botulinum toxin is a neurotoxic protein produced by the bacterium *Clostridium botulinum* that has been widely used in methods of investigating the process of neuronal plasticity. The toxins have the unique ability to eliminate neurotransmission by preventing the pre-synaptic release of ACh into the intra-synaptic space, while the viability of the nerve endings remains unchanged (Meunier, *et al*., 2003). As a result, they are useful in the management of conditions that cause skeletal muscle spasticity and joint contractures, such as cerebral palsy (Koman, *et al*., 2001), and are also used for cosmetic purposes.

There are seven botulinum neurotoxin classes that have been identified and labelled from A to G. Type A and B are the more commonly used types of the botulinum toxin for medical and cosmetic purposes in humans (Singh, 2006). BoNT-A is administered via an intra-muscular injection. The toxin is taken up by the pre-synaptic nerve terminal via endocytosis and prevents the ACh vesicles from being released and docking to the post-synaptic site (see Figure 1.11) (Eleopra, *et al*., 1998). This inhibition of ACh signalling causes degeneration of the NMJ and a reduction in force generation by the muscles. Neuroparalysis and denervation occur as a result of the impaired ACh pathway (Arnon, *et al.*, 2001). Both muscle mass and force were significantly reduced at one to two weeks post injection (Ma, *et al*., 2004).

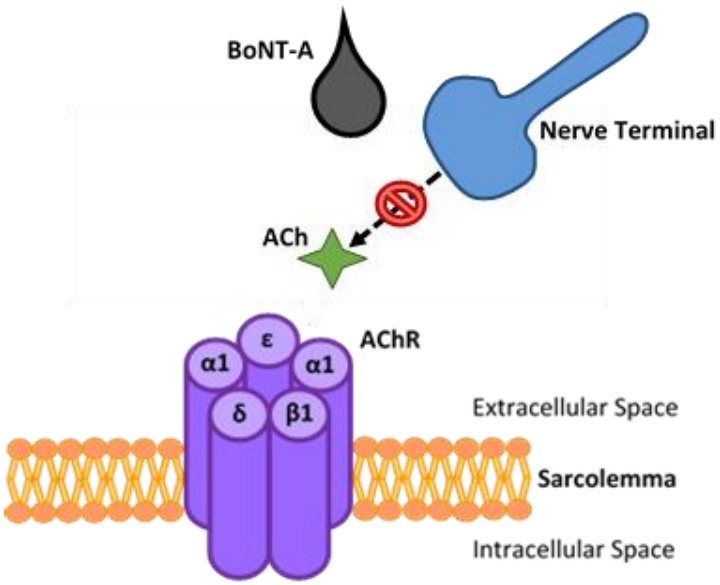

Figure 1.11 BoNT-A blocks release of ACh.

Animal studies have shown that the extent of damage elicited to the NMJ occurs in a dose-dependent manner. Depending on the dose, the BoNT-A injection caused a 30% to 70% reduction in muscle mass, as well as a reported 30% to 90% reduction in muscle force production (Tsai, 2013). Interestingly, BoNT-A injections also caused structural damage and a decrease in muscle mass of contra-lateral and non-injected peripheral muscle (Dressler & Benecke, 2003). As a result, the use of the contra-lateral limb as a control is not possible when using this model. According to Fortuna *et al*. both the muscle mass and muscle force production were decreased in the non-injected contra-lateral quadriceps muscles of New Zealand White rabbits (Fortuna, *et al*., 2011).

The NMJ regeneration required for post-injury stabilisation and a return of muscle function is initiated by the genes that control myogenesis and NMJ remodelling (Shen, *et al*., 2005). MRFs, MuSK, p21 and the AChR subunits' mRNA are all implicated in the repair process (Hamjian & Walker, 1994). The degenerative effects of BoNT-A have been shown to last from 3 to 6 months, after which muscle mass and force production return to normal (Ma, *et al*., 2004).

1.3.3 NMJ Aging Models

A loss of muscle mass and decrease in strength, termed "sarcopenia", are underlying factors in musculoskeletal impairment of aged populations (Goldspink, 2012). The age-associated decline in function subsequently leads to individuals being more susceptible to fatigue and injuries (Brooks & Faulkner, 2001). Both pre- and post-synaptic morphological changes are seen at the NMJ of aged tissue, indicating extensive remodelling during the aging process (Deschenes, 2011). These morphological changes are part of the pathophysiology of sarcopenia and result in NMJ dysfunction due to degradation of neural input to the muscle (Gonzalez-Freire, *et al.*, 2014).

Studying age-related NMJ changes has proved to be challenging due to the difficulty associated with directly studying the synapse in humans (Valdez, *et al*., 2010). As a result, clarity is still needed as to whether sarcopenia follows denervation or vice versa (Deschenes, *et al.*, 2010). A number of experimental techniques are utilised in an attempt to better understand the age-related effects, including electron microscopy, immunofluorescent staining, and electrophysiology (Banker, *et al.*, 1983) (Deschenes, *et al*., 2010). However, a recent review has concluded that novel structural, molecular and animal studies are still sorely needed (Gonzalez-Freire, *et al.*, 2014). Reviewing studies that used immunofluorescence and electrophysiology are in this case particularly relevant because these techniques are used in this thesis.

Various qualitative and quantitative IHC techniques were developed for assessing the mechanisms and extent of NMJ dysfunction in aged tissues (Deschenes, *et al*., 2013) (Plate, *et al.*, 2014) (Pannérec, et al., 2016). The Deschenes research group compared with young adult rats aged 8 months old (equivalent to a 23 year old human) to aged rats that were 24 months old (equivalent to a 71 year old human) (Deschenes, *et al*., 2013) (Turturro, *et al.*, 1999). 50 µm longitudinal sections were acquired from *soleus* and *extensor digitorum longus (EDL)* muscles of the hindlimb. Sections were stained with the neurofilament heavy polypeptide RT97 (pre-synaptic nerve terminals), α-Bungarotoxin (AChR) and anti-synaptophysin (ACh-filled pre-synaptic vesicles) (Anderton, *et al*., 1982). This allowed for the visualisation of both the pre- and post-synaptic components of the NMJ so that each could also be quantified.

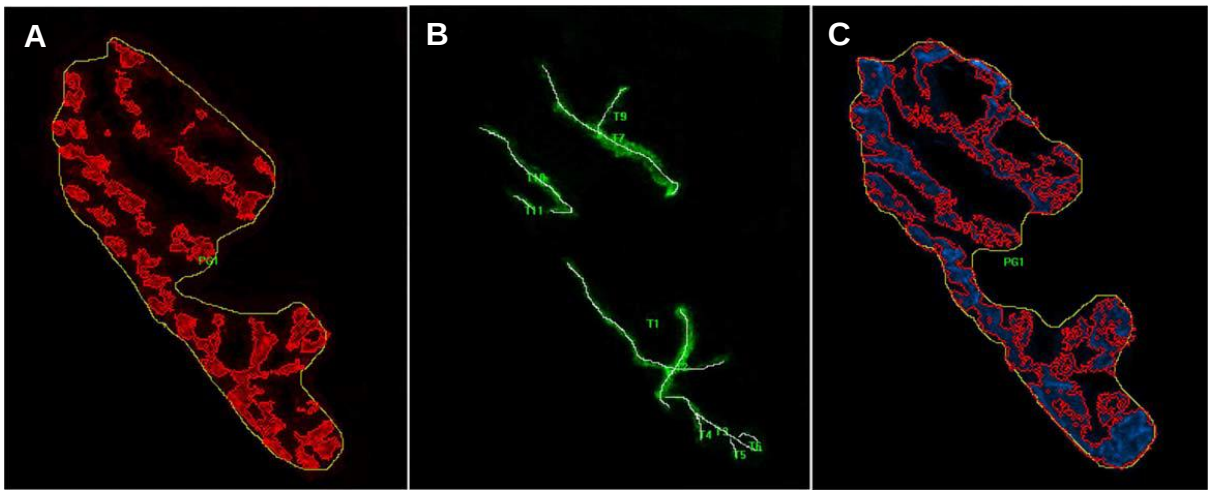

Figure 1.12 Representative image of quantitative measurement variables used on the NMJ at 1000X magnification. . A: Pre-synaptic vesicles containing ACh stained with anti-synaptophysin and outlined both manually and using software. B: Pre-synaptic nerve terminal branches stained with RT97 with tracings drawn to measure branch lengths. C: The post-synaptic AChR stained with α-Bungarotoxin and outlined both manually and using software to generate measurements. Image reproduced without permission (Deschenes, *et al*., 2013).

Pre-synaptic nerve branching and vesicles were assessed with a number of variables to produce quantitative data. Table 1.2 shows the different pre- and post-synaptic variables measured at the endplate (Deschenes, *et al*., 2013). Nerve branching was assessed by determining the number and lengths of nerve branches at the nerve terminal (see Table 1.2 and Figure 1.12 panel B). Branching complexity was then calculated by multiplying the number of branches at the nerve terminal by the total cumulative length of the branches, and then dividing by 100 (Tomas, *et al*., 1990).

Table 1.2 Pre- and post-synaptic measurement variables.

	Variables Measure
Nerve Branching	Number of branches at nerve terminal.
	Total cumulative length of branches at nerve terminal.
	Average length of each branch.
	Branching complexity.
Vesicle Staining	Total perimeter of the outline of the entire vesicular region at endplate.
	Total cumulative perimeter of the stained vesicular region at endplate.
	Total area of the outline of the entire vesicular region at endplate.
	Total area of the stained vesicular clusters at endplate.
	Dispersion of vesicles
AChR Staining	Total perimeter of the outline of the entire AChR region at endplate.
	Total cumulative perimeter of the stained AChR region at endplate.
	Total area of the outline of the entire AChR region at endplate.
	Total area of the stained AChR at endplate.
	Dispersion of AChR.

The pre-synaptic vesicle staining was assessed by measuring the total perimeter and area of the outline of the vesicular region, and the total perimeter and area of the stained vesicular clusters (see Table 1.2 and Figure 1.12 panel A). The dispersion of the vesicles was then calculated by dividing the area of the stained vesicular clusters with the total area of the outline of the vesicular region and multiplying by 100 (Deschenes, *et al*., 2013). Post-synaptic quantification of the AChR was similar to that of the vesicular staining (see Table 1.2 and Figure 1.12 panel C). The perimeter and area of the AChR outline, and the total AChR stained perimeter and area. Dispersion of the AChR was again calculated by dividing the stained area by the outlined area and multiplying by 100 (Deschenes, *et al*., 2013).

As previously mentioned, another fairly common quantitative method used in studies of sarcopenia is electromyography (EMG) measurements of specific muscles. Pannérec used both IHC morphology and EMG measurements to compare the muscle tissue of healthy adult and sarcopenic aging rats (8 to 10 months versus 22 to 24 months of age) (Pannérec, *et al*., 2016). The EMG protocol tested the function of the left *gastrocnemius* by measuring the compound muscle action potential (CMAP) (see Figure 1.13). This was achieved by inserting an electrode into the muscle and conducting a supra-maximal electrical stimulation via the sciatic nerve (Pannérec, *et al*., 2016).

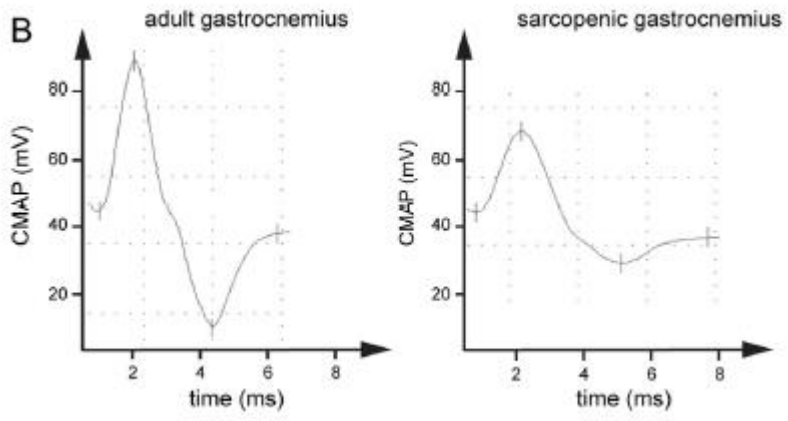

Figure 1.13 Electromyographic compound muscle action potential readings from the *gastrocnemius* muscle of adult and sarcopenic rats. Image reproduced without permission (Pannérec, *et al*., 2016).

1.3.4 Muscle Fibre Injuries

Incidents of muscle fibre injuries are surprisingly more common than one would expect. These injuries could include damage to the morphology of the myofibre, surrounding connective tissue or the synaptic components. There are a number of different ways that muscle fibre injuries can occur *in vivo*, including severe eccentric contractions, muscle contusions or restrictive compression injuries (Li & Thompson, 2011). Each of these can be simulated in experimental models.

1.3.4.1 Eccentric

An eccentric muscle contraction can be described as a lengthening contraction where the external load on the muscle is greater than the tension generated (Lindstedt, *et al*., 2001). Eccentric injuries could be mild such as that occurring with unaccustomed voluntary exercise (Lovering & Brooks, 2014), or severe. Severe NMJ injuries of eccentric origin are usually as a result of intense or exaggerated movements or in some cases even joint dislocations (Ozturk, 2015).

Between mild and severe models of eccentric-induced NMJ injury, a moderate injury can be induced by an externally supplied stimulation of maximal eccentric contractions (see Figure 1.14) (Lovering & Brooks, 2014).

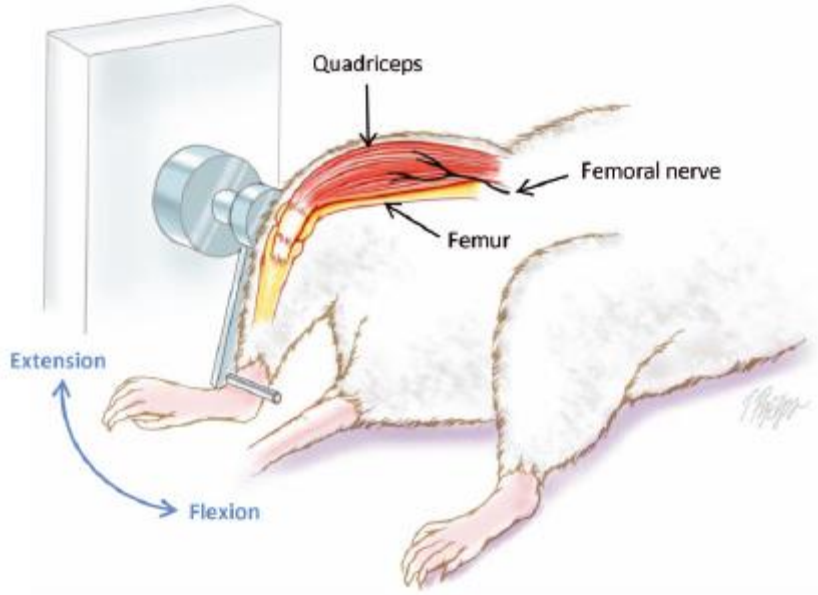

Figure 1.14 Apparatus setup for induction of an eccentric quadriceps muscle injury. Supramaximal exertion of the *quadriceps* muscle group can be achieved by inducing an isometric contraction against the motor-driven lever arm for 200 ms before the lever arm forces an eccentric lengthening of the quadriceps. Image reproduced without permission (Pratt, 2014).

Typically, such eccentric muscle injury is induced in the *quadriceps* muscle group in mice or rats using a motor-driven lever arm (Pratt, 2014) (Stone, *et al*., 2007). The ankle is secured under the lever arm, the knee aligned with a torque sensor and the femur stabilised (see Figure 1.14). Subcutaneous electrodes are used to stimulate the femoral nerve to produce extension of the knee and at the same time the motor-driven lever arm counteracts the extension motion by producing flexion of the knee. These opposing forces result first in an isometric contraction that typically lasts 200 ms before the lever arm overpowers the torque of the *quadriceps* to force knee flexion and subsequent eccentric contraction of the *quadriceps* (Pratt, 2014).

Even in rodent models, such forced eccentric contractions could be repeated up to 15 times through a 40° - 100° arc of motion (which is similar to human studies) with 1-minute intervals to induce an eccentric muscle injury (Paulsen, *et al.*, 2010).

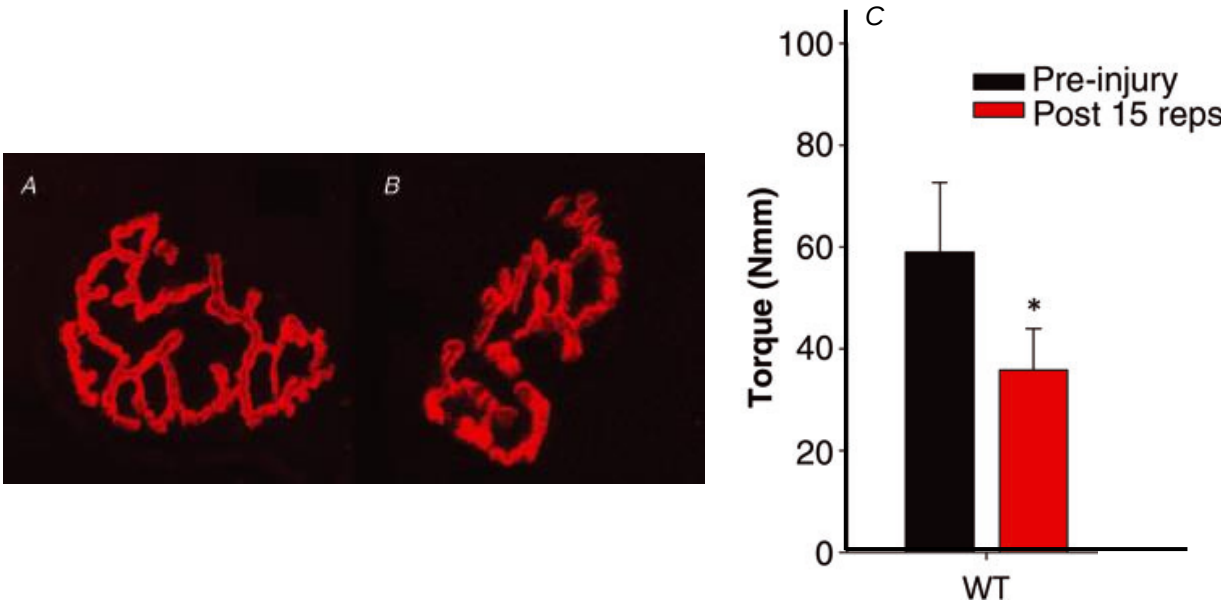

Figure 1.15 Morphological and functional changes in mouse *quadriceps* following eccentric muscle injury. A: Confocal microscope image of a section of *quadriceps* muscle before injury with the AChR stained with α-Bungarotoxin. B: Confocal microscope image of a section of *quadriceps* muscle after injury with the AChR stained with α-Bungarotoxin. C: Difference in maximal isometric torque produced by the quadriceps muscles pre- and post-injury. * indicates statistical significance of $P < 0.05$. Image reproduced without permission (Pratt, *et al*., 2013).

When this protocol was followed by Pratt *et al.*, a decrease in the functional capacity of the muscles followed the eccentric injury (see Figure 1.15 panel C) (Pratt, *et al.*, 2013). The repeated lengthening of the quadriceps resulted in greatly diminished maximal isometric torque production (39 ± 6%) 5 minutes post-injury. This is due to the focal mechanical damage to the sarcomeres of the myofibres (Macpherson, *et al*., 1996). However, in the study by Pratt *et al.*, the morphology of the NMJ and neuromuscular transmission which were assessed 24 hours after injury, were not significantly affected by the eccentric injury (see Figure 1.15 panels A and B) (Pratt, *et al*., 2013). It should be noted that this particular time point may not have covered all the post-injury consequences. Typically, the initial mechanical damage to the sarcomere initiates a cascade of secondary injury symptoms like inflammation, reactive oxygen species damage, sarcolemmal disruption and connective tissue damage (Evans & Cannon, 1991) (Morgan & Allen, 1999) (Rader, *et al*., 2006). These secondary events may be those that actually cause the NMJ injury, alongside the further degeneration of the muscle fibre segments that sustained the acute disruption damage (Lovering & Brooks, 2014).

1.3.4.2 Restrictive

Tourniquets are often used in instances of severe limb hemorrhaging to prevent a loss of blood (Inaba, *et al*., 2015). Unfortunately, the use of tourniquets has not been without setbacks, as a number of complications have been reported following tourniquet treatment and its subsequent release. The restriction by the tourniquet first causes a mechanical compression and ischemia, but with release ischemia-reperfusion has been shown to occur as unintentional repercussions with the use of tourniquets in emergencies (Kragh, *et al*., 2012) (Schoen, *et al.*, 2007).

Serious injuries to the nerve and skeletal muscle or both sides of the NMJ are frequently seen post-treatment (Doyle & Taillac, 2008). Both the functional and structural damage following tourniquet treatment results in extensive pathophysiology (Gillani, *et al*., 2012). To better understand this, animal models of tourniquet-induced injuries attempting to mimic those seen in humans have been utilised (Tu, *et al*., 2017).

It has been established that 3 hours of tourniquet application followed by 4 hours of tourniquet release on the hindlimb of a mouse was sufficient to cause necrosis and apoptosis in the *gastrocnemius* muscle of the affected limb (Tran, *et al*., 2011). Tu *et al*. recently showed that 3-hour tourniquet treatment followed by release resulted in both acute and long-term complications (Tu, *et al*., 2017).

Their experimental model used an orthodontic rubber band to restrict the hip joint of the left hindlimb of a mouse. The injury caused damage in the distal portion of the hindlimb, with the left *gastrocnemius* undergoing morphological changes to the NMJ. NMJ transmission was also impaired as a result of partial denervation immediately following the injury, and AChR degeneration during late-stage (after approximately 6 weeks) injury (Tu, *et al*., 2017).

1.3.4.3 Contusion

Muscle injuries are extremely common in athletes as well as the general population (whether sedentary or active) (Arrington & Miller, 1995). Contusion injuries have been reported as the second leading cause of sports-related injuries resulting in morbidity (Beiner & Jokl, 2001). The muscle crush injury used in animal models is an effective way to mimic a human muscle contusion injury. By utilising animal models, the *in vivo* recovery process of muscle contusion injuries can be investigated at many time points (Deane, *et al*., 2014). Muscle tissue repair, NMJ regeneration and functional nerve transmission need to be achieved for full recovery to take place (Beiner & Jokl, 2001).

A number of different contusion injury models have been described in the literature, with the method becoming far more common in recent years (see Table 1.3). Due to the non-invasive nature of the injury, it allows for the induced injury to remain relatively localised and not be disrupted by additional immune responses that may present in surgically induced injuries. The contusion injury also presents the perfect opportunity to specifically investigate the regeneration of the NMJ in conjunction with the nerve and muscle tissue (Hainline, 2014), since the eccentric contraction-induced injury is mainly focussed on sarcomere damage. Previous studies have reported that the intended injury has not, upon qualitative inspection, caused any bone damage or changes in the gait of the animal (Myburgh, *et al.*, 2012) (Tsai, 2018).

The muscle crush injury model that was implemented in this thesis to induce the muscle contusion injury also allows for an initiating point in the experiment that can be controlled, unlike injuries occurring during general life accidents/sports in humans (Tomazoni, *et al*., 2017). The contusion injury jig used was custom made by the Department of Mechanical Engineering of Stellenbosch University and has been previously used in protocols conducted by our research group (Myburgh, *et al.*, 2012). The height of the instrument was adjustable and allowed for the small weight to be dropped from a desired height (10 cm – 30 cm). The exact height to be used was determined so that it would create a moderately severe contusion injury.

Other similar apparatus and detailed use are presented in Table 1.3 below. From the starting point of the injury, the subsequent time course of events that occurs during the recovery process can be evaluated. Evaluation at multiple time points is important and also not always possible in humans since NMJ regeneration is highly complex involving many components – much like developmental synaptogenesis.

This highly complex and regulated process – much like developmental synaptogenesis – involves a number of components that carry out specific functions.

Table 1.3 Contusion Injury Protocols

Study	Animal	Limb	Injury Description
(Stratton, *et al*., 1984)	Male Holtzman Rats	Right upper hindlimb (*biceps femoris*)	Non-penetrating wound was induced on the right lateral thigh by an instrument developed at Brigham Young University. A 5.56 kg mass was dropped from a perpendicular height of 30.48 cm on to the *biceps femoris* to create a wound approximately 283.5 mm^2 in size.
(Wright-Carpenter, *et al*., 2004)	Female C57Bl/6 Mice	Lower hindlimb (*gastrocnemius*)	A mass-drop contusion injury was induced on the *gastrocnemius* muscle and resulted in a "high energy blunt trauma".
*(*Myburgh*, et al*., 2012)	Male Wistar Rats	Right lower hindlimb (*gastrocnemius*)	A drop-mass jig was used to produce a muscle contusion on the medial surface of the right *gastrocnemius*. A 200 g cylindrical mass was dropped from a perpendicular height of 50 cm.
(Deane, *et al*., 2014)	New Zealand White Rabbits	Left upper hindlimb (*vastus lateralis*)	A 201 g elongated oval-shaped mass was dropped on the left lateral thigh through a 1 m long tube. The drop was repeated seven times to induce a contusion injury on the left *vastus lateralis*.
(Liu, *et al*., 2018)	Male C57Bl/6 Mice	Lower hindlimb (*gastrocnemius*)	A tube with a diameter of 16 mm was set up with a 16.8 g stainless steel ball inside. The ball was dropped from a perpendicular height of 125 cm onto the belly of the *gastrocnemius* muscle.
(Song, *et al*., 2018)	Sprague-Dawley Rats	Right upper hindlimb (*biceps femoris*)	A metallic ball within an acrylic pipe was dropped onto the right upper hind limb to produce a muscle contusion.
(Tsai, 2018)	Male ICR Rats	Left lower hindlimb (*gastrocnemius*)	A mass-drop protocol entailing a 50 g mass dropped from a perpendicular height of 60 cm onto the left lower hindlimb. A contusion was induced on the medial surface of the *gastrocnemius.*

1.4 Aims and Hypotheses

The research in this thesis focussed specifically on the ultrastructure of the post-synaptic components of the NMJ in response to contusion injury. Qualitative assessment of the post-synaptic membrane was conducted in combination with quantitative structural and functional examinations to best establish the time course of regeneration for different elements.

This study aimed to:

- Qualitatively assess the cellular morphology and post-synaptic structure of the NMJ in healthy skeletal muscle tissue.
- Qualitatively assess the cellular morphology and post-synaptic structure of the NMJ following injury and over the course of its regeneration.
- Quantitatively determine the extent of post-synaptic AChR-associated protein dispersion in response to injury.
- Quantitatively determine the co-localisation and co-occurrence of the AChR with its associated accessory proteins.
- Establish a timeline of muscle function recovery in response to injury.

This thesis presents the following hypotheses:

- AChR and rapsyn will sustain less dispersion from their normal position than MuSK, LRP4 and Dok7 in response to a muscle crush injury, because of their tighter co-localisation in healthy muscle.
    - Due to rapsyn's unique role in structural stabilisation of the AChR and its position as an intracellular cytoskeletal-associated protein, one would expect less severe dispersion in response to injury.
    - The tethering function of rapsyn may be responsible for maintaining confined signal expression of the AChR and rapsyn itself.
- Nonetheless, normal AChR structure and distribution is restored only in conjunction with the return of accessory protein co-localisation.
- A return of muscle function follows the structural regeneration of the synapse.

"When you want to know how things really work, study them when they're coming apart." – (Gibson, 2010).

CHAPTER 2: METHODS

2.1 Study Design

2.1.1 Animals

Male BALB/C mice were bred at the Stellenbosch University Medicine and Health Sciences Faculty small laboratory animal breeding facility. Animals were transported to and housed in the small animal facility at Stellenbosch University Department of Physiological Sciences once weaned. Animals were divided and housed 3 to 5 animals per cage for the duration of the study. The room was temperature controlled at between 21° and 24° C, with ventilation changes at 10 changes every hour under a 12:12 hour light:dark cycle. Animals had access to water and rodent chow *ad libitum* and cages were cleaned at least once a week. Monitoring of animals was carried out daily on the Animal Monitoring Sheet and animals were handled regularly to familiarise them with the handler (T. Faulmann).

All animals were required to reach maturity (>10 weeks; mean mass 27.42 g) prior to being subjected to any experimental protocols. All experimental protocols were approved by the Animal Ethics Committee of Sub-Committee B of Stellenbosch University (Protocol #: 0915) and undertaken with the animal under general anaesthesia.

2.1.2 Experimental Groups

Animals were randomly divided into the following experimental groups:

1. Control Group (D0) – Animals not subjected to any injury. N = 10.
2. 3 Day Post-Injury Group (D3) – N = 8.
3. 7 Day Post-Injury Group (D7) – N = 8.
4. 14 Day Post-Injury Group (D14) – N = 8.

For the control group, a baseline muscle function force test was carried out immediately prior to euthanasia. Animals from the injury groups had a closed muscle crush injury induced to the right *gastrocnemius*. For the injury groups, a baseline muscle function force test was carried out immediately prior to injury and the longitudinal post-injury test was carried out just prior to euthanasia at the respective time points of the groups. Euthanasia was achieved via exsanguination, with blood draws taken by means of cardiac puncture. The injured right *gastrocnemius* and contralateral control left *gastrocnemius* muscle were then excised and cryopreserved.

2.2 Experimental Protocol

2.2.1 Force Testing

2.2.1.1 Experimental Setup

The *in-vivo* muscle function force testing experimental setup consisted of the Whole Animal System (Aurora Scientific Instruments, 1300A, Aurora, Canada) with mouse specific hardware attachments. The animal platform included a mounted knee clamp and footplate, and needle stimulation electrodes. Readings were collected, and data analysed with the Data Acquisition and Analysis System software (Aurora Scientific Instruments, 605A, Canada).

Figure 2.1 Mouse secured under anaesthesia via nosecone. Shaved lower limb exposed for experimental procedure.

2.2.1.2 Anaesthesia

Animals were individually anaesthetised in a sealed Perspex container with a precision isofluorane vaporiser (Ohmeda Isotech 4, Ohmed, Nevada USA). 3% Isofluorane (Isofor, Piramal Health Care, Mumbai India) in 100% oxygen was administered for induction. Once the animal was fully unconscious, it was removed from the chamber and placed on the animal platform, with 2% isofluorane delivered via a nosecone for maintenance (see Figure 2.1). Sufficient depth of anaesthesia was assessed by testing the pedal reflex (pinch between the toes).

2.2.1.3 Force Testing Protocol

A heating lamp was used to regulate the body temperature of the anaesthetised animal for the duration of the procedure. Animals were placed in supine position and the right lower hind limb shaved with a disposal razor (see Figure 2.1). The right foot was then fastened in place on the footplate with masking tape and the knee secured with the knee clamp. The two needle stimulation electrodes were placed subcutaneously along the lateral and medial surfaces of the *gastrocnemius* muscle belly, until the neck region of the fibula (see Figure 2.2). This allowed for stimulation of the superficial fibular nerve due to its superficial position over the lateral *gastrocnemius* head.

The sequence protocol was loaded on the Dynamic Muscle Control (DMC) programme to obtain readings for a force-frequency relationship. The force produced at different frequencies was measure in grams of weight and later converted to millinewtons (1 g = 9.8 mN) (Head & Arber, 2013). A total of 8 stimulations were carried out at 15; 30; 45; 60; 75; 90; 105 and 120 Hz, with an interval of 45 s (Distefano, *et al.*, 2013) (Pasteuning-Vuhman, *et al.*, 2017). The maximum force values for each frequency were recorded and divided by the body mass of the animal. This calculated value was plotted against its respective frequency to establish a sigmoidal curve (Head & Arber, 2013).

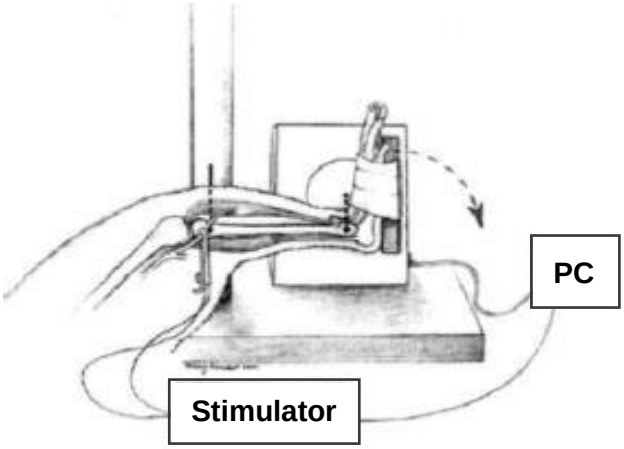

Figure 2.2 Force Testing Protocol Setup. Mouse secured at the knee clamp and footplate on animal platform, with electrodes inserted. The sequence protocol loaded onto the PC was executed via the stimulator**.** Image modified and reproduced without permission from (Lovering, 2013)**.**

2.2.2 Muscle Injury

2.2.2.1 Apparatus

A muscle crush injury was induced using a custom apparatus designed by the Central Engineering Services, Stellenbosch University specifically for the Muscle Research Group, Department of Physiological Sciences. The apparatus comprised of a square metal base (approximately 20 cm X 20 cm) with 5 mm cylindrical platform in the centre of the base. A plastic tube with holes drilled at regular intervals along its length was positioned perpendicularly above the platform to direct the passage of the small cylindrical weight.

The weight (mass = 35 g; diameter = 4.5 mm) was attached to a string that exited the top of the tube and acted as a pulley to move the mass to any chosen height. A height of 11 cm was used for the duration of the experiment and a steel peg was inserted at this height to hold the weight in place. Removal of the peg resulted in the weight being dropped directly onto the platform. This enabled the impact of the dropped weight to occur on the desired area of muscle. Using a specific height for the entirety of the experiment also ensured that the velocity of the weight as it impacted the muscle was standardised across repeated attempts.

2.2.2.2 Procedure

Animals were placed under anaesthesia as previously described in section 2.2.1.2 and right lower hind limb shaved with a disposal razor (see Figure 2.1). The injury was carried out immediately after baseline force testing was conducted while the animals were still anaesthetised via the nosecone. Animals were placed in the supine position on the base of the apparatus with the right lower hind limb placed on the platform. The ankle and knee were secured on either end of the platform using one's fingers, with the knee joint held at a 90° angle to reduce tension in the calf. The medial surface of the *gastrocnemius* was adequately exposed for impact without any injury occurring to the tibia/fibula bone. Once the leg was sufficiently secured, the peg was removed, causing the weight to be dropped on the exposed *gastrocnemius* belly. The impact of the muscle crush injury induced a contusion of the soft tissue. The animal was removed from the nosecone post-injury and placed in a new cage to recover. Animals were monitored until consciousness was regained and a normal walking gait established before being placed back into their original cages.

2.3 Euthanasia and Sample Collection

2.3.1 Exsanguination

All animals were sacrificed by means of exsanguination, with blood draws carried out via cardiac puncture while anaesthetised. All surgical equipment was sterilised and an appropriate number of 2 mL syringes and labelled 4 mL EDTA coated blood collection tubes (BD Vacutainer K2 EDTA, Fisher Scientific, Waltham USA) set aside. Animals were individually weighed, and body mass recorded before being placed under anaesthesia as previously described in section 2.2.1.2. They were then moved to the sterilised work space and placed in the supine position, with anaesthesia administered via nosecone and pedal reflex tested.

Using forceps and a pair of scissors, an incision was made along the midline of the animal from the abdominal region to the pectoral region. The ribcage was then bisected by cutting through the sternum to expose the thoracic cavity. Special care was taken to avoid penetrating any internal organs. The aorta was severed and blood drawn up from the thoracic cavity with a syringe. Blood was quickly transferred to the appropriately labelled EDTA tubes. Blood was gently mixed with the anticoagulant by inverting the tubes and kept at room temperature before being processed.

Blood samples were centrifuged (see section 2.4.1) within approximately 30 minutes (after muscle excision). Euthanasia was confirmed by a visible lack of heartbeat and pedal reflex, and the animal was then removed from the nosecone.

2.3.2 Muscle Excision

Prior to muscle excision, 4 cork squares (approximately 10 mm X 10 mm) were cut and labelled appropriately for each animal, and isopentane (Merck, 109-66-0, Darmstadt, Germany) was cooled in liquid nitrogen. Animals were placed in prone position and using a scalpel an incision was made around the base of the right hind limb at the ankle joint. Fine tipped forceps were used to remove the skin and connective tissue, leaving the skeletal muscle of the entire hind limb exposed.

One arm of the forceps was inserted between the Achilles' tendon and the tibia at the base of the hind limb. It was slid towards the knee joint to separate the superficial posterior compartment muscles from the rest of the lower leg. The superficial posterior compartment muscles were severed using a pair of surgical scissors at the Achilles' tendon and just inferior to the knee joint to ensure the site of injury was intact.

The *soleus* and *plantaris* muscles on the deep surface of the muscle complex were removed along with any connective tissue and remaining fascia to leave behind only the bilateral *gastrocnemius* heads. The *gastrocnemius* heads were split, with one mounted cross-sectionally and the other longitudinally on the cork (see Figure 2.3) with the optimum cutting temperature (OCT) media (Tissue Tek, Leica, 03706329, Nussloch, Germany).

Samples were frozen in the liquid nitrogen cooled isopentane for approximately 60 seconds before being placed in a tank of liquid nitrogen for safe transportation. This exact procedure was repeated on the uninjured left hind limb, to serve as a contralateral control. Samples were stored in a -80° C freezer until required.

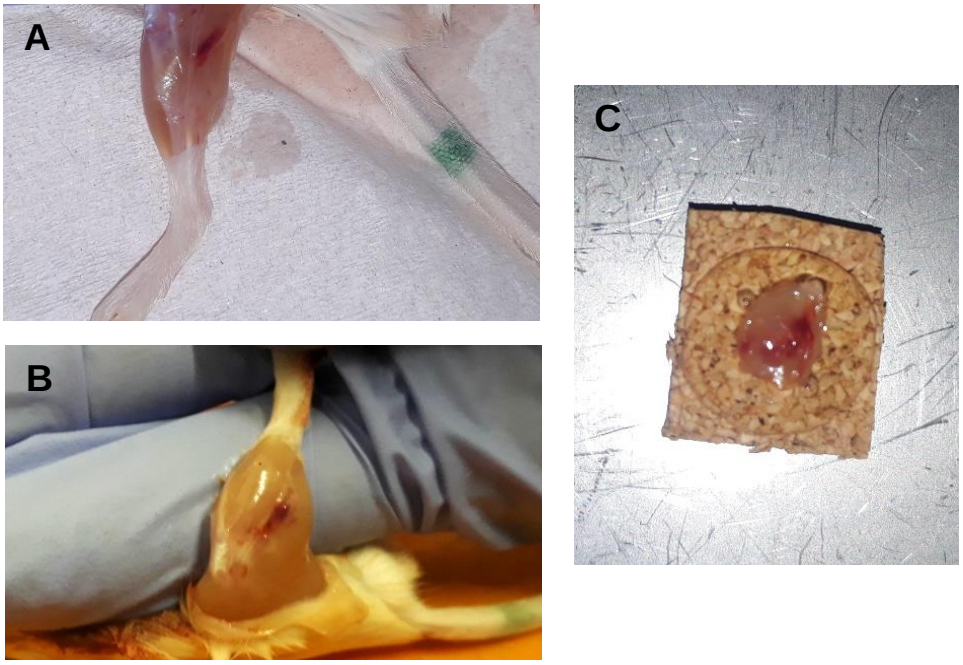

Figure 2.3 Injured mouse *gastrocnemius* during muscle excision and mounting. A: The medial *gastrocnemius* head (impacted side) of an injured limb at 7 days post-injury. Visible hematoma is present in the muscle belly. B: The lateral *gastrocnemius* head of an injured limb at 3 days post-injury. Visible hematoma with a diffuse border is present in the muscle belly. C: *Gastrocnemius* of injured limb at 3 days post-injury mounted on cork in longitudinal orientation.

2.4 Sample Analyses

The following analytical procedures were used on the collected samples:

1. ELISA performed on blood plasma
2. Histological assessment of longitudinal and cross muscle sections
3. Immunohistochemical analysis of longitudinal and cross muscle sections

2.4.1 Blood Plasma Isolation

Blood samples collected in EDTA tubes were centrifuged for 15 min at 2000 rpm at 4° C (Merck, Germany). Supernatant was carefully pipetted to a labelled 1.5 mL capped plastic tube (Eppendorf, Sigma St. Louis USA) and stored in a -80° C freezer until required.

2.4.2 Cryo-sectioning

Muscle samples were removed from the freezer and placed in the cryostat (Leica CM1860 UV Cryostat, Nussloch, Germany) with the temperature set to -25° C. Samples were left for an hour to adjust to the temperature before sectioning was carried out. Once equilibrated to the change in temperature, each sample was mounted. The cork square base of each frozen sample was fixed to the specimen disk with OCT media (Leica, 03706329, Nussloch, Germany). The mounted sample was then secured to the microtome and a cryostat blade fastened in the special blade holder.

Both cross-sectionally and longitudinally mounted samples were sectioned at a thickness of 20 µm and pressed to a poly-L-lysine (P4707, Sigma Aldrich, St. Louis USA) coated microscope slide. Approximately 4 sections were placed on slides intended for immunohistochemistry and 6 sections were placed on slides on intended for histology. Slides were placed in a sealed container and stored at -20° C until staining was carried out. Leftover tissue was carefully pried off of the specimen disk, relabelled and returned to storage in a -80° C freezer.

2.4.3 Histology

Both longitudinal and cross sections of each muscle sample were stained with haematoxylin and eosin (H&E) and visualised on a light microscope. Areas of induced injury were identified, and the severity of muscle fibre damage was observed by assessing the extent of oedema, immune cell infiltration, and the destruction of tissues.

2.4.3.1 Haematoxylin and Eosin Staining

An automated stainer (Leica ST4020 Small Linear Stainer) was used to carry out the Meyer's Haematoxylin (Sigma Aldrich, SLBK4907V, St. Gallen, Switzerland) and Eosin Y (Leica, 390512, Peterborough, England) staining protocol (see Addendum A). Slides with cryo-sections were allowed to defrost at room temperature (RT) for at least 30 minutes to prevent sections washing off.

Slides were placed in the slide holders and the customised protocol settings were uploaded to the automated system. The standard protocol that was used required slides to remain in each reagent for 2 minutes before being transferred to the next. The order of reagents was as follows, distilled water (RT), Mayer's Haematoxylin, warm tap water, Scott's Tap Water, 95% alcohol, Eosin Y, 95% alcohol, 100% alcohol and a final change of 100% alcohol (see Addendum A). Once the protocol was completed, slides were removed from the holders and excess fluid wiped off with a paper towel. Slides were left to dry completely before being mounted with DPX Mountant (NICE Chemicals, 2217, Kerala, India) and a 50mm x 24 mm coverslip (CS24X50-2, Livingstone Industrial, Sydney Australia).

2.4.3.2 Imaging

The bright field view of a fluorescent microscope (Nikon ECLIPSE E400, New York, USA) was used to visualise stained sections. Images were attained using the 4X, 10X and 20X objectives and captured by a microscope camera controller (Nikon DS-U3) with imaging software (NIS-Elements version 4.0). Morphological characteristics were identified by assessing the muscle section as a whole, along with a more detailed approach to regions of interest.

2.4.4 Immunohistochemistry

2.4.4.1 Reagents

The following markers were used in various combinations:

1. α-Bungarotoxin (α-Btx) – post-synaptic nicotinic AChRs
2. anti-MuSK – MuSK, a transmembrane synapse-regulating protein associated with the NMJ
3. anti-rapsyn – rapsyn, a sub-sarcolemmal structural protein that stabilises the AChR
4. anti-Dok7 – Dok7, a sub-sarcolemmal adaptor protein responsible for activating MuSK and facilitating its downstream signalling.
5. anti-LRP4 – LRP4, a transmembrane co-receptor that enables MuSK activation
6. Hoechst – DNA of interphase nuclei (myonuclei, satellite cell, blood cells etc.)

All dilutions were made up in 1% bovine serum albumin (BSA).

Table 2.1 Antibodies used to identify AChR (α-Btx), MuSK, rapsyn, Dok7, LRP4 and myonuclei (Hoechst).

Antibodies	Cat no.	Supplier	Host Species	Dilution	Fluorescent Dye
α-Btx AlexaFluor® 488 Conjugate	B13422	Invitrogen, Life Technologies, Molecular Probes	*Bungarus multicinctus*	1:500	AlexaFluor® 488
anti-MuSK	ABS549	EMD Milipore	Rabbit Polyclonal	1:200	AlexaFluor® 594
anti-rapsyn	ab11423	AbCam	Mouse Monoclonal	1:150	AlexaFluor® 555
anti-Dok7	NBP2-02073	Novus Bio	Mouse Monoclonal	1:150	AlexaFluor® 555
anti-LRP4	ab122923	AbCam	Goat Polyclonal	1:200	AlexaFluor® 555
Hoechst	14533	Sigma-Aldrich, Schnelldorf, Germany		1:1000	Blue fluorescent dye

2.4.4.2 Procedure

For detailed protocol for IHC staining listed see Addendum B.

Slides with cryosections were removed from the freezer and allowed to defrost at RT for at least 30 minutes to prevent sections from washing off. Once defrosted, slides were dried and a PAP liquid-repellent slide marker pen (Dako, S2002, Glostrup, Denmark) was used to draw a hydrophobic circle around each section. If sections were longitudinal, the tissue was fixed with 1% PFA (Sigma Aldrich, SZBD3180V, Steinheim, Germany) for 8 minutes. Cross-sections were exempt from the fixation step.

Longitudinal sections were drained and together with cross-sections were permeabilised with 0.1% Triton X solution (BDH, 1014224, Poole, England) for 15 minutes. The Triton X solution was drained off and slides were allowed to dry completely before being washed with PBS. Sections were incubated with blocking serum made up of 5% donkey serum (AbCam, ab7475, Cambridge, USA) and 0.1% Triton X in 1% BSA (Roche, 70331927, Mannheim, Germany), for 60 min at RT to reduce non-specific binding. Following the incubation period, the blocking serum was drained, and washing steps repeated. A primary antibody of choice was added to the slides for incubation overnight at -4° C in a humidifying black box. The following day, primary antibody solution was drained, and wash steps repeated.

Table 2.2 Secondary antibodies used with primary antibodies.

Antibodies	Cat no.	Supplier	Host Species	Dilution
AlexaFluor® 594	ab150076	AbCam	Donkey Polyclonal to Rabbit IgG	1:200
AlexaFluor® 555	ab150130	AbCam	Donkey Polyclonal to Goat IgG	1:200
AlexaFluor® 555	ab150106	AbCam	Donkey Polyclonal to Mouse IgG	1:150

From here on out, staining was carried out in the dark, due to light-sensitive secondary antibodies being used. A constant humidified environment was also maintained to prevent slides from drying out. Appropriate secondary antibodies were added, and slides were allowed to incubate at RT. After 4 hours of incubation, wash steps were repeated before the addition of α-Btx to sections. Slides incubated for 60 minutes at RT and wash steps were repeated. Hoechst 33342 nuclear stain was added to sections and incubated for 10 minutes, followed by wash steps. Slides were left to dry completely and then mounted with fluorescent mounting media (Dako, S3023, Carpentaria, USA) and coverslip.

2.4.4.3 Imaging

Slides were imaged on a confocal microscope (LSM 780 with Elyra S.1 Superresolution platform, Carl Zeiss, Oberkochen Germany) with Zen 2011 imaging software (Carl Zeiss, Oberkochen Germany). Custom wavelength ranges were set for each fluorophore channel and settings were saved to ensure settings were duplicated across all images acquired. Ranges were set as follows:

- 405 nm Laser for Hoechst: 410-480 nm
- 488 nm Laser for AlexaFluor 488: 500-550 nm
- 561 nm Laser for AlexaFluor 555: 560-625 nm
- 561 nm Laser for AlexaFluor 594: 595-650 nm

Fluorescent images were observed with a “Plan-Apochromat” 20x/0.8 M27 LD objective to locate AChRs, and then Z stack images were captured with a “Plan-Nuofluar” 40x/0.6 Corr M27 objective. Z stack images were obtained with uniform settings across all images and within each channel (see Table 2.3) (Ammar, *et al*., 2013) (Amenta, et al., 2012). Only AChRs orientated *en face* were captured and analysed to avoid misrepresentation of data (Pratt, *et al.*, 2015). Maximum intensity projection images were constructed from the Z stacks captured for further analysis.

Table 2.3 Confocal microscope channel settings for Z stacks acquired.

Channel	Pinhole	Laser Intensity	Gain	Digital Offset	Digital Gain
Hoechst	1 AU	6%	600	-2	1.0
AlexaFluor® 488	1 AU	7%	720	-2	1.5
AlexaFluor® 555	1 AU	7%	700	-2	1.5
AlexaFluor® 594	1 AU	6.5%	650	-2	1.5

2.4.4.4 Image analysis

ImageJ version 1.51 (NIH, Bethesda USA) was used to carry out several quantitative analyses on the confocal images captured. The same algorithm and processes were applied to all images to ensure that staining signal quantification remained as accurate and objective as possible (Mori, *et al.*, 2017).

For each image, the channels were split, background subtracted and noise de-speckled (Pratt, et al., 2015) (White, 2011). Images then had a colour threshold applied and a binary image was generated for various measurements (Gomez, *et al.*, 2016) (Amenta, *et al.*, 2012) (Pratt, *et al*., 2015).

The following quantification variables were measured (Barik, *et al.*, 2014) (Noller, *et al.*, 2016)(Otsuka, *et al.*, 2015):

- Total Outlined Area (TOA)
- Total Stained Area (TSA)
- Staining Intensity (SI)
- Density (SI/TSA)
- Co-localisation
    - Pearson's Correlation Coefficient (P)
    - Mander's Overlap Coefficients (MOC1 & MOC2)

Within each of the 4 groups (D0; D3; D7 and D14), 4 synaptic proteins (rapsyn, MuSK, LRP4 and Dok7) were individually analysed in conjunction with the AChRs. For each synaptic protein sub-group data were accumulated from 10 endplates. Group D0 consisted of 10 endplates across 10 mice (i.e. 1 represented from each mouse). Groups D3, D7, and D14 consisted of 10 endplates across 8 mice for each group, with a minimum of 1 endplate represented from each mouse. The following 3 objective criteria were used for each endplate selected:

- AChR in *en face* view
- AChR not near injury-induced debris
- Minimal background signal from synaptic protein channel

This objective selection process eliminated a large number of endplates that were imaged but could not fulfil all 3 criteria. No more than 2 endplates from each mouse were eligible for analysis. Addendum C shows visual differences between endplates that met the criteria versus those that did not.

For each protein of interest the stained image was analysed for quantifiable data as follows:
The ImageJ Polygon Selection tool was used to manually draw along the outline of each endplate to create a region of interest (ROI). The ROI was then analysed using the ImageJ Analyse function and Measure tool to generate the TOA. Thereafter, the area of an endplate stained positively was first selected using an automated ImageJ Threshold selection tool (staining intensity threshold set once and applied for each subsequent endplate). Then the Measure tool was used again to acquire the TSA of each endplate. From the TSA, the mean fluorescent intensity (SI) was determined, and used to calculate the staining density (SI/TSA). Measurements for each ROI included intensity statistics (mean, min and max) and area parameters (area and perimeter) (Ferreira & Rasband, 2012).

Pearson's correlation co-efficient (PCC) and the Mander's overlap co-efficient (MOC) are two commonly used methods of quantifying co-localisation of fluorophores (Adler & Parmryd, 2010). The ImageJ "Coloc 2" function was used and generated a full report detailing the respective MOC1, MOC2 and P values for each AChR and synaptic protein image pair (Ferreira & Rasband, 2012).

The PCC is calculated taking into consideration the spatial relationship between intensities of the fluorophores from the two channels (typically red and green) and the difference from the mean intensity of each to describe the signal correlation between the two channels (P). It is not calculated similarly to the well-known statistical p-value.

The formula used to determine the PCC is as follows (Manders, *et al.*, 1992):

$$P = \frac{\sum_i (R_i - \bar{R}) \times (G_i - \bar{G})}{\sqrt{\sum_i (R_i - \bar{R})^2 \times \sum_i (G_i - \bar{G})^2}}$$

$\bar{R}$ and $\bar{G}$ refer to the mean intensities of red and green channels, while R_i and G_i refer to the specific intensity value of the red and green channels for a given pixel (i). The P value falls between -1 and 1, where 0 indicates that the positive pixels of the two channels of interest do not correlate i.e. are randomly distributed. P = 1 when the two channels are perfectly and linearly related in space and intensity, while P = -1 indicates a perfect, but inverse relationship i.e. not randomly distributed, but with no overlap (Dunn, *et al.*, 2011).

The MOC describes the fraction of signal of a given channel that is located where there is positive signal of another channel and can be described as co-occurrence of pixels. For example, MOC1 is the fraction of the area of AChR signal (denoted as *G*) that overlaps with rapsyn positive signal (denoted as *R*) and MOC2 is the fraction of the area of rapsyn signal that overlaps with AChR positive signal. The MOC equations are as follows (Manders, *et al.*, 1993):

$$MOC1 = \frac{\sum_i G_{i,colocal}}{\sum_i G_i} \text{ where } G_{i,colocal} = G_i \; if \; R_i > 0 \; and \; G_{i,colocal} = 0 \; if \; R_i = 0$$

$$MOC2 = \frac{\sum_i R_{i,colocal}}{\sum_i R_i} \text{ where } R_{i,colocal} = R_i \; if \; G_i > 0 \; and \; R_{1,colocal} = 0 \; if \; G_i = 0$$

Example	P Value	MOC1	MOC2
	0	0	0
	0.23	0.30	0.30
	1.00	1.00	1.00

Figure 2.4 Correlation coefficients calculated for selected examples. Modified and reproduced without permission from (Hartmann, *et al.*, 2012)**.**

Unlike the PCC, the MOC operates independently of signal intensity proportionality and only measures co-occurrence. However, the Costes' threshold method was used as an additional tool provided by the "Coloc 2" function to take signal intensity into consideration when calculating the MOC. This unique method was developed to determine a threshold value for background signal. Only pixels that fall above the respective threshold for each channel are considered when calculating the MOC values. The Costes' method allowed for more robust and reproducible calculations of an accurate MOC than what were available before (Dunn, *et al.*, 2011).

2.4.5 ELISA Analysis

An Enzyme-linked Immunosorbent Assay kit for MuSK (SEE270Mu 96, Cloud Clone, Katy USA) was used to determine the presence of the protein in blood plasma samples. The wells of the ELISA microplate kit were pre-coated with a biotin-conjugated anti-MuSK antibody. Detailed protocol for ELISA kit and sample preparation listed in Appendix D.

All kit components and samples to be tested were brought to room temperature before being prepared as indicated in the instruction manual. Standard curve dilutions were tested in triplicates (N = 3) of each concentration at 10ng/mL, 5ng/mL, 2.5ng/mL, 1.25ng/mL, 0.625ng/mL, 0.312ng/mL, 0.156ng/mL and a blank well (see Figure 2.5).

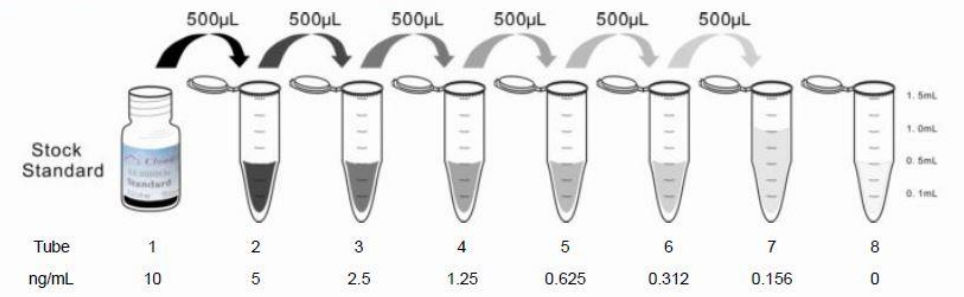

Figure 2.5 Double dilution series prepared from stock standard. Standard curve dilutions prepared from stock standard solution (concentration 10ng/mL) according to manufacturer's instructions (Cloud-Clone, 2013).

Samples were used undiluted due to low presence of MuSK expected in plasma (N = 10 for D0, and N = 18 for D3, D7 and D14). 100 µL of either standard or sample was added to each well and incubated with the lid sealed for 1 hour at 37° C. The standard/sample was then aspirated and 100 µL of Detection Reagent A was added to each well and incubated with the lid on for 1 hour at 37° C. Remnants were again aspirated following incubation and washed 3 times with Wash Solution.

100 µL of Detection Reagent B was added to the plate and incubated with the lid on for 30 minutes at 37° C. Remaining liquid was aspirated and washed 5 times with Wash Solution. 90 µL of Substrate Solution was added to the plate and incubated with the lid on for 10 - 20 minutes at 37° C. Finally, 50 µL of Stop Solution was added to each well and read with a microplate reader (EZ Read 400, Biochrom, Cambridge, United Kingdom) at 450 nm immediately (Cloud-Clone, 2013) (Ma, *et al.*, 2017).

The average zero standard optical density (blank) was subtracted from mean of each standard and sample. A standard curve was generated from the mean Optical Density (OD) for each standard with the sigmoidal best fit function on GraphPad Prism 4 (GraphPad Software, La Jolla, CA). The means ± SD of MuSK plasma concentration for the sample groups were then interpolated from the curve.

2.5 Statistics

GraphPad Prism 4 (GraphPad Software, La Jolla, CA) was used for statistical analyses of the body mass, force testing and ELISA data. Body mass of the animals, area under the curve (AUC) of force-frequency and ELISA data were analysed by means of a one-way analysis of variance (ANOVA) test with Tukey's multiple comparisons post hoc test. The force-frequency curves were compared using a two-way ANOVA and Bonferroni multiple comparison post hoc test. $P \leq 0.05$ was considered significant and values were expressed as means ± standard deviation (SD) unless otherwise stated. Statistica (TIBCO Statistica 13.4.0, Palo Alto, CA) was used for the statistical analyses of the IHC quantitative data. The Staining Density, TSA and TOA underwent a fixed effect and LSD test, and data are presented with error bars indicating 95% confidence intervals and $P \leq 0.01$ was considered significant.

CHAPTER 3: RESULTS

3.1 Body Mass of Animals

For each group, animals were weighed at baseline immediately prior to administration of injury and again at their designated time point, on the day of sacrifice. On both occasions, body mass was measured before force testing was carried out. The mean body mass of all mice prior to injury was 27.42 g, while at the time of sacrifice the mean body mass of all mice was 27.18 g (see Addendum E Table E.1). There was no significant difference found over time comparing pre- and post-injury groups, or between the different groups sacrificed at different time points (see Figure 3.1 below).

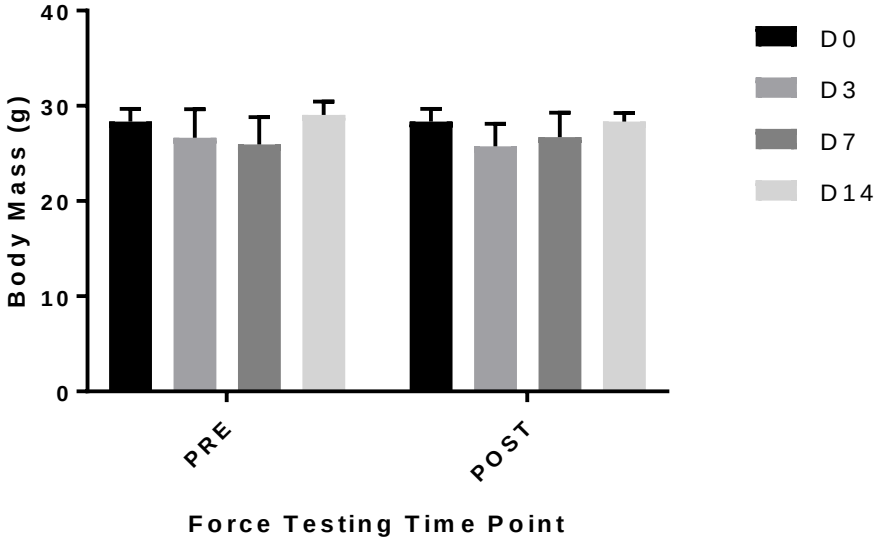

Figure 3.1 Mouse body mass measured pre-injury and on day of sacrifice between 3 and 14 days post-injury. Data are presented as means (N = 10 for D0, and N = 8 for D3; D7 and D14), with ± SD. One-way ANOVA revealed no significant differences.

3.2 Effect of Crush Injury on Muscle Morphology

Cryo-preserved control samples, as well as samples from the non-injured contralateral limb of an injured animal, were used to establish the morphology of normal, healthy skeletal muscle tissue. Samples from the injured limbs were then compared to the non-injured samples, and the extent of damage was assessed qualitatively. All samples were stained with Meyer's hematoxylin and Eosin Y to assess healthy *gastrocnemius* fibres. Hematoxylin stained the basophilic structures in the tissue, namely cell nuclei, and they appeared blue-purple. Eosin stained eosinophilic matter that appeared pink-red and included the cytoplasm, intra- and extra-cellular proteins, and epithelial cells (M.A & s, 2011).

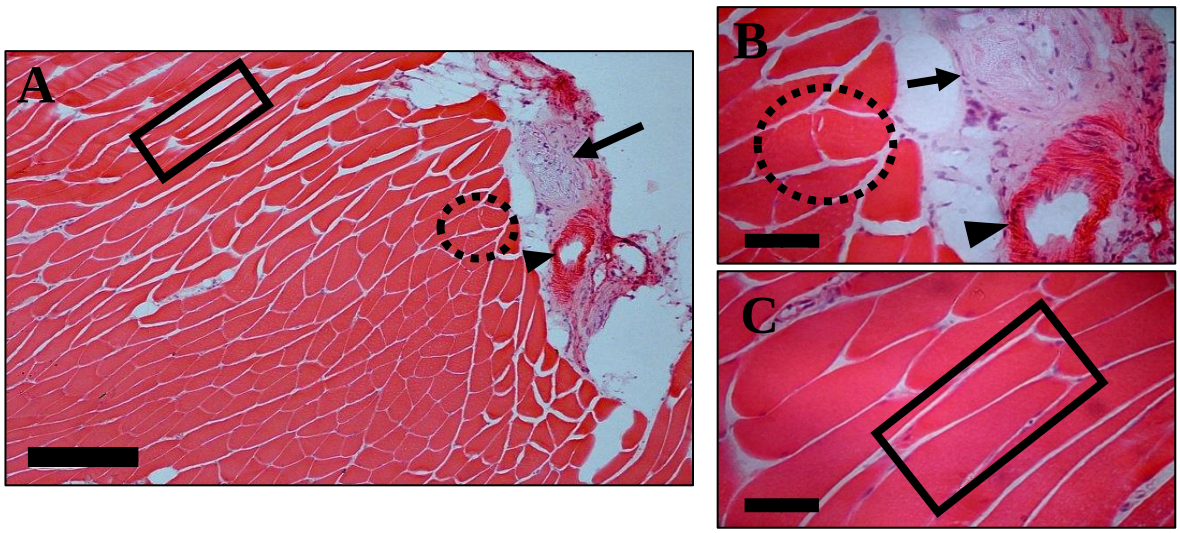

Figure 3.2.1 H&E stained longitudinal sections of uninjured, healthy *gastrocnemius* skeletal muscle with uninterrupted fibres in uniform pattern. A: 10X magnification of control muscle section; scale bar = 200 µm. Rectangle indicates areas of intact longitudinal fibres. Circle indicates region with fibres in transverse orientation. A blood vessel and tendon are located on the distal portion of the muscle. The arrow identifies attachment of the tendon at its insertion point and a solid arrowhead indicates the blood vessel. B and C: 40X magnifications of regions of interest in Panel A; scale bars = 20 µm.

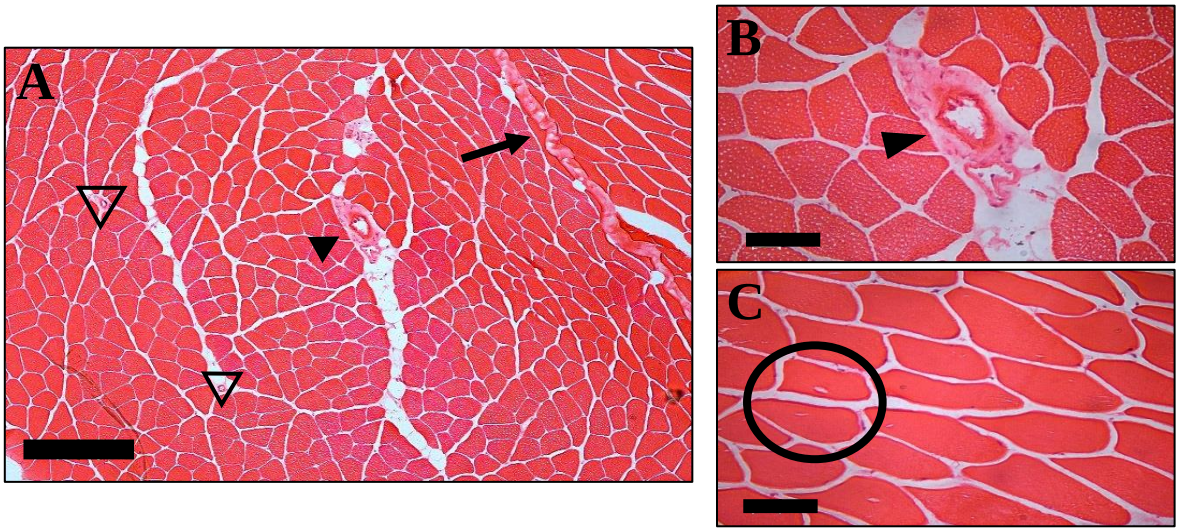

Figure 3.2.2 H&E stained cross-sections of uninjured, healthy *gastrocnemius* skeletal muscle with intact mosaic patterned myofibres. A: 10X magnification of control muscle section; scale bar = 200 µm. Solid arrowheads denote larger blood vessels and open triangles show individual capillaries within fascicles. Arrow identifies connective tissue separating the lateral and medial *gastrocnemius* heads. B and C: 40X magnifications of regions of interest in Panel A; scale bars = 20 µm. Circle indicates areas of fibres in transverse orientation and.

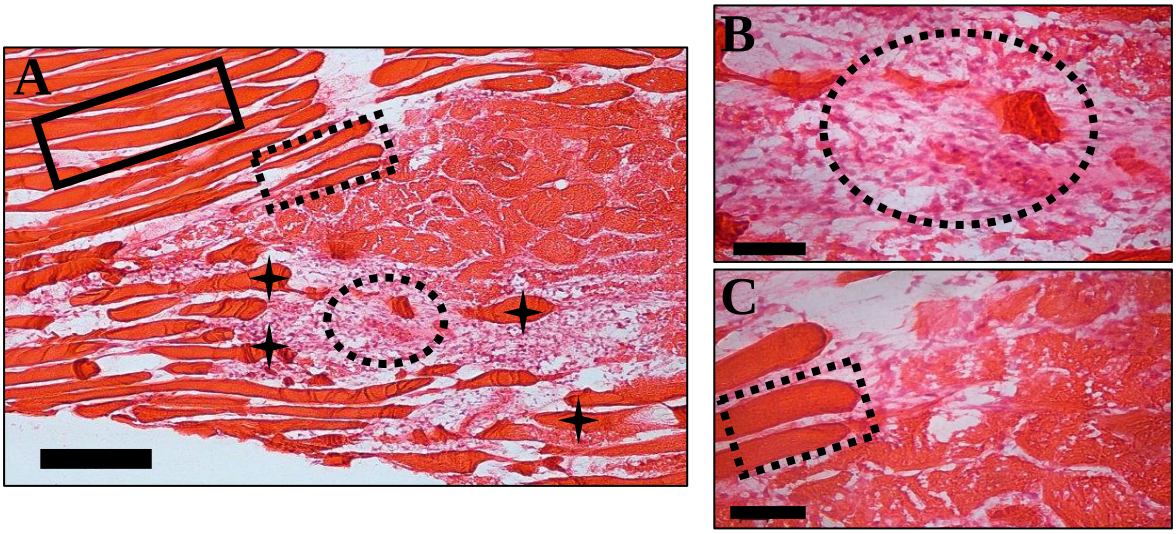

Figure 3.2.3 H&E stained longitudinal sections of *gastrocnemius* skeletal muscle 3 days post crush injury including injured and border zone areas. A: 10X magnification; scale bar = 200 µm. Rectangle indicates area of intact longitudinal fibres in the border zone. Stars indicate areas of extremely fragmented myofibres with immense immune cell infiltration. B and C: 40X magnifications of regions of interest in Panel A (dashed shapes); scale bars = 20 µm. Extensive immune cell infiltration (B) and ruptured myofibres (C) are exhibited.

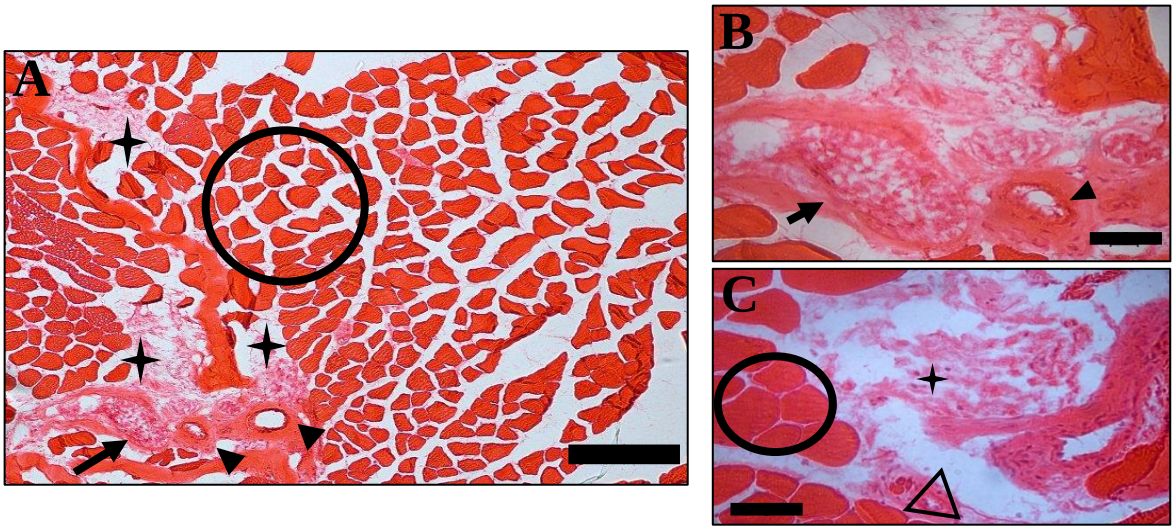

Figure 3.2.4 H&E stained cross-sections of *gastrocnemius* skeletal muscle 3 days post crush injury including injured and border zone areas. A: 10X magnification; scale bar = 200 µm. Circle indicates area of fibres in transverse orientation with oedema-induced spacing between fibres. Solid arrowheads denote blood vessels, the arrow identifies a tendon and stars indicate regions of immune cell infiltration. B and C: 40X magnifications of regions of interest in Panel A; scale bars = 20 µm. Intact polygonal myofibres are circled in the border zone. An open triangle indicates an individual capillary and a larger blood vessel is shown by a solid arrowhead.

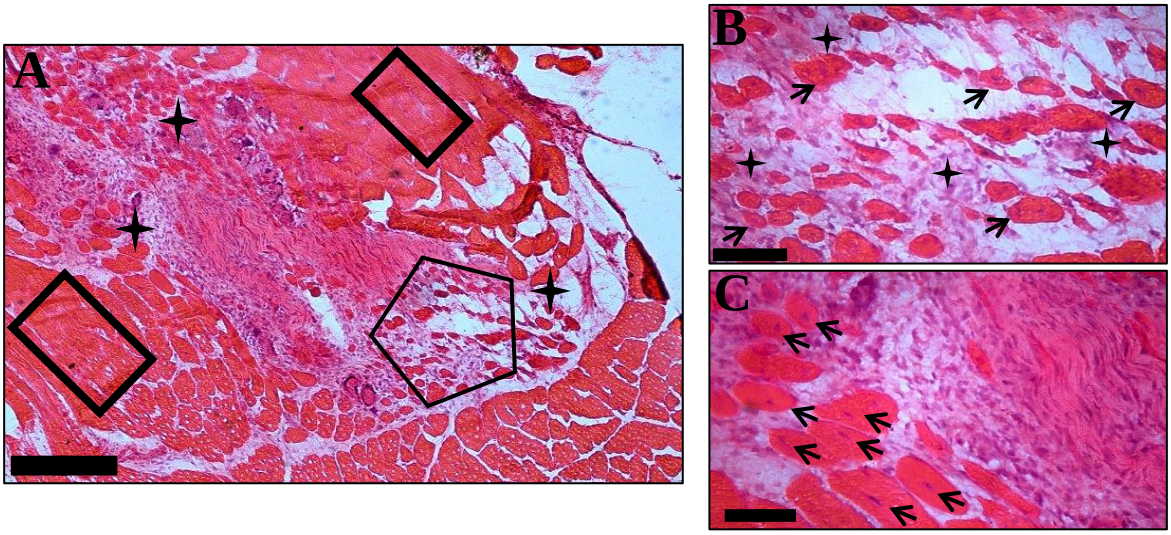

Figure 3.2.5 H&E stained longitudinal sections of *gastrocnemius* skeletal muscle 7 days post crush injury including injured and border zone areas. A: 10X magnification; scale bar = 200 µm. Rectangles indicate areas of intact longitudinal fibres in the border zone. Stars indicate areas of extreme fragmented myofibres with immense immune cell infiltration. Pentagon indicates oedema and necrosis in the impact zone. B and C: 40X magnifications of regions of interest in Panel A; scale bars = 20 µm. Central nuclei of regenerating fibres are shown by arrows.

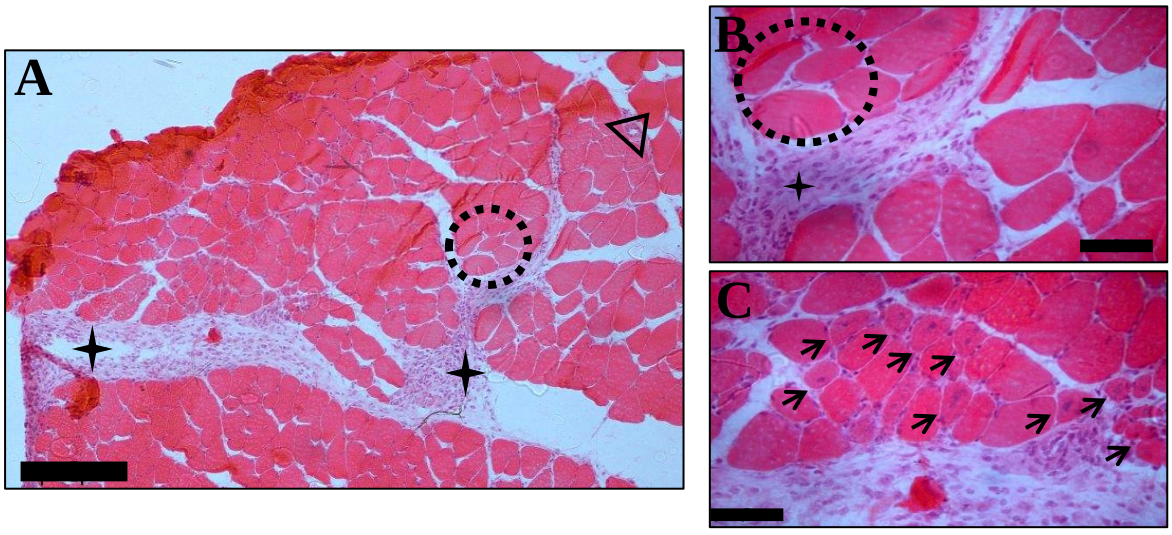

Figure 3.2.6 H&E stained cross-sections of *gastrocnemius* skeletal muscle 7 days post crush injury including areas of injury and regeneration. A: 10X magnification; scale bar = 200 µm. Circle indicates area of intact fibres in transverse orientation in the border zone. The open triangle denotes an individual capillary and stars indicate regions of immune cell infiltration. B and C: 40X magnifications of regions of interest in Panel A (dashed circle); scale bars = 20 µm. Central nuclei of fibres shown by arrows (C).

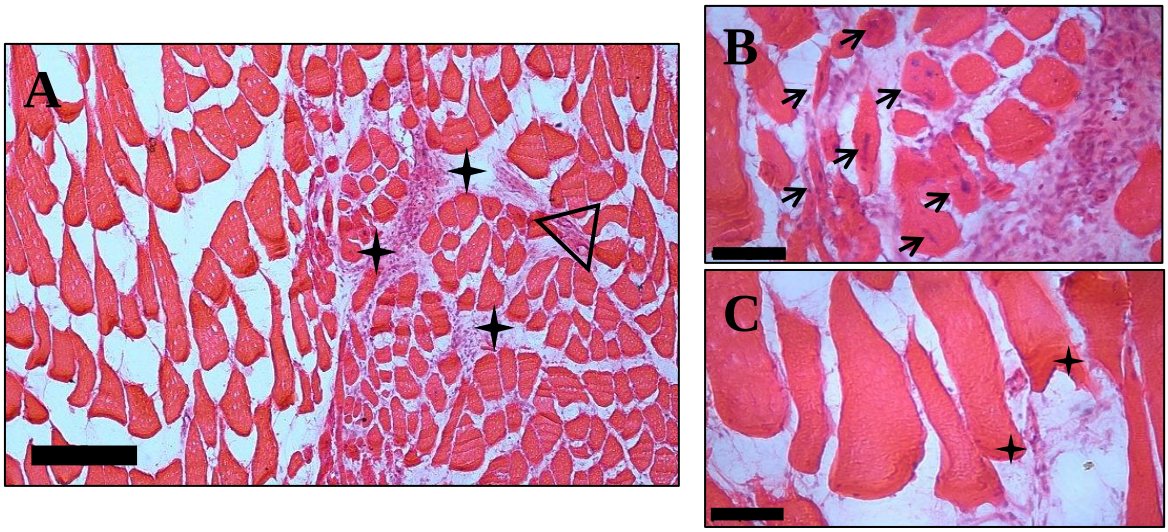

Figure 3.2.7 H&E stained longitudinal sections of the impact zone of *gastrocnemius* skeletal muscle 14 days post crush injury. A: 10X magnification; scale bar = 200 µm. The triangle denotes capillaries in close proximity to each other. Stars indicate regions of immune cell infiltration, and large areas of oedema are visible. B and C: 40X magnifications of regions of interest in Panel A; scale bars = 20 µm. Central nuclei of fibres shown by arrows (B). Loose connective tissue and immune cells remain around regenerating fibres with large irregularly shaped fibres (C).

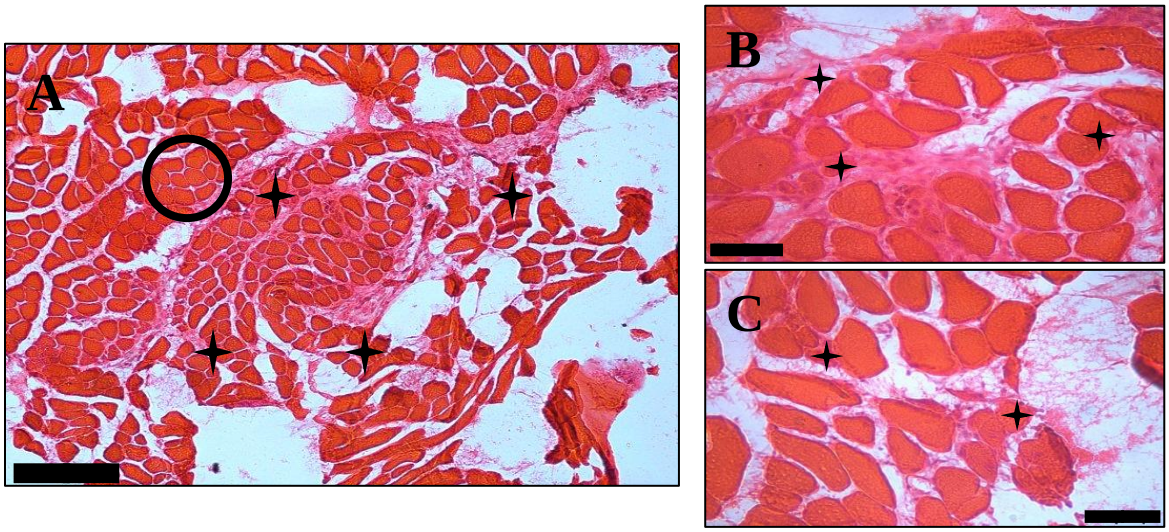

Figure 3.2.8 H&E stained cross-sections of regenerating *gastrocnemius* skeletal muscle 14 days post crush injury. A: 10X magnification; scale bar = 200 µm. Stars indicate regions of remaining immune cells and deposition of connective tissue; large areas of oedema are visible. Circle indicates area of intact fibres in transverse orientation in the border zone. B and C: 40X magnifications of regions of interest in Panel A; scale bars = 20 µm.

3.2.1 Morphological Structure of Healthy *Gastrocnemius*

Longitudinal sections had a combination of parallel longitudinal fibres, diagonal fibres and polygonal transverse fibres due to the bulge shape caused by the belly of the muscle (see Figure 3.2.1). Diagonally- or cross-sectioned fibres were usually visible towards the origin or insertion points of the muscle, which was typically along the border of sections. Fibres were organised and displayed multiple peripheral nuclei along their borders. A sheath surrounding the muscle was clearly exhibited and contained a tendon and large blood vessel. The tendon appeared as a light pink oval with a wavy interior indicating collagen fibres. Groups of small intact round or polygonal myofibres with multiple peripheral nuclei along the fibre borders are clearly visible in cross-sections (see Figure 3.2.2). Capillaries were easily identified in cross-sections as they ran parallel to the myofibres and appeared as delicate rings. Larger blood vessels were also prominent and characterised by the dark pink colour and oval ring shape of their endothelium with purple nuclei (Rubinstein, *et al.*, 1998). Due to the *gastrocnemius* being split into two distinct compartments, the connective tissue that separates the medial and lateral heads was clearly visible.

3.2.2 Morphological Structure of Injured *Gastrocnemius*

Distinct injured regions in both longitudinal and cross-sections were identifiable, with a border zone of less affected tissue alongside the impact zone. The border zone maintained organisation and fibres remained intact. The border zone was still affected by minor immune cell infiltration or exhibited minor oedema in part (see Figure 3.2.3 panel A).

The impact zone displayed far more extreme morphological changes than the border zone. Fragmented myofibres were caused by the sheer force created during the crush injury. This led to extensive immune cell infiltration, oedema-induced spaces, swelling of fibres and in situ necrosis of cells (see Figure 3.2.3 and 3.2.4). Organisation and uniformity of fibres was lost as immune cells attempted to clear debris and repair the area. Migration of inflammatory cells and central nuclei peaked around D7 (see Figures 3.2.5 and 3.2.6) but were still present by D14 (see Figures 3.2.7 and 3.2.8). The number of nuclei present in the interstitial space probably indicate migration of myonuclei and satellite cells. The centralised nuclei indicated that myogenesis was in progress by D7 and continued to D14 when larger myofibres with multiple centralised nuclei could be observed (see Figures 3.2.5 panel B and 3.2.7 panel B). Although to a lesser extent, the border zone underwent myogenesis much like the impact zone. Considerable deposition of loose connective tissue coupled with inflammatory cells was seen around D7 (see Figures 3.2.5 and 3.2.6). However, there appeared to be fewer inflammatory cells present, with the initial hematoma replaced by the loose connective tissue by D14 (see Figure 3.2.8) (Winkler, *et al.*, 2011).

3.3 Effect of Crush Injury on Muscle Force Generation

3.3.1 Uninjured Group Force-Frequency Curves

From of the control group (D0), muscle function force testing was carried out on 5 animals. The 5 control animals all underwent a baseline reading and a repeated reading after a designated time point, but without injury. This was to ascertain whether the baseline force testing would influence any later results when the protocol was repeated. This ensured that any differences seen post-injury could absolutely be attributed to the effects of crush injury.

Of the initial 5 animals, N = 2 were retested at the D7 time point and N = 3 at the D14 time point. There was no significant effect of repeated testing found at any of the stimulation frequencies between the control subgroups (see Figure 3.3.1).

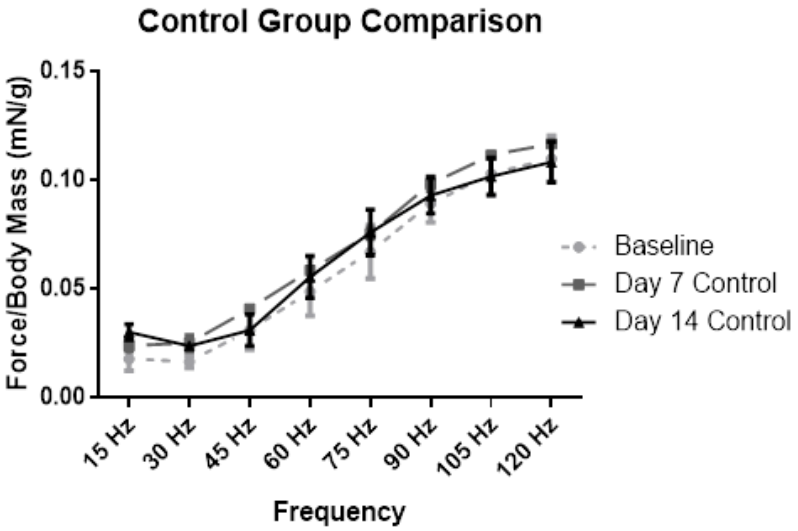

Figure 3.3.1 Force-frequency curve of control uninjured subgroups. Readings carried out at baseline and 7 and 14 days post-baseline reading (no injury). Data expressed as mean ± SD and N = 5 for baseline, N = 2 for D7, and N = 3 for D14. Two-way ANOVA with multiple comparisons indicated no significant differences between subgroups at each frequency.

3.3.2 Injury Group Force-Frequency Curves

Force-frequency curves of the injured groups compared the muscle functional capacity of the animals pre- and post-injury over time, with significant differences seen in all 3 injury groups (Figure 3.3.2). D3 group (see Panel A) decreased following injury. Force produced per body mass by the plantar flexor muscles was highly significantly decreased ($P < 0.0001$) at 60 Hz, 75 Hz, 90 Hz, 105 Hz and 120 Hz.

The D7 group (see Panel B) had a similar decrease ($P < 0.0001$) at 60 Hz, 75 Hz and 90 Hz, and lesser decrease ($P < 0.05$) at 45 Hz and 105 Hz. The pre- and post-injury groups were no longer significantly different at 120 Hz. The D14 group (see Panel C) also displayed a decrease ($P < 0.01$) at 45 Hz and ($P < 0.001$) 105 Hz, and a more marked decrease ($P < 0.0001$) at 60 Hz, 75 Hz and 90 Hz. A return to baseline function was also seen at 120 Hz of the D14 group.

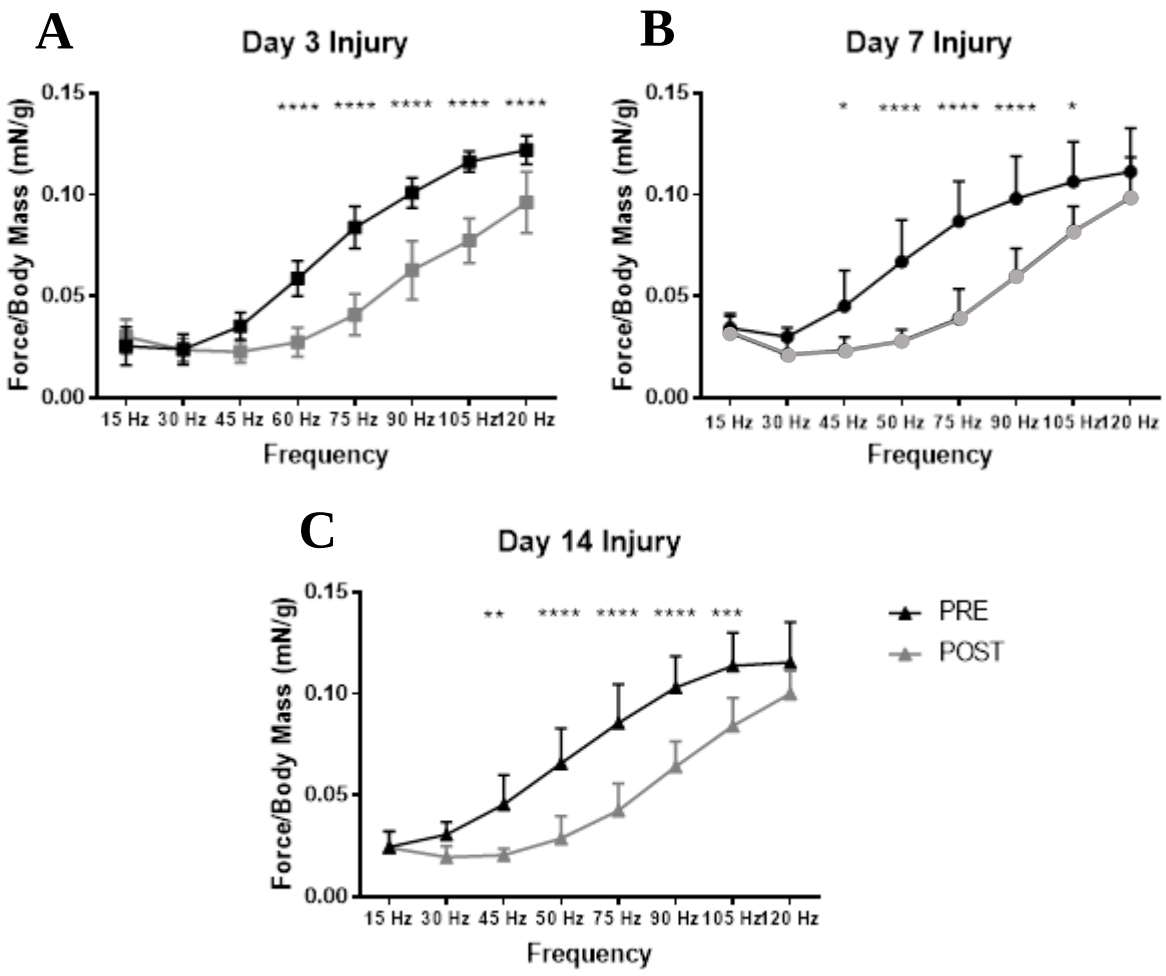

Figure 3.3.2 Force-frequency curves of injury groups over time post-injury. Readings carried out at baseline (PRE) and after 3; 7 and 14 days post-injury (POST). Data expressed as mean ± SD and N = 8 unless otherwise stated. Statistical analyses included two way ANOVA with multiple comparisons. Stars indicate degrees of significance between PRE and POST at each frequency where * = $P < 0.05$; ** = $P < 0.01$; *** = $P < 0.001$ and **** = $P < 0.0001$. A: Longitudinal baseline and 3 day post-injury force-frequency curves. B: Longitudinal baseline and 7 day post-injury force-frequency curves. C: Longitudinal baseline and 14 day post-injury force-frequency curves.

The pre-injury baseline readings of the 3 injury groups were combined with the control baseline readings to produce a mean baseline force-frequency curve of all 34 mice (see Figure 3.3.3 above). The respective post-injury curves of the D3, D7 and D14 groups were then compared against this combined baseline (see Addendum E Table E.2). There was a marked decrease ($P < 0.0001$) in force produced per body mass across all 3 injury groups at 60 Hz, 75 Hz, 90 Hz and 105 Hz.

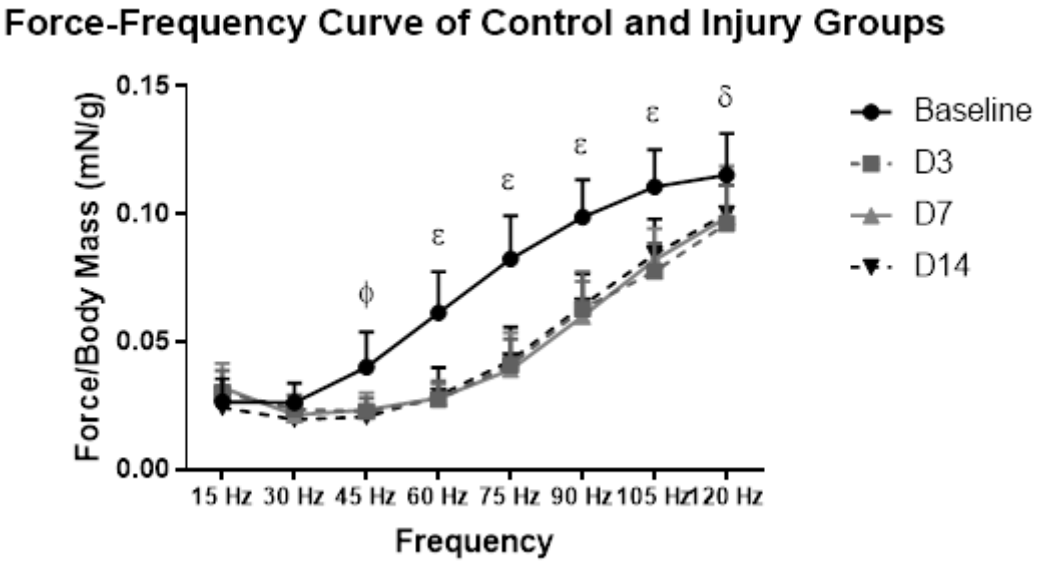

Figure 3.3.3 Force-frequency curves of post-injury groups and combined pre-injury baseline. Combined baseline (N = 34) and 3; 7; and 14 day post-injury groups. ϕ indicates ** between baseline and the D3 and D7 readings, and *** between baseline and D14. ε indicates **** between baseline and all 3 POST time points. σ indicates ** between baseline and the D3 and D7 readings, and * between baseline and D14.

3.3.3 Area Under the Force-Frequency Curve

The area under the curve (AUC) was further calculated to take into consideration the cumulative difference in force produced at all frequencies tested, to facilitate comparison between baseline and post-injury readings (see Figure 3.3.4).

The baseline AUC of each injury group was found to be significantly higher when compared to their respective post-injury AUC ($P < 0.0001$). While the individual force-frequency curves (representative of the maximum force/body mass) of each injury group displayed an apparent return to baseline at 120 Hz for D7 and D14 (see Figure 3.3.2 B and C), the AUC shows that the cumulative difference across all frequencies was still markedly reduced at D3, D7 and D14 (see Figure 3.3.4).

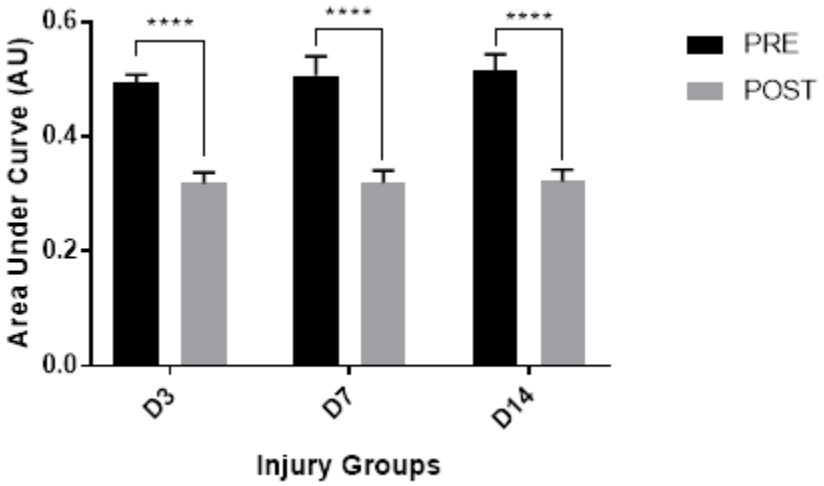

Figure 3.3.4 Cumulative force-frequency data of injury groups. Data expressed as mean ± SD and N = 8. Two-way ANOVA carried out with multiple comparisons. Stars indicate degrees of significance between PRE and POST at each time point where **** = P < 0.0001

3.4 Presence of MuSK in Plasma

A standard curve generated from the mean OD for each standard was fit to a sigmoidal curve (see Figure 3.4.1 below) with an r value of 0.9878. Considering the mean OD for each concentration of the standard curve (see Addendum E Table E.3), the range of the first 3 was similar to the range of the OD for samples from the mice (0.23 – 0.85). The OD of mice samples was therefore within the detection range specified.

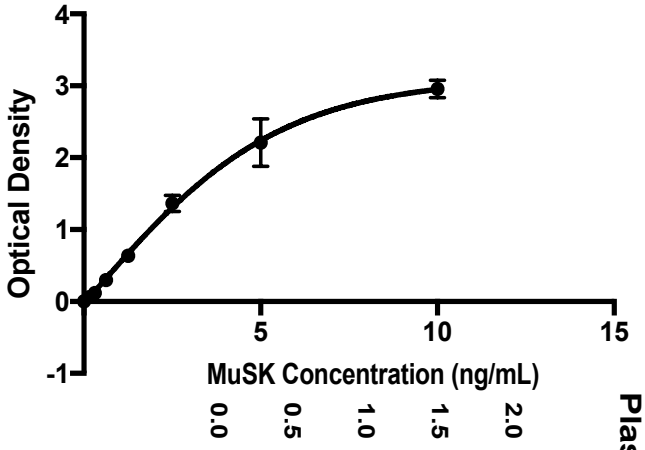

Figure 3.4.1 Standard curve for M s means ± SD of OD for MuSK concentrations prepared by icates of each standard concentration were run on the san curve. Standard curve concentrations used were 10 ng/mL 5 ng/mL, 0.312 ng/mL, 0.156 ng/mL and a blank.

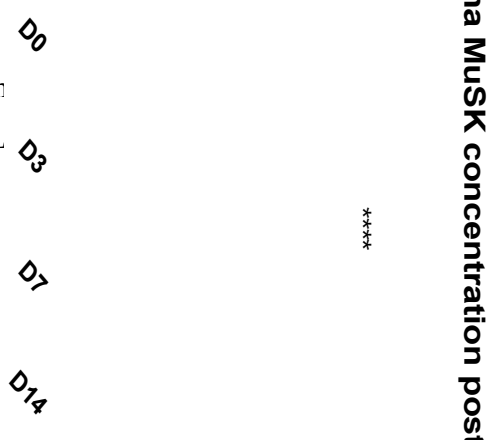

Control samples (D0) had 0.23 ng/mL MuSK in plasma. A rise in the concentration of plasma MuSK occurred after injury and peaked at 14 days post-injury (see Figure 3.4.2 below) with a 5-fold increment by D14 ($P < 0$ **Plasma MuSK concentration post-injury** < 0.0001).

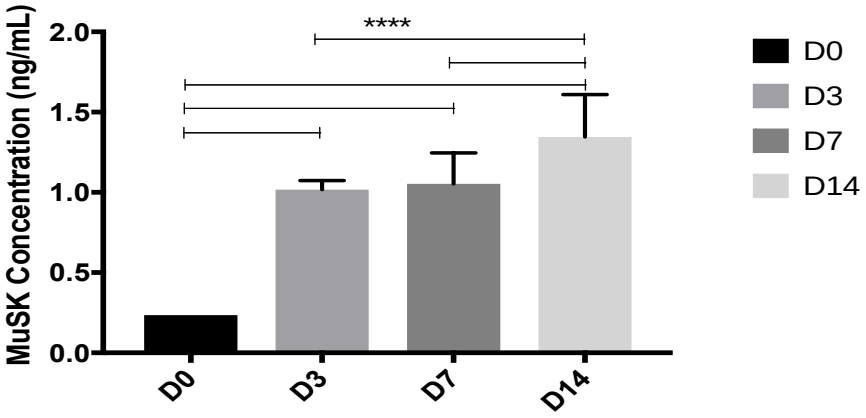

Figure 3.4.2 Differences in plasma MuSK concentration of pre-injury and post-injury mice. ELISA data are presented as means of plasma MuSK ± SE (N = 10 for D0, and N = 8 for D3, D7 and D14). One-way ANOVA with multiple comparisons. **** indicate $P < 0.0001$ for all between-group differences.

3.5 Effect of Crush Injury on Synapse

3.5.1 Morphology of Post-synaptic Region of Synapse

Immunostaining was carried out on injured and un-injured samples to investigate the presence and distribution of the AChR and its associated post-synaptic proteins. Many simplistic diagrams have alluded to neat co-localisation of the post-synaptic components (Rudolf, 2014) (Yamanashi, *et al.*, 2008). However, there is insufficient experimental literature presenting this assumption. The spatial signal profiles of rapsyn (Figures 3.5.1 and 3.5.2), MuSK (Figures 3.5.3 and 3.5.4), LRP4 (Figures 3.5.5 and 3.5.6) and Dok7 (Figures 3.5.7 and 3.5.8) in tandem with the AChR are presented across injury groups.

Of the post-synaptic proteins, rapsyn has been established as a primary AChR associated protein (Ramarao, *et al.*, 2001). This was clearly exhibited in the current study as well by co-localisation of rapsyn with AChR in the D0 group (see Figures 3.5.1 A and 3.5.2 A). AChR of the D0 group displayed the characteristic coral-like architecture that has been widely presented in literature (Rudolf, 2014), with rapsyn presenting a nearly identical staining profile. As expected, uninjured tissue also had peripheral nuclei along the fibre borders and beneath the AChRs. A loss in normal AChR structure with fragmented, complex and ill-defined borders was seen at D3 (Figures 3.5.1 B and 3.5.2 B).

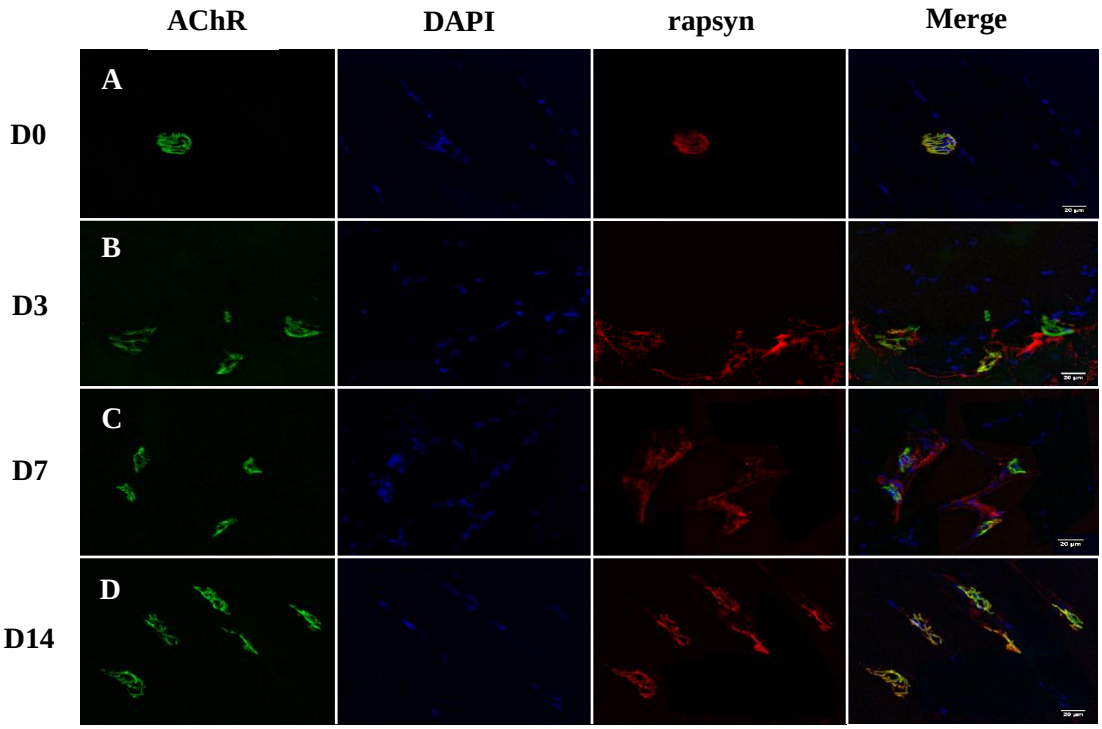

Figure 3.5.1 Longitudinal sections of *gastrocnemius* skeletal muscle with AChR stained with α-Btx conjugated fluorophore (green), nuclei stained with DAPI (blue) and rapsyn stained with primary and secondary antibodies (red). 40X magnification; scale bars = 20 μm. A: Uninjured (D0). B: 3 days post-injury (D3). C: 7 days post-injury (D7). D: 14 days post-injury (D14).

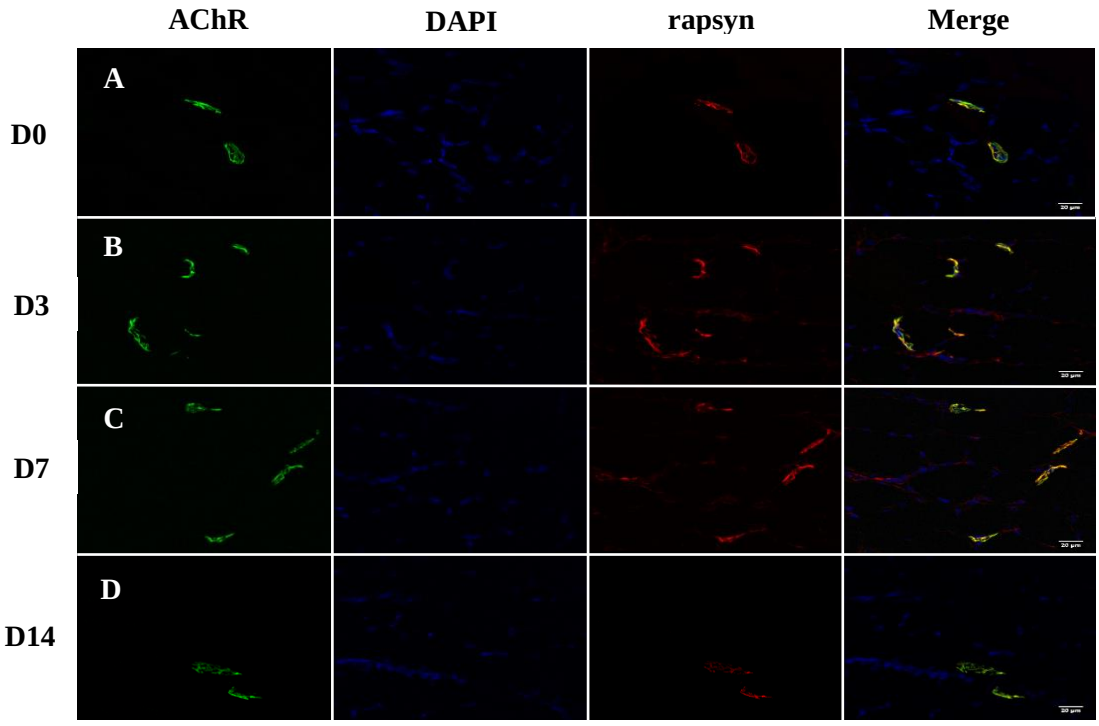

Figure 3.5.2 Cross sections of *gastrocnemius* skeletal muscle with AChR stained with α-Btx conjugated fluorophore (green), nuclei stained with DAPI (blue) and rapsyn stained with primary and secondary antibodies (red). 40X magnification; scale bars = 20 μm. A: Uninjured (D0). B: 3 days post-injury (D3). C: 7 days post-injury (D7). D: 14 days post-injury (D14).

Rapsyn protein had more disruption, with dispersion further afield of the post-synaptic region (for quantification, see Section 3.5.2 later), but also still maintained signal expression at the sites of the AChRs. Nuclei were no longer limited to the periphery of fibres (see Figure 3.5.1 B). This is in line with the morphology presented in Figure 3.2.5. The D7 group AChRs appeared to be somewhat more compact than those of D3 but still lacked concise borders (see Figure 3.5.1 C). Rapsyn was still dispersed from the AChR sites, along with nuclei clustering (see Figure 3.5.2 C).

By D14, normal structure had begun to be re-established, with an increase in AChR size from D7 (see Figures 3.5.1 D and 3.5.2 D). Uniformity of fibres returned, with nuclei present along the periphery and far less dispersion of rapsyn (see Figure 3.5.1 D). The rapsyn and AChR again exhibited similar signal profiles, indicating a return to what was seen at D0 (see Figures 3.5.2 A and D).

MuSK has been described as an essential receptor associated protein due to its critical role in AChR clustering, formation and maintenance (Hubbard & Gnanasambandan, 2013). Diagrams often depict its position as being closely related to the receptor (Punga & Reugg, 2012) and this relationship was also exhibited in the immunohistochemical data with co-localisation of MuSK and AChR signal in the D0 group (see Figures 3.5.3 A and 3.5.4 A).

Similar to rapsyn signal expression, MuSK and AChR showed matching pretzel shaped signal in uninjured tissue (see Figure 3.5.3 A). D3 damage resulted in disintegration of AChR structure and a loss of co-localisation with MuSK signal (see Figures 3.5.3 B and 3.5.4 B). At D3, the extent of MuSK dispersion appeared far worse when compared to that of rapsyn. The MuSK signal was broadly distributed and was also found in areas with nuclei clustering (see Figure 3.5.3 B), where one would expect the impact zone to be (see Figure 3.2.3).

A loss of co-localisation between MuSK and the AChR signal was still apparent at D7 in the longitudinal section, however the AChR structure appeared to have improved (see Figure 3.5.3 C). While there appeared to be an improved return in co-localisation in the cross section, AChR structure was still fairly fragmented and compact (see Figure 3.5.4 C). The nuclei arrangement in the longitudinal section at D14 suggested restored uniformity of regenerated fibres (see Figure 3.5.3 D). AChR structure began to resemble its normal appearance by D14, along with its overlapping MuSK signal in both the cross- and longitudinal sections (see Figures 3.5.3 D and 3.5.4 D). However, minor MuSK dispersion remained visible in the cross section (see figure 3.5.4 D).

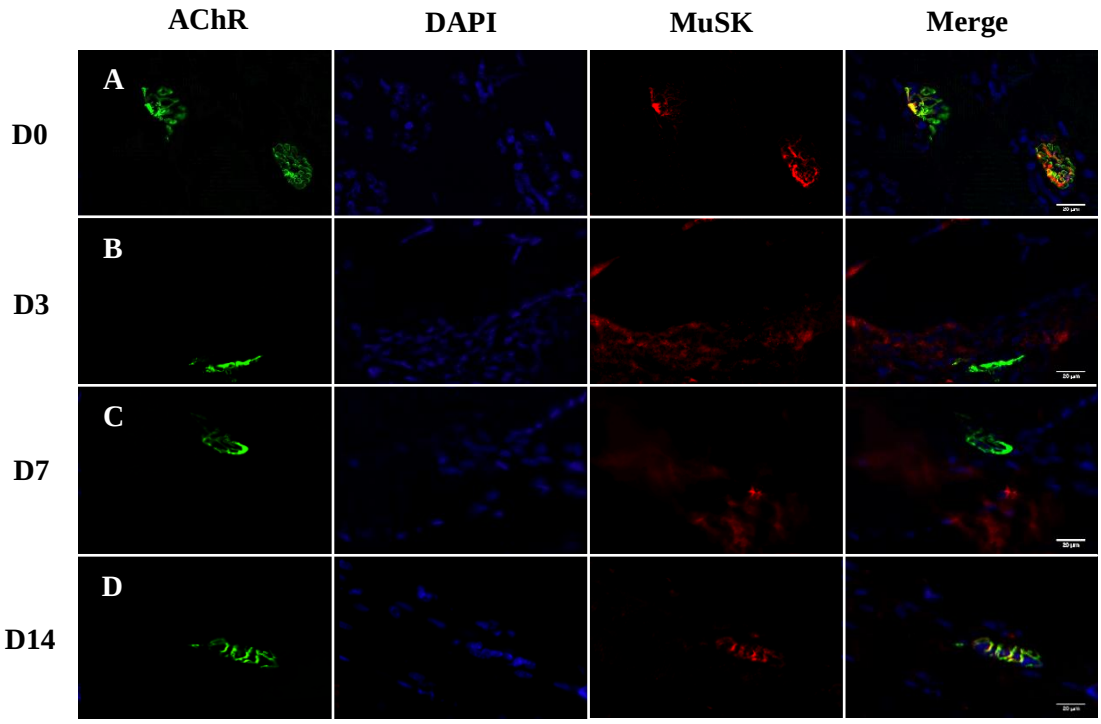

Figure 3.5.3 Longitudinal sections of *gastrocnemius* skeletal muscle with AChR stained with α-Btx conjugated fluorophore (green), nuclei stained with DAPI (blue) and MuSK stained with primary and secondary antibodies (red). 40X magnification; scale bars = 20 µm. A: Uninjured (D0). B: 3 days post-injury (D3). C: 7 days post-injury (D7). D: 14 days post-injury (D14).

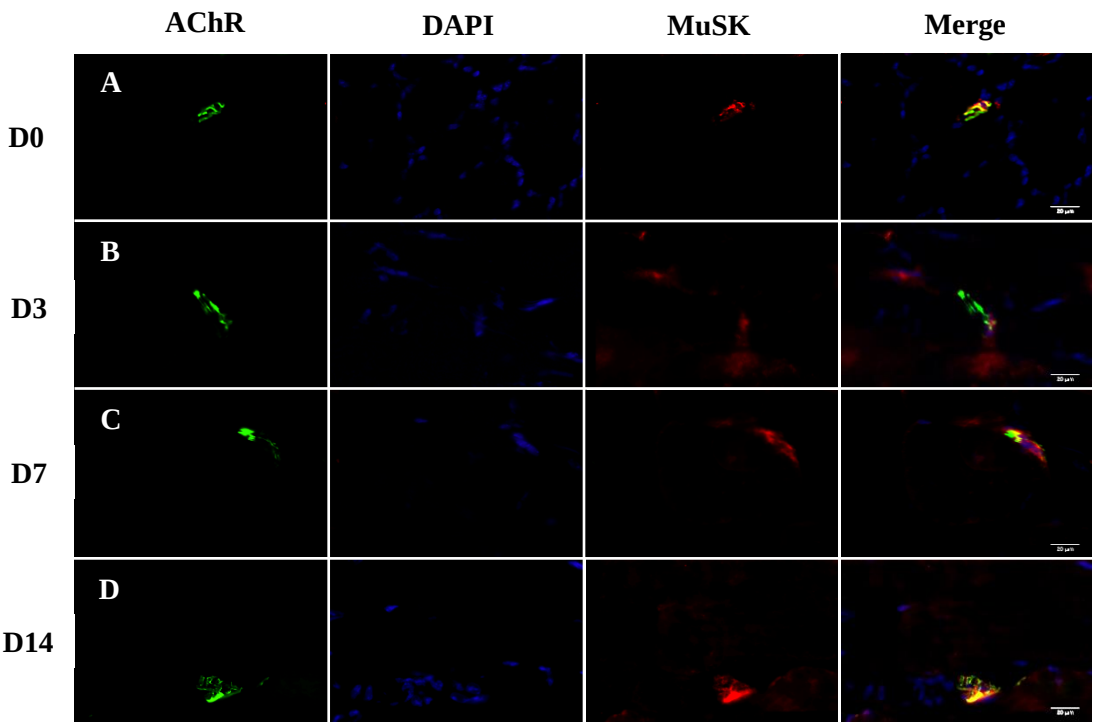

Figure 3.5.4 Cross sections of *gastrocnemius* skeletal muscle with AChR stained with α-Btx conjugated fluorophore (green), nuclei stained with DAPI (blue) and MuSK stained with primary and secondary antibodies (red). 40X magnification; scale bars = 20 µm. A: Uninjured (D0). B: 3 days post-injury (D3). C: 7 days post-injury (D7). D: 14 days post-injury (D14).

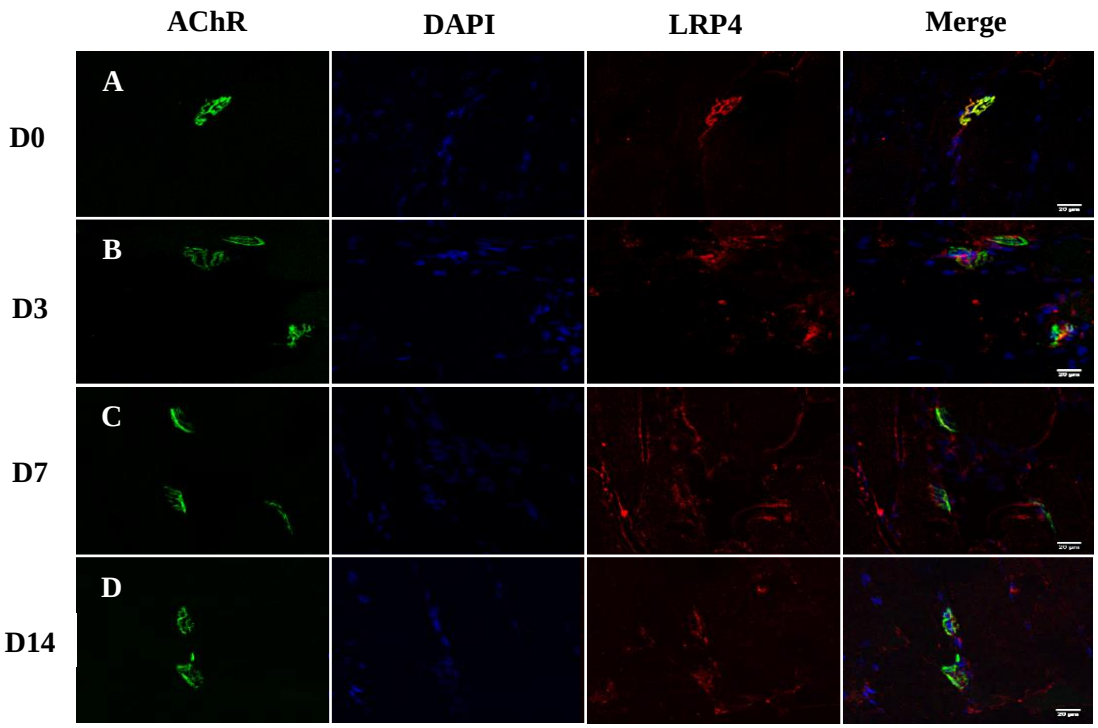

Figure 3.5.5 Longitudinal sections of *gastrocnemius* skeletal muscle with AChR stained with α-Btx conjugated fluorophore (green), nuclei stained with DAPI (blue) and LRP4 stained with primary and secondary antibodies (red). 40X magnification; scale bars = 20 μm. A: Uninjured (D0). B: 3 days post-injury (D3). C: 7 days post-injury (D7). D: 14 days post-injury (D14).

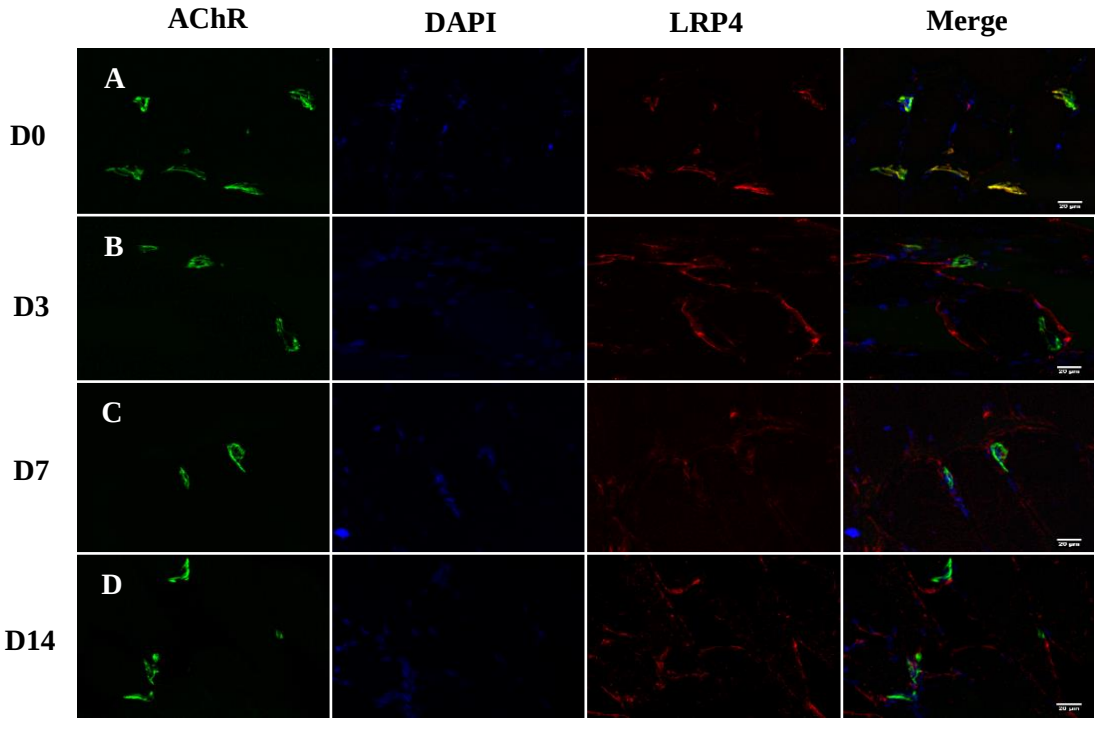

Figure 3.5.6 Cross sections of *gastrocnemius* skeletal muscle with AChR stained with α-Btx conjugated fluorophore (green), nuclei stained with DAPI (blue) and LRP4 stained with primary and secondary antibodies (red). 40X magnification; scale bars = 20 μm. A: Uninjured (D0). B: 3 days post-injury (D3). C: 7 days post-injury (D7). D: 14 days post-injury (D14).

LRP4 acts as a co-receptor for and has been shown to associate with MuSK (Zhang, *et al.*, 2008). However, its position in relation to the AChR has yet to be fully established. Immunohistochemical data presented here showed that LRP4 also displayed a similar signal profile to the AChR with co-localisation of their signals present in D0 (see Figures 3.5.5 A and 3.5.6 A). However, LRP4 signal was not as neatly confined to the AChR area as previously exhibited with rapsyn and MuSK (see Figures 3.5.1 A and 3.5.3 A).

Extensive dispersion of LRP4 post-injury was seen in the longitudinal sections of D3 (see Figure 3.5.5 B), however increased LRP4 signal was still maintained at the AChR sites. Widespread dispersion of LRP4 was seen in the cross section of D3 but was not accompanied by increased signal expression at the AChR sites (see Figure 3.5.6 B). The longitudinal section of D7 displayed very similar characteristics to its D3 counterpart (see Figures 3.5.5 B and C), with broad LRP4 signal across the disrupted fibres. The cross section of D7 showed early stages of fibre uniformity returning, with LRP4 signal still dispersed, but limited to the membrane (see Figure 3.5.6 C).

Unlike rapsyn and MuSK (see Figures 3.5.1 D and 3.5.3 D), there was no substantial reduction in extra-synaptic LRP4 signal by D14 (see Figure 3.5.5 D). However, increased LRP4 signal expression at AChR sites suggested the beginning of AChR-LRP4 recoupling (see Figures 3.5.5 D and 3.5.6 D).

Due to Dok7 binding to MuSK (Hubbard & Gnanasambandan, 2013), a similar distribution to that of MuSK and LRP4 could be anticipated (see Figures 3.5.3 and 3.5.5). Dok7 however, is a cytoplasmic adaptor protein (Muller, *et al*., 2010), while MuSK and LRP4 are transmembrane proteins *(Zhang, et al.*, 2008). Subsequently, one would expect a difference in Dok7's distribution profile compared to the other post-synaptic proteins, particularly in relation to the AChR. There were notable differences between Dok7 location in longitudinal and cross sections of uninjured tissue. The longitudinal section of D0 showed Dok7 signal in the region of the AChR, but no co-localisation (see Figure 3.5.7 A). The cross section of D0 exhibited more expansive distribution of Dok7 that was present at the sites of the AChR, but also along extra-synaptic membranous regions (see Figure 3.5.8 A).

D3 Dok7 signal was extensively dispersed as expected (see Figures 3.5.7 B and 3.5.8 B. Dok7 dispersion remained at D7 but was accompanied by increased signal at the AChR sites and nuclei clustering in the expected injury zone (see Figures 3.5.7 C and 3.5.8 C). By D14, Dok7 was less dispersed, but still found outside the AChR sites in membranous regions (see Figures 3.5.7 D and 4.5.8 D). The increased Dok7 intensity at AChR sites seen at D7 had dissipated by D14 (see Figures 3.5.7 C and D).

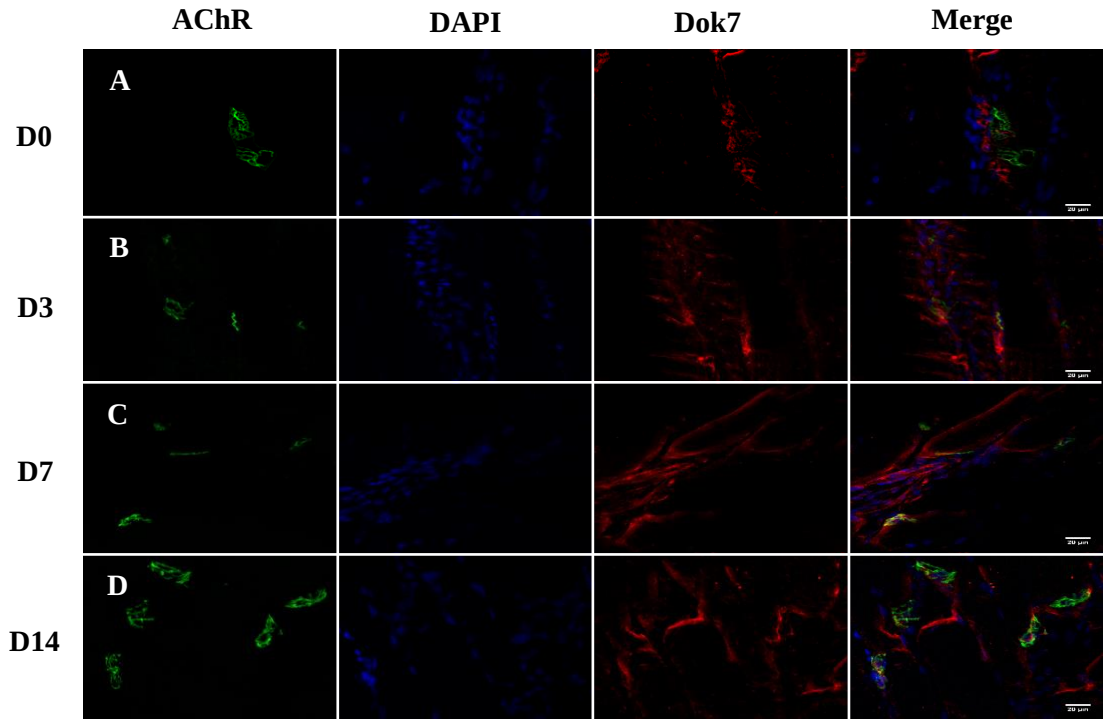

Figure 3.5.7 Longitudinal sections of *gastrocnemius* skeletal muscle with AChR stained with α-Btx conjugated fluorophore (green), nuclei stained with DAPI (blue) and Dok7 stained with primary and secondary antibodies (red). 40X magnification; scale bars = 20 μm. A: Uninjured (D0). B: 3 days post-injury (D3). C: 7 days post-injury (D7). D: 14 days post-injury (D14).

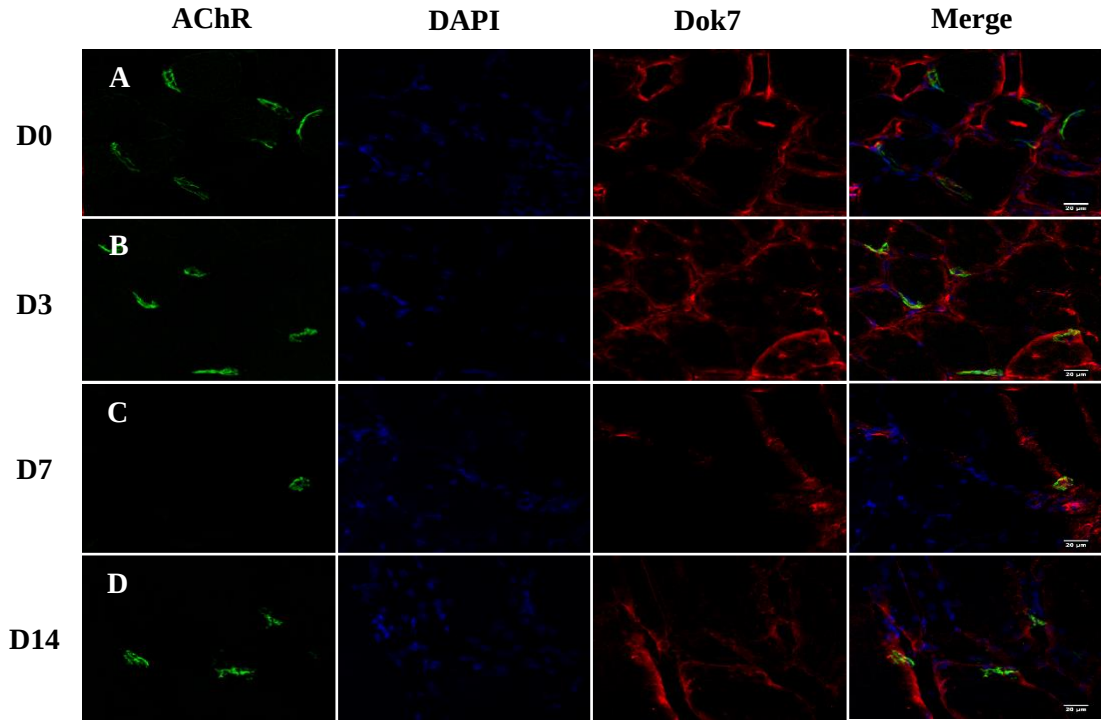

Figure 3.5.8 Cross sections of *gastrocnemius* skeletal muscle stained with α-Btx labelled AChRs (green), nuclei (blue) and Dok7 (red). 40X magnification; scale bars = 20 μm. A: Uninjured section (D0). B: Injured section 3 days post-injury (D3). C: Injured section 7 days post-injury (D7). D: Injured section 3 days post-injury (D14).

In summary, qualitative differences in spatial signal profiles of the synaptic proteins indicated that the effects experienced following the crush injury varied between proteins and across time points. Quantitative measures were used to better understand the different responses to injury across groups.

The quantitative measures utilised included:

- Total outlined area (TOA): indicating overall shape
- Total stained area (TSA): indicating area of positive pixel signal
- Staining intensity (SI): mean pixel intensity within a ROI
- Staining density (SI/TSA)

3.5.2 Quantified Variables of Post-synaptic Region of Synapse

Due to the selection criteria for NMJs, only the longitudinal section images were processed (see Section 2.4.4.4 and Appendix C). Staining intensities and areas were measured and co-localisation between the AChR and its respective associated synaptic protein was calculated for all time points.

Rapsyn's close interaction with the AChR under normal conditions (see Figure 3.5.1 A) was confirmed by TOA and TSA readings in close proximity to each other (see Figures 3.5.9 A and B; time 0) indicating that their morphology profiles mimicked each other. A lower staining density was observed due to the lower SI of rapsyn (see Figure 3.5.9 C; time point 0). This may be due to several factors such as primary antibody and secondary antibody influences on pixel brightness, or protein quantity. These two synaptic components had marked differences in their response to injury. Opposite acute effects in response to injury were observed, particularly for the parameters of area.

At D3 rapsyn underwent vast dispersion (see Figure 3.5.1 B) with a sharp increase in both TOA and TSA, while the AChR appeared to disintegrate with a decrease in TOA and TSA (see Figures 3.5.9 A and B). Even though the SI of the AChR decreased at D3, its considerable decrease in TSA meant that the calculated staining density increased (see Figure 3.5.9 C). Rapsyn SI was also decreased but coupled with its increase in TSA, a decrease in its staining density was observed (see Figure 3.5.9 C).

The return to a more normal morphology was presented at D7 and D14, however the time course differed between AChR and rapsyn. TSA of rapsyn returned to its control value by D7 and remained there at D14, but the TOA decreased to below the control at D7 (see Figure 3.5.9 A and B). This indicated a return to a more compact structure. The AChR TSA and TOA only returned to control by D14 when it realigned with rapsyn morphology (see Figures 3.5.9 A and B).

The simultaneous decrease in rapsyn and increase in AChR TSA after the divergent D3 responses, ensured their staining densities became much closer to normal by D14. However, an overall increase in rapsyn and decrease in AChR SI resulted in rapsyn density being greater at D14 than D0 and also greater than the AChR D14 value. The AChR density, in contrast, was less that its own baseline D0 value (see Figure 3.5.9 C).

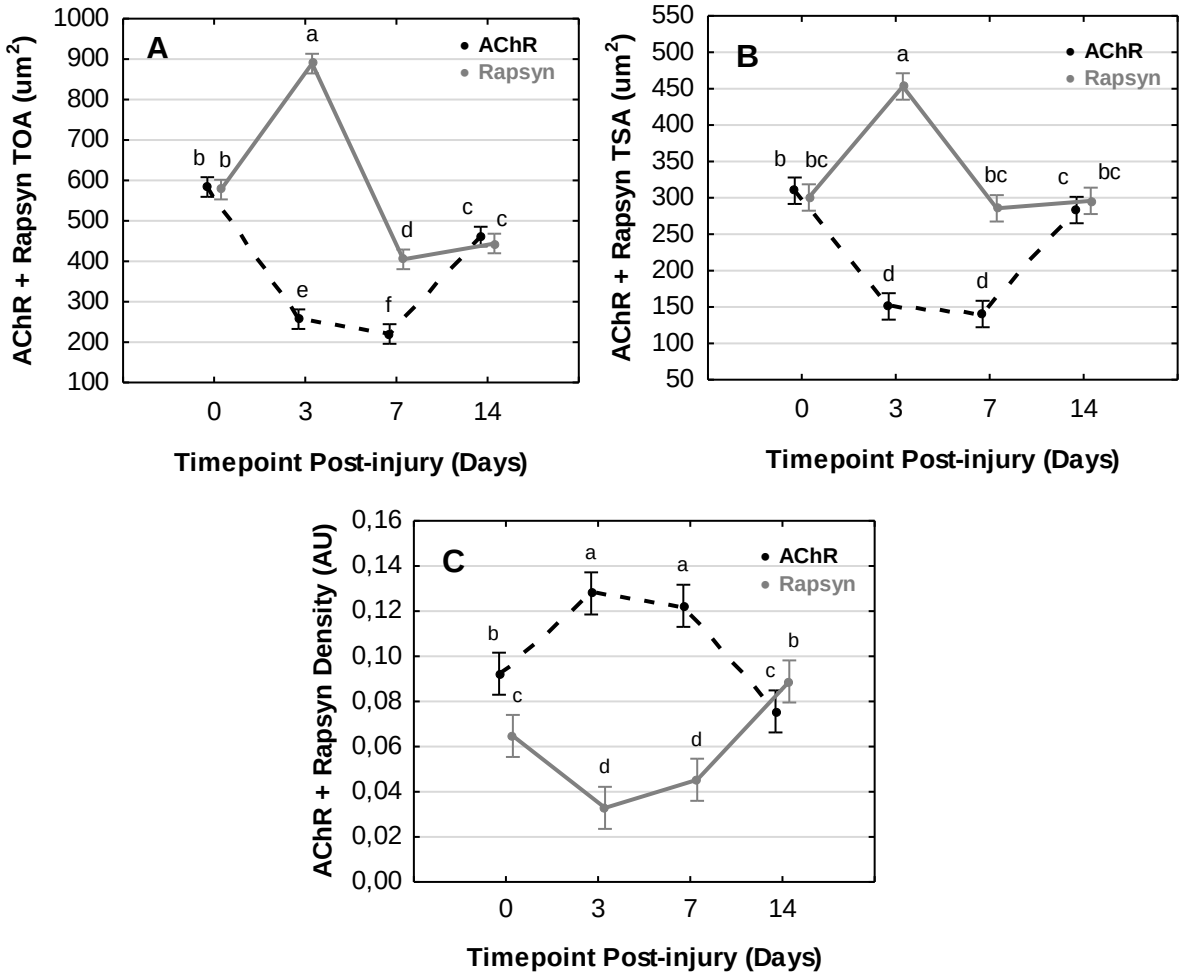

Figure 3.5.9 Quantitative measurements for rapsyn from IHC images pre- and post-injury. Image analyses for AChR and rapsyn carried out on samples from animals sacrificed at D0, and at D3; 7 and 14 post-injury. Data expressed as mean ± 0.95 confidence intervals. Statistical analyses included a Fixed Effect and LSD Test, and at least $P < 0.01$ was reported as significant. Lower case letters indicate significance between points that are labelled with differing letters. Points that denoted the same lower case letters were not significantly different from one another. A: Total Outlined Area. B: Total Stained Area. C: Staining Density (TSA/SI).

MuSK displayed a similar morphology to AChR under normal conditions (for qualitative image, see Figure 3.5.3 A) with similar TOA and TSA readings at D0 (for quantitative variables, see Figures 3.5.10 A and B). Much like rapsyn's response, injury increased MuSK TOA and TSA considerably at D3 (see Figures 3.5.10 A and B). Both variables began to normalise at D7 (see Figures 3.5.10 A and B). However, the MuSK TSA returned to control value by D14, while TOA did not return to control. Nonetheless, MuSK TOA did realign with the AChR TOA at D14 (see Figure 3.5.10 A).

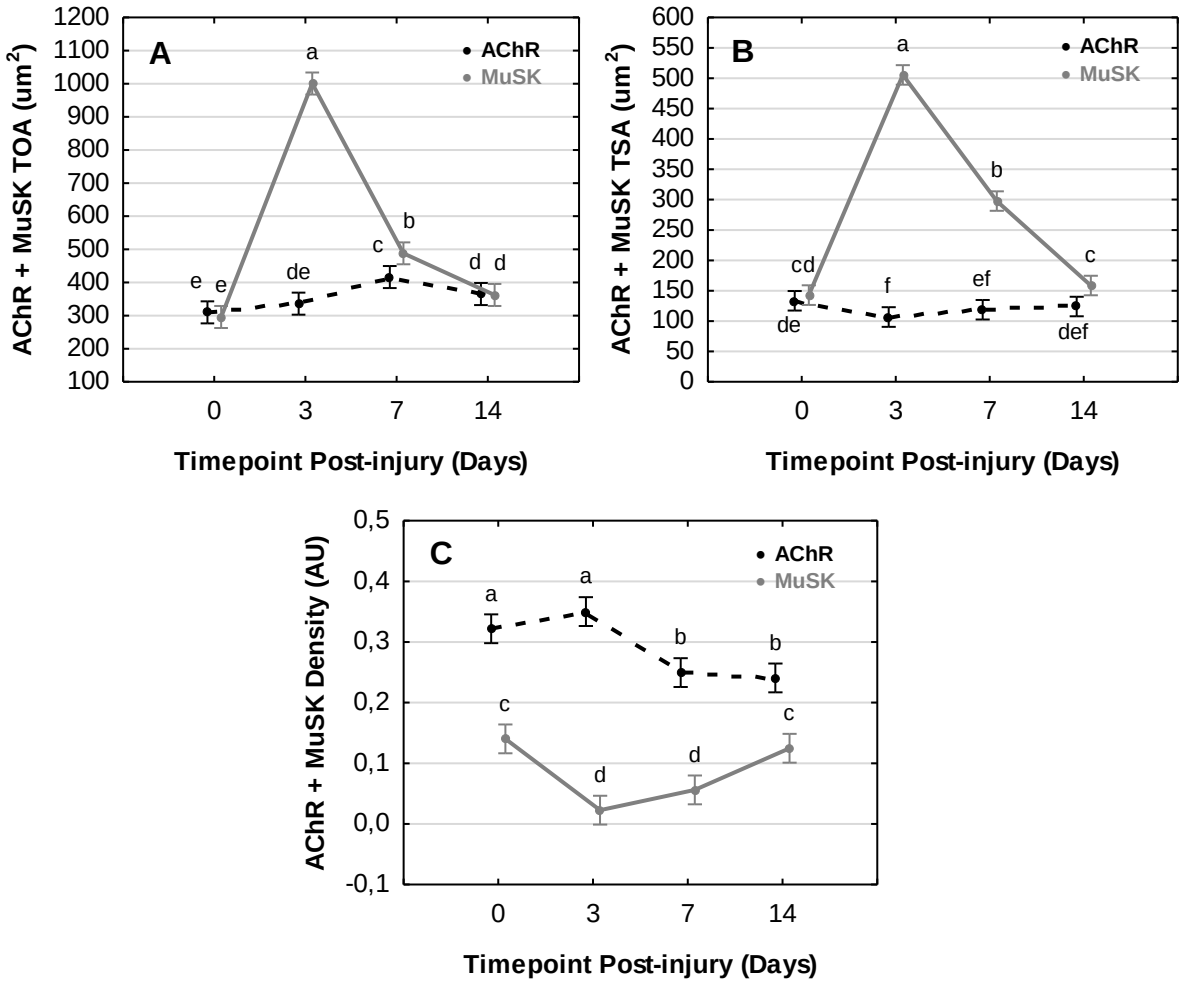

Figure 3.5.10 Quantitative measurements for MuSK from IHC images pre- and post-injury. Image analyses for AChR and MuSK carried out on samples from animals sacrificed at D0, and at 3; 7 and 14 post-injury. Data expressed as mean ± 0.95 confidence intervals. Statistical analyses included a Fixed Effect and LSD Test, and $P < 0.01$ was reported as significant. Lower case letters indicate significance between points that are labelled with differing letters. Points that denoted the same lower case letters were not significantly different from one another. A: Total Outlined Area. B: Total Stained Area. C: Staining Density (TSA/SI).

Another point to note, was that MuSK appeared to change more with injury (D3) than the AChR, indicating it could be more sensitive to dispersion when compared to the AChR. The large difference between the staining density of MuSK and the AChR across all timepoints can be attributed to the significantly increased SI in the AChR when compared to MuSK (see Figure 3.5.10 C below).

The AChR experienced a decrease in SI following injury that did not reconcile by D14, and as a result the density at D7 and D14 was abated. MuSK underwent less drastic changes in SI across the timepoints, however the spike in TSA at D3 caused a drop in density before returning at D14.

LRP4 again expressed a similar relationship with AChR in healthy skeletal muscle tissue as previously exhibited by rapsyn and MuSK (see Figures 3.5.1 A; 3.5.3 A and 3.5.5 A). The TOA and TSA interestingly differed in that at D0, the TOA of LRP4 and AChR signal was comparable, but the TSA of LRP4 appeared to be lower than its AChR counterpart (see Figures 3.5.11 A and B below).

MuSK's reduced TSA (and SI), but similar TOA could potentially be attributed to the somewhat tapered signal seen along the junctional folds. The proportional difference in LRP4 and AChR signal across the SI and TSA at D0 resulted in similar values for their respective staining densities (see Figure 3.5.11 C below).

Both the TOA and TSA of LRP4 spiked in response to the crush injury at D3, peaking at D7 and initiated its return to control by D14 (see Figures 3.5.11 A and B). The AChR experienced slight dispersion in its signal as its TOA gradually increased at D3 and D7, while its TSA saw a modest decrease at the same timepoints (see Figures 3.5.11 A and B). By D14, the AChR presented as a more compact structure with its TOA and TSA both lower when compared to D0 (see Figures 3.5.11 A and B).

The marked decrease in staining density exhibited by LRP4 at D3 and D7 was caused by the inflated TSA with only a minor increase in SI. LRP4's density normalises at D14 and was greater when compared to its D0 value due to a decreased TSA coupled with an increased SI (see Figures 3.5.11 C).

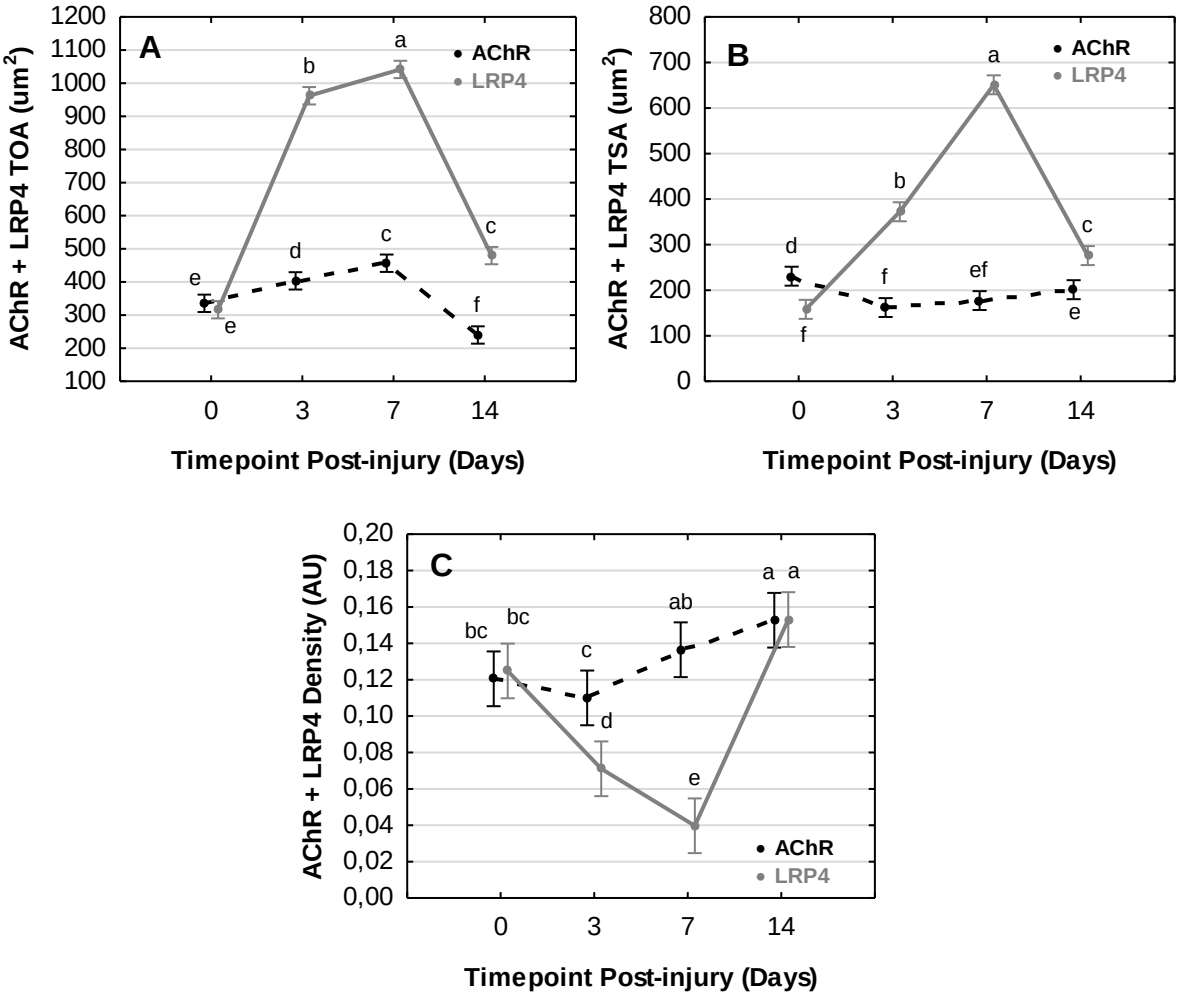

Figure 3.5.11 Quantitative measurements for LRP4 from IHC images pre- and post-injury. Image analyses for AChR and LRP4 carried out on samples from animals sacrificed at D0, and at D3; 7 and 14 post-injury. Data expressed as mean ± 0.95 confidence intervals. Statistical analyses included a Fixed Effect and LSD Test, and $P < 0.01$ was reported as significant. Lower case letters indicate significance between points that are labelled with differing letters. Points that denoted the same lower case letters were not significantly different from one another. A: Total Outlined Area. B: Total Stained Area. C: Staining Density (TSA/SI).

AChR signal was not co-localised with Dok7 at D0, instead Dok7 signal was seen adjacent to the AChR (see Figure 3.5.7 A). Their signal profiles also did not closely match each other and subsequently their TOA and TSA values at D0 differed (see Figures 3.5.12 A and B). The moderate decrease in Dok7 TSA compared to that of the AChR at D0 was cancelled out by the decreased Dok7 SI. AChR and Dok7 showed similar values in staining density at D0 (see Figure 3.5.12 C).

TOA and TSA of Dok7 experienced a sharp increase at D3 but declined significantly by D7 (see Figures 3.5.12 A and B). A return to control was seen in the TOA at D14, but not in the TSA (see Figures 3.5.12 A and B). Even though Dok7 experienced a significant increase in SI at D3, it was mitigated by the considerable increase in TSA, hence its staining density decreased from D0 to D3 (see Figure 3.5.12 C). Staining density of Dok7 began to normalise at D7, but surprisingly decreased again at D14 (see Figure 3.5.12 C). This was due to a return to control of the SI coupled with a raised TSA. The AChR density followed a similar trend to that of the Dok7 density; however it was as a result of reversed responses of its variables. AChR SI and TSA decreased in proportion following injury (D3) before returning to control by D14 (see Figure 3.5.12 C).

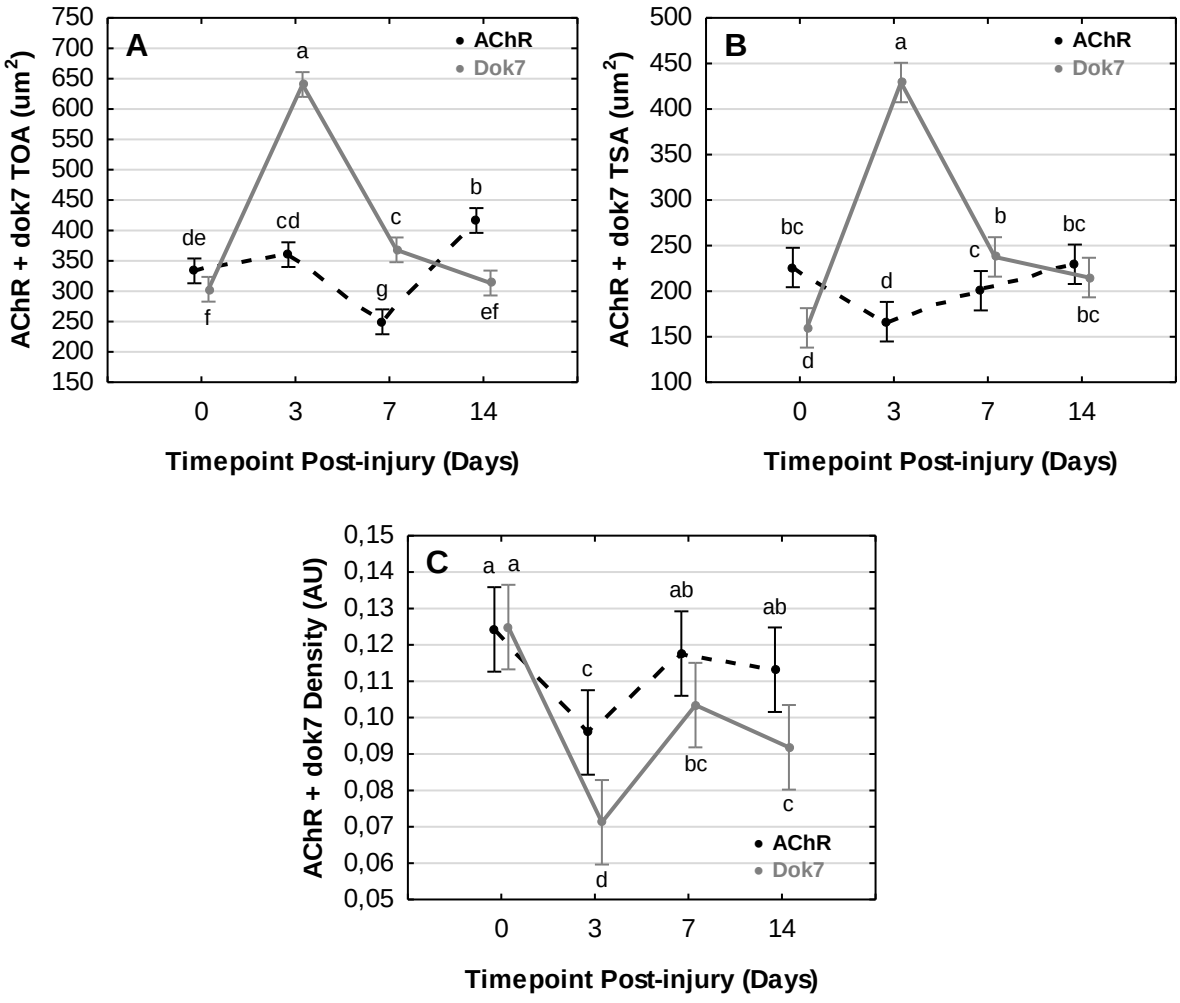

Figure 3.5.12 Quantitative measurements for Dok7 from IHC images pre- and post-injury. Image analyses for AChR and Dok7 carried out on samples from animals sacrificed at D0, and at D3; 7 and 14 post-injury. Data expressed as mean ± 0.95 confidence intervals. Statistical analyses included a Fixed Effect and LSD Test, and $P < 0.01$ was reported as significant. Lower case letters indicate significance between points that are labelled with differing letters. Points that denoted the same lower case letters were not significantly different from one another. A: Total Outlined Area. B: Total Stained Area. C: Staining Density (TSA/SI).

Table 3.1 Mander's Overlap Co-efficient values for AChR and associated synaptic proteins pre- and post-injury.

Injury Timepoint	D0		D3		D7		D14	
Co-efficient	**MOC1**	**MOC2**	**MOC1**	**MOC2**	**MOC1**	**MOC2**	**MOC1**	**MOC2**
AChR + Rapsyn	0.9734	0.9589	0.9675	0.5648	0.7768	0.8159	0.8716	0.9354
AChR + MuSK	0.9082	0.7442	0.6865	0.0431	0.9841	0.5640	0.9400	0.7680
AChR + LRP4	0.9701	0.9764	0.6923	0.7166	0.9862	0.7871	0.9590	0.8137
AChR + Dok7	0.9790	0.9730	0.8741	0.3530	0.8147	0.6927	0.9183	0.7740

The final quantitative methods used to evaluate the relationships between the AChR morphology and the other sub-synaptic proteins' morphology were the Pearson's correlation co-efficient (PCC) and the Mander's overlap co-efficient (MOC) that quantify co-localisation of fluorophores. Data summary is presented above in Table 3.1. Co-occurrence is expressed as MOC1 or MOC2. MOC1 is the fraction of the area of AChR signal that overlaps with the other sub-synaptic proteins' signals and MOC2 is the fraction of the area of the other sub-synaptic proteins' signals that overlap with AChR positive signal.

The co-occurrence and correlation data for AChR and rapsyn signal solidified earlier results (see Figures 3.5.1 A; 3.5.9 A and B) indicating a strong co-localisation between the two components under normal conditions (see Figure 3.5.13). MOC1 and MOC2 values at D0 showed an almost complete overlap in signal expression (see Table 3.1) and the P value also indicated a very strong correlation between the AChR and rapsyn signal intensity (see Figure 3.5.13 C). D3 saw the AChR maintain an overlap with rapsyn signal, however rapsyn signal saw a marked decrease in its overlap with the AChR (see Table 3.1) as a result of its increased TOA and TSA (see Figures 3.5.9 A and B).

Subsequent recovery in rapsyn TOA at D7 (see Figure 3.5.9 A) could be responsible for the MOC2 rising and increasing its concurrent signal with the AChR (see Table 3.1 and Figure 3.5.13 B); while the AChR TOA was at its lowest at D7 (see Figure 3.5.9 A), negatively influencing its MOC1 (see Table 3.1 and Figure 3.5.13 A). By D14, rapsyn had regained its substantial overlap with the AChR as MOC2 returned to the control value (see Table 3.1 and Figure 3.5.13 B). MOC1 also increased but did not fully return to its control value (see Table 3.1 and Figure 3.5.13 A). Interestingly, the correlation data followed a similar trend to the MOC2 data. The greatest decrease in correlation between the AChR and rapsyn was seen between D0 and D3, followed by a gradual increase at D7 and D14 (see Figure 3.5.13 C). However, along with the MOC1 data, the P value did not fully return to its control value at D14 (see Figures 3.5.13 A and C).

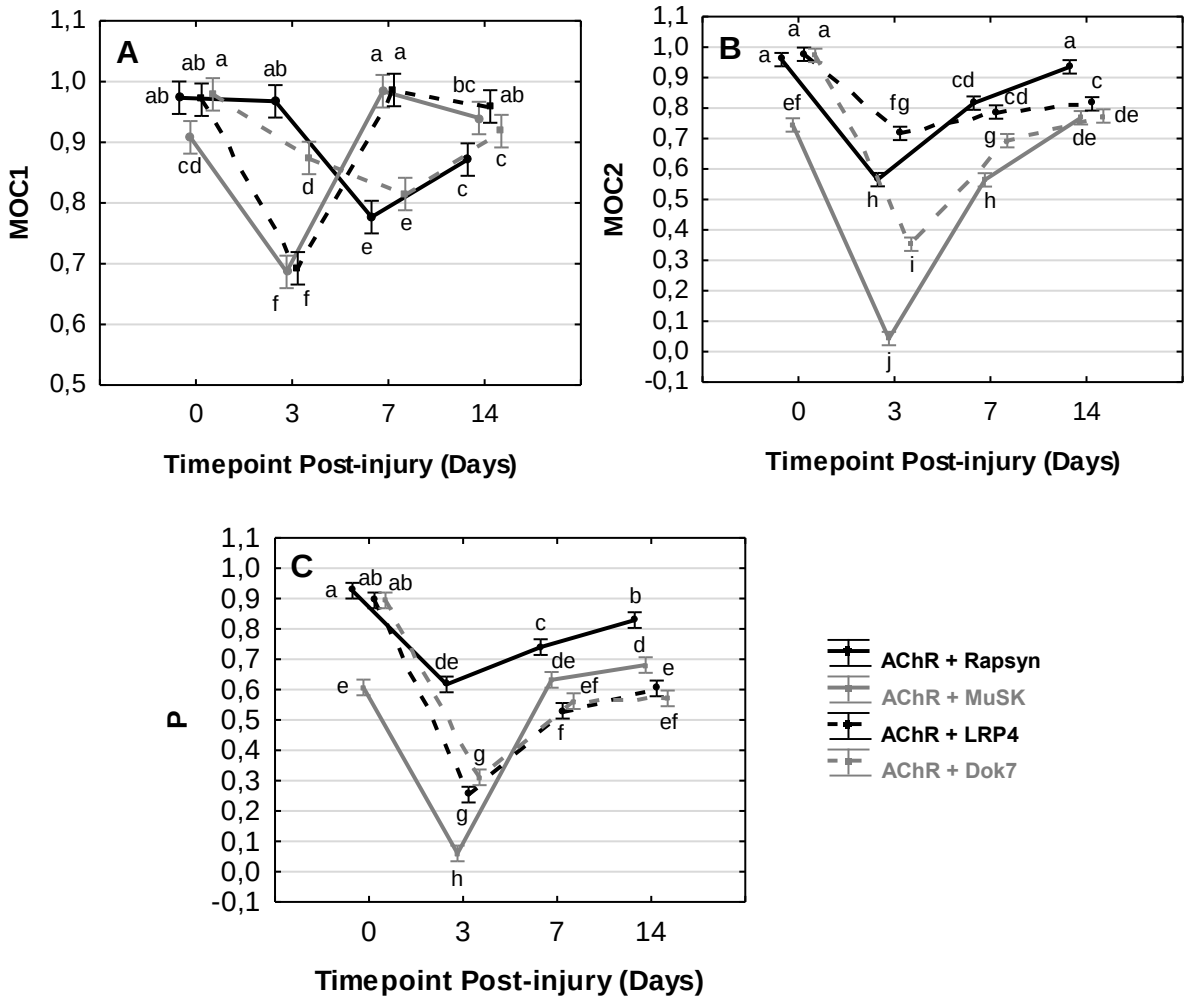

Figure 3.5.13 Co-localisation variable measurements for AChR and its associated synaptic proteins from IHC images pre- and post-injury. Co-localisation tests run on images acquired from samples from animals sacrificed at D0, and at D3; 7 and 14 post-injury. Data expressed as mean ± 0.95 confidence intervals. Statistical analyses included a Fixed Effect and LSD Test, and $P < 0.01$ was reported as significant. Lower case letters indicate significance between points that are labelled with differing letters. Points that denoted the same lower case letters were not significantly different from one another. A: Mander's Overlap Co-efficient 1. B: Mander's Overlap Co-efficient 2. C: Pearson's Correlation Co-efficient.

The co-occurrence and correlation data for AChR and MuSK displayed visibly different profiles to that of the other synaptic proteins. Correlation between AChR and MuSK signal was far lower than its respective counterparts at D0 (see Figure 3.5.13 C). Both MOC1 and MOC2 of the AChR and MuSK were significantly lower when compared to the values of the other sub-groups at D0 (see Table 3.1). As expected, all three variables experienced a sharp decline at D3 (see Figure 3.5.13). Likely as a result of the spike seen in MuSK TOA and TSA, and subsequent marked difference in TOA and TSA between the AChR and MuSK at D3 (see Figures 3.5.10 A and B).

At D7, MOC1 increased beyond its D0 value before returning at D14 (see Figure 3.5.13 A). MOC2 on the other hand, increased at both D7 and D14, but only rebounded to its control value by D14 (see Figure 3.5.13 B). The P value saw an increase to its control value at D7 and then a further increase above control at D14 (see Figure 3.5.13 C).

The AChR and LRP4 MOC1 data displayed a very similar pattern to the AChR and MuSK MOC1 data (see Figure 3.5.13 A). The MOC1 again saw a sharp decline from D0 to D3, followed by an increase back to the control value at D7 (see Table 3.1). There was a slight decrease from D7 to D14, however the MOC1 value at D14 was not significantly different from that of the control value at D0 (see Figure 3.5.13 A). The MOC2 values behaved quite differently when compared to its MOC1 counterparts.

MOC2 data also displayed a significant, but not as severe, decline from D0 to D3 was seen (see Table 3.1). D7 and D14 showed a gradual increase that did not fully recover to the D0 value (see Figure 3.5.13 B). Both the TOA and TSA of AChR and LRP4 at D14 were significantly different from each other, and the TOA and TSA of LRP4 at D14 was significantly different from its control values (see Figures 3.5.11 A and B). Correlation data behaved as one would expect, with a sharp decline in the P value from D0 to D3 following injury (see Figure 3.5.13 C). A steady increase at D7 and D14 was observed, however it was not yet restored to the control value by D14 (see Figure 3.5.13 C).

The MOC1 data of AChR and Dok7 was more closely related to the AChR and rapsyn MOC1 values than the trends of the other proteins. Although a decrease from D0 to D3 was seen, the MOC1 of AChR and Dok7 was at its lowest value at D7 (see Table 3.1). It increased from D7 to D14 but was still significantly lower than the D0 value (see Figure 3.5.13 A). The MOC2 data of the AChR and Dok7 followed a similar trend to that of the other synaptic proteins, with its D0 value the closest to 1 of all the sub-groups (see Table 3.1). A massive drop was seen at D3 after injury (see Figure 3.5.13 B), likely attributed to the spike in Dok7 TSA and dip in AChR TSA at D3 (see Figure 3.5.12 B). A large increase in MOC2 at D7, with a smaller increase at D14 were observed, however it remained significantly lower than the D0 value (see Figure 3.5.13 B).

The correlation data followed an almost identical pattern to that of the LRP4 correlation data. Again, a sharp decline in the P value from D0 to D3 was seen, followed by steady increase at D7 and D14 (see Figure 3.5.13 C). Although D14 was significantly increased from D7, it remained lower than the control value (see Figure 3.5.13 C).

CHAPTER 4: DISCUSSION

4.1 Introduction

This study aimed to investigate and better understand the relationships between the various post-synaptic apparatus at the NMJ of adult skeletal muscle tissue before and after injury. This was achieved by employing both qualitative and quantitative methods to examine the synapse function and structure under normal conditions in healthy skeletal muscle, and on different days in post-injured muscle tissue.

A more nuanced grasp of the functions of and the dynamic interactions between these specialised components is of particular importance due to their role in a myriad of myopathies that require relatively constant regeneration. There is also less known about the repair process of the NMJ compared to the contractile proteins in response to injury.

The main aims of the research and the findings presented in the previous chapter, that will be discussed here, are as follows:

Firstly, immunohistochemical and histological analyses showed that the ultrastructure of the muscle fibres along with the synapse underwent severe morphological destruction following the muscle crush injury.
Secondly, by following the time course of structural changes in conjunction with functional deterioration and subsequent improvement, this study was able to establish that a return of muscle function was preceded by structural adaptations in response to injury.
Thirdly, the main novelty of the research and results are those that address the close association between AChR-associated proteins at the post-synaptic membrane and the receptor itself; associations that could be quantified.
Finally, the relationship between the recovery of these associations and the recovery of normal function was addressed.

“You should write not what you know but what you can find out about.” – (Sawyer, 2017).

4.2 Post-synaptic proteins associate with the AChR in healthy adult skeletal muscle tissue

The first objective of this study (see Section 1.4) was to qualitatively evaluate the cellular morphology of the myofibre and the ultrastructure of the post-synaptic NMJ apparatus in healthy skeletal muscle tissue. Section 3.2.1 describes the muscle fibre morphology of the *gastrocnemius* of a healthy adult BALB/C mouse in both longitudinal and cross-sections. Published literature that made use of longitudinal orientation as opposed to cross-sections in skeletal muscle tissue is limited due to the difficulty associated with avoiding artefacts while processing the samples (Ekundina & Eze, 2015) (Pearson & Sabarra, 1974). In the current study, the usual markers of normal muscle tissue were observed with no disruptions to the fibres in both orientations (Young, *et al.*, 2013). This confirmed that the mice used were healthy and had no underlying pathologies that affected their skeletal muscle and that the tissue processing was effective.

As expected in longitudinal sections, peripheral fibres were orientated in mixed directions, with some diagonal and cross-sections present. This was due to the fusiform arrangement of the *gastrocnemius* fibres within each of the heads (Dave, *et al.*, 2012). The bulging shape of the medial and lateral heads are responsible for the distal portion of the fibres being in a mixed orientation (see figure 4.1). The importance of the longitudinal orientation within the context of the IHC was because of the positioning of the AChRs in relation to the muscle fibres. Only the images from the longitudinal sections that met the selection criteria were included in the quantitative image analysis: the AChRs needed to be viewed *en face* so that their complete 2D structure could be assessed.

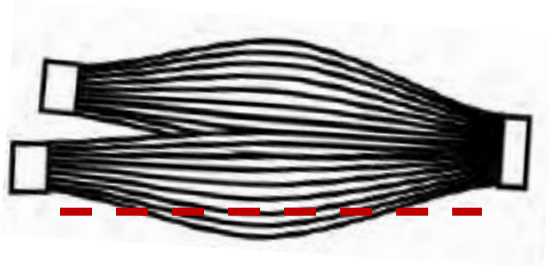

Figure 4.1 Fusiform arrangement of medial and lateral head of the *gastrocnemius.* Red dashed line indicates path of longitudinal section through the muscle belly.

The pretzel-like architecture of the AChR has been well described in the literature and its normal structure in healthy skeletal muscle tissue has been well established (Gervasio & Phillips, 2005) (Mori, et al., 2017) (Punga & Reugg, 2012) (Pratt, et al., 2013) (Shi, et al., 2012). The relationship between the AChR and its associated pre-synaptic components has also been frequently investigated.

As discussed in Section 1.2.3, optimal neural transmission relies on an effective overlap of the pre-synaptic nerve terminals and ACh-filled vesicles with the post-synaptic AChR (Mori, et al., 2017). However, the continuation of the nerve signal to the muscle side of the NMJ and then along the sarcolemma is dependent on appropriate functionality of the AChR complex. To ensure dynamic maintenance of the AChR, its post-synaptic associated proteins are constantly in interaction with the receptor and each other (Lee, et al., 2009).

Research focussing on the interactions between the AChR and the post-synaptic proteins is far less prevalent when compared to its pre-synaptic counterparts, especially with regards to LRP4 and Dok7. MuSK and rapsyn have enjoyed slightly more popularity in literature. With neuromuscular disease or injury, there is limited plasticity retained by the mature NMJ to enable a return to normal function, hence the need for a variety of injury models to be explored (Magill, 2009).

Most of the NMJ post-injury regeneration research has been done using eccentric contraction damage (Pratt, et al., 2013), however there are virtually no studies that track the post-synaptic changes at the NMJ following a mechanical PNI. Therefore, the current study produced novel data on the effects of a non-invasive PNI on the post-synaptic structure and function of the NMJ. The AChRs were labelled with α-Btx, and stained in conjunction with an associated protein of interest, namely rapsyn, MuSK, LRP4 or Dok7. In order to better understand the regenerative response to exogenous disruptions (traumatic injury), one must for comparison's sake first understand the associations between each of these proteins and the AChRs in healthy muscle.

Relevant literature consulted regarding immunohistochemical staining of the AChR in combination with the post-synaptic proteins of interest appears to have only achieved successful staining results in muscle tissue cross-sections, as opposed to ideally longitudinal sections. There are a number of challenges associated with immunostaining of these post-synaptic proteins, most notably a lack of effective primary antibodies. This, coupled with the previously described difficulties related to acquiring quality longitudinal sections, has resulted in a lack of published data displaying *in vivo* co-staining of the AChR and its associated proteins *en face* in the longitudinal orientation. Hence, the results achieved in this study provide novel insight into the distribution of the AChR and its post-synaptic proteins *in vivo*.

In brief, in the healthy skeletal muscle tissue clear similarities were seen between the staining profiles of the AChR and specifically rapsyn, MuSK and LRP4. This was true for muscle sections in both the longitudinal and cross-sectional orientations (see Figures 3.5.1 – 3.5.6). AChR and Dok7 signal did not appear to co-localise in the same manner as the other post-synaptic proteins, however the distribution of Dok7 was not random in relation to the AChRs in the un-injured tissue.

As previously mentioned, the widely accepted blueprint for the arrangement of the components of the post-synaptic membrane has never fully been substantiated in research. And while these diagrams have suggested a clear link between the AChR and rapsyn, and the AChR and MuSK, no direct interaction between the AChR and both LRP4 and Dok7 has been described (Punga & Reugg, 2012). Therefore, in the current research, qualitative imaging was backed up by quantitative analyses of the fluorescent images. These were able to determine that in healthy skeletal muscle tissue, both rapsyn and MuSK occupied comparable TSA and TOA when compared to their corresponding AChR (see Figure 5.9 A and B, and Figure 5.10 A and B).

LRP4 and its corresponding AChR covered similar TOA, however the TSA of LRP4 was slightly lower than that of the AChR see Figure 5.11 A and B. This implies that although the LRP4 shape is similar to the AChR, it was more dispersed within its location. In the case of Dok7 and its corresponding AChR, although not far off from each other, the TOA and TSA values of the Dok7 are both lower than that of the AChR (see Figure 5.12 A and B), but their staining density values were the same. This implies that the Dok7 signal occupied a smaller area when compared to the AChR, but still had relatively similar intensity distribution patterns. The TSA and TOA values of the respective components give an idea of their relative size under normal conditions.

In addition to the general shape and quantity/density of each protein relative to the AChRs, co-localisation was also assessed to discern the nature of the interactions between the AChR and each of the associated post-synaptic proteins. There are generally two categories of methods used to quantify co-localisation, namely co-occurrence and correlation. As briefly mentioned in Section 2.4.4.4, co-occurrence analyses the positive signal of a respective channel that overlaps in pixels with another channel of interest and is calculated using the Mander's Overlap Co-efficient method (Adler & Parmryd, 2010). In contrast, correlation takes into consideration positive signal pixels as well as signal intensities and is calculated using the Pearson's Correlation Co-efficient method (Lagache, et al., 2015).

According to Table 3.1 and figure 3.5.13, at D0 the MOC1 and MOC2 values for all four proteins in combination with the AChR (with the exception of the MuSK MOC2) were extremely close to 1. This indicates that a considerable percentage of the AChR pixels overlap with pixels of the corresponding protein of interest, as well as vice versa. In the case of the MuSK co-localisation, it had the lowest MOC1 and MOC2 values. Most notable was the MOC2 value of 0.7442 (see Table 3.1). While there was still 74% of the MuSK-positive pixels that overlapped with the AChR pixels, it was lower than expected and suggested the potential for the presence of MuSK outside the confines of the AChR. The P values followed a similar pattern in suggesting a strong correlation between the AChR and signal of rapsyn, LRP4 and Dok7 (see Figure 3.5.13 C). The lower P value of MuSK could be attributed to the differences in intensities coupled with its relatively low MOC2 value.

4.3 Mass drop induces severe contusion injury in the skeletal muscle tissue

4.3.1 Muscle force generation is impaired following muscle crush injury

The force-frequency relation (FFR) is the relationship between the electrical stimulation frequencies used to activate the muscle and the isometric force generated by the muscle that is activated (Scott, et al., 2006). This relationship usually takes a sigmoidal shape to form a force-frequency curve (Lee, et al., 2009). Force generated by the plantar flexor muscles (*gastrocnemius, soleus and plantaris*) of the mice was measured using a force-frequency protocol as described in Section 2.2.1. A baseline reading was established before injury to assess the effect of the contusion injury on muscle function. A preliminary experiment also assured that the force testing protocol itself did not elicit any changes in subsequent readings (see Figure 3.3.1). This was to ensure that any differences seen in results were purely as a result of the injury.

Figure 3.3.2 shows the results of the force-frequency protocol plotted as Force/Body Mass to ensure the data was comparable across mice of difference sizes. All three time points showed a considerable decrease in force production at certain frequencies. The specific range of 60 Hz to 90 Hz saw a significant decline ($P < 0.0001$) in force production at all three time points when compared to their respective baseline values.

The sigmoidal curve can be described as having a rightward shift in response to the contusion injury (Scott, et al., 2006). The post-injury readings required higher stimulation frequencies to produce the same relative force when compared to the baseline readings (Gerrits, et al., 1999) (Rochester, et al., 1995). The D7 and D14 groups appear to begin to make a return to recovery of function at 120 Hz stimulation. This suggests that structural regeneration may be underway by D7 already to repair the neural pathway to the muscle tissue or the receiving complex on the muscular side of the NMJ, or both.

The cumulative data (AUC for force) presented in Figure 3.3.4 reinforces that full recovery suggested in response to the 120 Hz stimulation at D7 and D14 is still only partial. Therefore, when considering both sub-maximal activation and maximal activation the force response as a whole, the AUC results show that there is still a significant decrease ($P < 0.0001$) in the force generated between baseline and post-injury at D7 and D14.

4.3.2 Muscle fibre and synapse disruption

The second objective of this study (see Section 1.4) was to assess the effects of an induced contusion injury on the muscle fibre and post-synaptic morphology. Section 3.2.2 details the response to injury in the muscle tissue with notable markers identified. Disrupted fibres, immune cell infiltration, oedema and necrotic tissue were all exhibited following the muscle crush injury (see Figure 3.2.3 and 3.2.4) and confirmed that the induced contusion caused extensive structural damage to the muscle tissue. It appeared as though cellular regeneration was initiated by D7 and continued throughout D14, with the presence of centralised nuclei. Central nuclei are recognised as markers of myofibre repair in progress (Folker & Baylies, 2013).

Central nuclei are also a hallmark sign of several muscle diseases collectively named Central Nuclear Myopathies (CNM). In many of these cases the centralised nuclei are due to a loss of their normal position due to proteins not expressed properly, although some of the nuclei may be central responding to the muscle's attempt to regenerate. Less than 3% of myofibres are expected to have centralised nuclei in healthy skeletal muscle tissue, as opposed to approximately 25% in CNM skeletal muscle tissue (Spiro, et al., 1966).

Central nuclei have been implicated in muscle development and regeneration both when the usually peripheral myonuclei revert away from the sub-sarcolemmal position and when mono-nucleated myoblasts fuse to form multi-nucleated myotubes (Folker & Baylies, 2013). The nuclei migrate centrally and eventually form a mature myofibre with peripheral nuclei (Cadot, et al., 2012).

Once distinct regions of damage were identified using H&E staining (see Figure 3.2.1 to 3.2.8), serial sections were prepared and IHC staining was carried out. AChRs stained in conjunction with the post-synaptic proteins of interest revealed images that depicted the effect of the injury on the NMJ specifically.

Upon quantification, the general trend that the signal profiles of all the auxiliary post-synaptic proteins appeared to follow, was a spike in TSA and TOA in response to injury. This translates to widespread dispersion, as opposed to the initial condensed positive signal that aligns with that of the AChR. For the AChR itself, the TSA and TOA generally either remained the same or decreased across the sub-groups and time points following injury, implying a collapse of structure rather than dispersion.

Rapsyn in particular underwent extreme deviation from the course of response of its corresponding AChR. Rapsyn TSA and TOA increased by approximately 50% from D0 to D3 while the AChR TSA and TOA decreased by 50% (see Figure 3.5.9). While rapsyn may be the most closely associated post-synaptic protein to the receptor itself, there is a distinct difference in their structure as the AChR is a transmembrane molecule, while rapsyn is intracellular (Ramarao, et al., 2001). These differences in their structure and location could be responsible for their vastly opposed responses to injury. While a return towards normal structure began at D7, the TOA of rapsyn and both the TSA and TOA of the AChR remained lower than their baseline values (see Figure 3.5.9). One can therefore assume that the repair process was not yet concluded by D14.

Quantitative results of the other three auxiliary proteins confirmed what the qualitative results suggested with MuSK, LRP4 and Dok7 all showing extensive increases in their TSA and TOA in response to the induced contusion injury (see Figure 3.5.10 – 3.5.12). MuSK and Dok7 distribution patterns followed each other closely with the initial spike at D3 signifying severe dispersion of their signal with a subsequent drop towards baseline at D7 (see Figure 3.5.10 and 3.5.12).

This was interesting to note as MuSK and Dok7 share a similar interaction with each other to that of the AChR and rapsyn, where the former is a transmembrane protein and the latter an intracellular protein. Despite comparable associations between the two pairs, MuSK and Dok7 followed the same reaction as opposed to AChR and rapsyn having contrasting responses. This may suggest that the anchoring role Dok7 performs for MuSK functions differently to that of the role rapsyn performs for the AChR. Alternatively, AChR are more tightly embedded in the membrane due to the pentamer structure.

When compared to the other post-synaptic proteins, LRP4 had the most unique response to injury. Although the LRP4 TSA and TOA also spiked just following the contusion injury, they only reached the peak increase at D7 in contrast to the other proteins which reached it at D3 (see Figure 3.5.11). This delayed reaction to the injury also caused the D14 TSA and TOA to not fully return to the respective baseline values. When consulting the qualitative images, LRP4 retained a substantial portion of signal in the site of the receptor at D3 post-injury (see figure 3.5.5 panel B). However, by D7, the LRP4 signal is far more dispersed than before (see figure 3.5.5 panel C).

The time course that this transmembrane protein followed in response to injury is peculiar when compared to that of MuSK, the other transmembrane protein. There is however no reported direct interaction between LRP4 and the AChR which may influence its resultant response in comparison to the response of MuSK.

Blood plasma analysis also provided interesting insight as to systemic clearance/circulation of MuSK following traumatic injury. ELISA results showed that there was a 4-fold increase in the plasma MuSK concentration in response to the muscle crush injury at D3. Although there was no significant difference between D3 and D7, plasma MuSK reached its peak concentration at D14 with a 5-fold increase from the D0 concentration.

While one would not expect plasma MuSK concentrations to peak so late after injury when considering that the NMJ morphology had already showed signs of regeneration by D7, it is important to consider the source of the plasma MuSK and how it made its way to the vasculature. ELISA results alone would not be able to determine the source of the plasma MuSK, however it could be hypothesised that the MuSK could either be displaced from the original site of injury or newly synthesised.

Displaced MuSK could be caused by a leakage of cell contents, and specifically membrane-bound proteins, in response to the muscle crush injury. Sarcolemmal damage is caused by mechanical disruptions to the muscle fibre membrane and is characterised by an increase in plasma membrane permeability (Alloush, et al., 2013)(Celes, et al., 2010). Extracellular debris is disposed of by macrophages during the inflammatory response that follows injury, however the presence of MuSK in the plasma suggests that clearance of the degraded synaptic proteins may also be facilitated by vascular removal.

Alternatively, MuSK synthesis in response to injury may be responsible for flooding the synaptic region with excess amounts of newly synthesised MuSK protein. Should membrane sealing not be fully completed, the muscle fibre may undergo further leakage of excess MuSK into the extracellular space after the process of protein synthesis has already begun. This postponed increase in MuSK plasma concentration could account for the delayed peak at only D14.

While neither of these hypotheses could be determined from the protocols carried out, they present an intriguing follow up question to the results acquired. Further understanding of the response to injury should include additional direct quantitative measures such as qPCR and ELISA analyses of the AChR and all the synaptic auxiliary proteins. A comparison in protein concentration between the muscle tissue and the blood plasma may also be useful in comprehending the mechanisms of action of the synaptic components and the timeframe that they follow.

4.3.3 Correlation and co-occurrence of AChR-associated proteins

Whilst the TOA and TSA provided individual results for each protein assessed and inferences of different responses to injury could be made, direct comparisons were also done. Calculating the MOC1 and MOC2 for each protein sub-group provided interesting insight into the difference in response between the AChR and its respective corresponding post-synaptic protein.

The two co-occurrence variables were able to quantitatively distinguish the progress of the signal patterns in response to traumatic injury. Taking into consideration the opposing dispersion and compression reactions (see Section 4.3.2), the co-occurrence of the AChR and its associated protein were not expected to follow the same pattern.

The MOC1 responses of MuSK and LRP4 were closely related as both dropped significantly (25% - 27% decrease) from D0 to D3 (see Figure 3.5.13 panel A). Both values peaked at D7, even surpassing their respective baseline readings, followed by a tapered decline to their D0 values. These data indicate that the injury caused the AChR and MuSK/LRP4 to partially dissociate, as less than 70% of the AChR overlapped with signal from the corresponding protein (see Table 3.1). However, by D7 compensatory mechanisms came into play with a 98% overlap of AChR signal with its associated protein.

The MOC1 responses of Dok7 and rapsyn were both markedly different to that of MuSK and LRP4. Although the MOC1 of both rapsyn and Dok7 decreased in response to injury at D3, their values were only at their lowest by D7 and the decline from baseline was less severe (16% - 20% decrease) when compared to MuSK and LRP4 (see Figure 3.5.13 panel A). This translated to rapsyn and Dok7 retaining more signal at the site of the AChR than did MuSK and LRP4 (see Figures 3.5.1 to 3.5.8). This could be explained, only in part, by the close associated between AChR and the anchoring role of rapsyn.

As expected, the MOC1 and corresponding MOC2 values did not follow the same trends (see Figure 3.5.13). All four MOC2 values of the protein sub-groups decreased significantly to their lowest values at D3, however the extent of the decrease varied substantially (26% - 95% decrease) between the proteins (see Table 3.1). The MOC2 of MuSK and Dok7 had the harshest response to injury which could be explained by the extensive dispersion of their signal even if there was still some signal that remained close to the AChR (MOC1). Nonetheless, the AChR retained minimal overlap with the protein signal.

Because the TOA and TSA of MuSK and Dok7 were substantially larger than that of their corresponding AChR TOA and TSA (see Figures 3.5.10 and 3.5.12), the MOC2 values were affected disproportionately in comparison to the MOC1 values (see Figure 3.5.13). This is because the MOC1 reflects the fraction of the AChR TSA that overlaps with the respective auxiliary protein, while MOC2 indicates the fraction of auxiliary protein TSA that overlaps with the AChR (see Section 2.4.4.4).

Rapsyn and LRP4 both had a milder response to injury when compared to their counterparts. LRP4 had the smallest decline from baseline (26% decrease), but along with Dok7 did not fully return to its respective D0 value by D14. This indicates that Dok7 and LRP4 remained relatively dispersed from the site of the AChR by D14 (see Figures 3.5.5 to 3.5.8) and one could speculate that their relocalisation depends on the other proteins relocalising first. In contrast, MuSK overcame severe dispersion to regain substantial overlap of MuSK with the AChR (see Figure 2.5.3). Rapsyn also returned to a closely matched signal profile with its corresponding AChR, with 94% of the rapsyn signal overlapping with the AChR signal (see Table 3.1).

Due to the difference in co-occurrence and correlation, the MOCs and PCCs can be difficult to interpret when understanding co-localisation. While the MOC provides a simplistic description of the spatial overlap of positively stained pixels of two different channels, the PCC further takes signal intensities into consideration and their ability to co-distribute in proportion to one another (Dunn, et al., 2011). The degree to which the variability in the protein of interest's pixel intensity and the AChR pixel intensity overlap can be expressed as a linear function and is quantified by the PCC and expressed as P values (Adler & Parmryd, 2010).

Rapsyn, LRP4 and Dok7 produced P values exceptionally close to 1, indicating strong signal correlation between the protein and the receptor in terms of location and intensity in healthy muscle (see Figure 3.5.13 panel C). The P values of all four proteins responded similarly to the MOC2 values, as they decreased to their lowest value at D3 as a result of a substantial disassociation between the proteins and AChRs. While stand-alone moderate P values are usually complicated to interpret, they are far more relevant when compared to the more extreme P values (Dunn, et al., 2011). Hence, the readings at D3 confirm the considerable effect that the contusion injury has on the NMJ.

Interesting to note was that the proteins that had P values exceptionally close to 1 at baseline (rapsyn, LRP4 and Dok7) did not fully recover their correlative association to the receptors by D14 (see Figure 3.5.13 panel C). In contrast, MuSK hade a moderate P value at baseline, but reached its peak at D14 post-injury. This suggests that in the case of MuSK, regenerative mechanisms could cause an increase in the signal correlation between MuSK and the AChR above normal levels in response to injury.

4.4 Relevance of injury models in muscle research

Section 1.3 reviewed a number of experimental models that induce an injury to the skeletal muscle tissue and the NMJ. These injury models can be particularly useful in addressing the need for a better understanding of NMJ-specific myopathies. The majority of these myopathies are currently incurable with minimal treatment strategies available to patients.

Amyotrophic lateral sclerosis (ALS) is an example of a neurodegenerative disorder defined by pathophysiological events that result in the denervation and subsequent degeneration of the NMJ (Arbour, et al., 2015). In contrast, congenital myasthenic syndromes (CMS) refers to a group of diseases where the root of the pathology is specific to synaptic defects by means of gene mutations. These inherited gene mutations can affect any of the relevant synaptic components including, but not limited to the AChR, rapsyn, LRP4, MuSK and Dok7 (Muller, et al., 2007). As a result, neural transmission is impaired and can cause considerable muscle weakness, fatigue and in severe cases, degeneration (Cossins, et al., 2006). Current studies are therefore targeting these molecules of interest in an attempt to produce potential therapeutic strategies (Arimura, et al., 2014).

One of the most notable neuromuscular disorders is myasthenia gravis (MG), an autoimmune disease that targets the AChR and its associated post-synaptic proteins. In cases of MG, the body produces antibodies that block the action of the NMJ components that become unable to respond to the motor nerve. It is estimated that around 85% of patients that suffer from MG have anti-AChR antibodies present in their sera (Nikolica, et al., 2016). Those who present with AChR-antibody negative sera usually produce MuSK-antibody or LRP4-antibody positive sera (Nikolica, et al., 2016)(Punga, et al., 2011). MuSK or the presence of the MuSK-antibody should not be expected in the sera of healthy individuals, hence the importance of Section 3.4.

Even though the mature NMJ of skeletal muscle tissue maintains a relatively high level of plasticity into adulthood, its regenerative capacity is still somewhat limited (Magill, 2009). As a result, incomplete recovery can potentially occur following traumatic injuries, leaving patients with impaired muscle function that may never be restored. This is why numerous injury models have been used in studies to explore what mechanisms might also be disrupted in pathological states. Knockout animals, aged populations and induced injuries have all generated synaptic environments comparable to that of NMJ-specific myopathies (Alvites, et al., 2018).

4.5 Conclusion, limitations and recommendations

The objectives outlined in this study were successfully achieved as the morphology of the skeletal muscle tissue and the post-synaptic NMJ, along with the functional capacity of the muscle were definitively established under normal conditions in healthy adult mice. The variables were further assessed following an induced contusion injury to the muscle and indicated that muscle structure and function were considerably impaired in response to injury. However, regenerative mechanisms were initiated within the time frame of the experiments as certain variables began to recover towards their baseline values.

Although not fully comprehensive, these findings present appropriately quantified data into the interactions between the post-synaptic apparatus components and their responses to injury. To my knowledge, this study is the first to produce IHC images depicting the AChR *in combination* with rapsyn, MuSK, LRP4 and Dok7 in both un-injured and injured skeletal muscle tissue and particularly to follow the qualitative imaging with quantitation. The addition of the muscle force testing data also provides a novel aspect that further strengthens the results as they address both the structural and functional modifications that follow injury.

This thesis does have a few limitations. One challenge when assessing multiple proteins using IHC is that the primary antibodies available were limited with respect to the species specificity. As a result, certain secondary antibody combinations were affected, but with extensive troubleshooting it was possible to ensure that there was no overlapping of wavelengths.

In retrospect, there are a number of recommendations that can be made for future studies. It became apparent that the regenerative process was still well underway by the final time point (D14). Therefore an extended time course for the experiment should be implemented to cover a wider range of the repair response. Ideally the experiment should run up to 28 days post-injury with weekly intervals from 7 days post-injury onwards.

Due to ethical constraints, the number of animals used in the experiment was relatively low and subsequently the injury groups consisted of fewer animals than the control group. It was considered very important that complete confidence was developed for control conditions, otherwise the post-injury response could not be considered validly different from baseline. However, due to more variability post-injury, it would be useful in future larger studies to have at least the same number of animals across all time points. For example, at least 12 animals per time point should be used and it would be recommended to determine if, due to higher variability at any particular time point, a larger group size would be statistically useful.

While the ELISA results for plasma MuSK were successful, it would be beneficial to add the other post-synaptic components (in particular the AChR) in further studies. Careful consideration would need to be made regarding the small volume of blood that can be drawn from mice should additional protocols require more plasma.

The data presented in this study provides novel insight into the mechanisms involved in post-synaptic stability, vs. instability in response to injury. While each section of data shown may not be the first of its kind, the results collectively tell a story that has not yet been explored in the world of neuromuscular research. In conclusion, this study successfully conducted a holistic assessment of the NMJ in terms of structural and functional response to an acute trauma.

REFERENCES

Adler, J. & Parmryd, I., 2010. Quantifying Colocalization by Correlation: The Pearson Correlation Coefficient is Superior to the Mander's Overlap Coefficient. *Journal of the International Society for Advancement of Cytometry*, Volume 77, pp. 733-742.

Albuquerque, E., Pereira, E. & Alkondon, M., 2009. Mammalian Nicotinic Acetylcholine Receptors: From Structure to Function.. *Physiology Review*, Volume 89, pp. 73-120.

Algora, J. et al., 1996. Functional effects of lymphotoxin on crushed peripheral nerve.. *Microsurgery*, 17(3), pp. 131-135.

Alluin, O. et al., 2009. Functional recovery after peripheral nerve injury and implantation of a collagen guide.. *Biomaterials*, 30(3), pp. 363-373.

Alvites, R. et al., 2018. Peripheral nerve injury and axonotmesis: State of the art and recent advances. *Cogent Medicine*, Volume 5.

Amenta, A. et al., 2012. Biglycan is an extracellular MuSK binding protein important for synapse stability. *Journal of Neuroscience*, 32(7), pp. 2324-2334.

Ammar, A. et al., 2013. A Mutation Causes MuSK Reduced Sensitivity to Agrin and Congenital Myasthenia. *PLoS ONE*, 8(1).

Anderton, B. et al., 1982. Monoclonal antibodies show that neurofibrillary tangles and neurofilaments share antigenic determinants.. *Nature*, Volume 298, pp. 84-86.

Apel, E. et al., 1997. Rapsyn Is Required for MuSK Signaling and Recruits Synaptic Components to a MuSK-Containing Scaffold. *Neuron*, Volume 18, pp. 623-635.

Apel, P. et al., 2009. How age impairs the response of the neuromuscular junction to nerve transection and repair: An experimental study in rats.. *Journal of Orthopaedic Research*, 27(3), pp. 385-393.

Arber, S., Burden, S. & Harris, A., 2002. Patterning of skeletal muscle.. *Current Opinion in Neurobiology*, 12(1), pp. 100-103.

Arbour, D. et al., 2015. Early and Persistent Abnormal Decoding by Glial Cells at the Neuromuscular Junction in an ALS Model. *The Journal of Neuroscience*, 35(2), pp. 688-706.

Arimura, S. et al., 2014. DOK7 gene therapy benefits mouse models of diseases characterized by defects in the neuromuscular junction.. *Science*, 345(6203), pp. 1505-1508.

Arnon, S., Schechter, R. & Inglesby, T., 2001. Botulinum toxin as a biologicalweapon:medical and public healthmanagement.. *Journal of the American Medical Association*, 285(8), p. 1059–1070.

Arrington, E. & Miller, M., 1995. Skeletal Muscle Injuries. *The Orthopaedic Clinics of North America*, 26(3), pp. 411-22.

Bain, J., Mackinnon, S. & Hunter, D., 1989. Functional evaluation of complete sciatic, peroneal, and posterior tibial nerve lesions in the rat.. *Plastic and Reconstructive Surgery*, 83(1), pp. 129-138.

Balice-Gordon, R. & Lichtman, J., 1994. Long-term synapse loss induced by focal blockade of postsynaptic receptors.. *Nature*, Volume 372, pp. 519-524.

Banker, B., Kelly, S. & Robbins, N., 1983. Neuromuscular transmission and correlative morphology in young and old mice.. *Journal of Physiology,* Volume 339, pp. 355-377.

Barik, A. et al., 2014. LRP4 Is Critical for Neuromuscular Junction Maintenance. *The Journal of Neuroscience,* 42(34), pp. 13892-13905.

Beer, G., Steurer, J. & Meyer, V., 2001. Standardizing nerve crushes with a non-serrated clamp.. *Journal of Reconstructive Microsurgery,* 17(7), pp. 531-534.

Beiner, J. & Jokl, P., 2001. Muscle Contusion Injuries: Current treatment options. *The Journal of the American Academy of Orthopaedic Surgeons,* 9(4), pp. 227-37.

Bezakova, G. & Reugg, M., 2003. New insights into the roles of agrin. *Nature Review of Molecular Cell Biology,* 4(4), pp. 295-308.

Bolliger, M., Zurlindrn, A., Luscher, D. & Sonderegger, P., 2010. Specific proteolytic cleavage of agrin regulates maturation of the neuromuscular junction. *Journal of Cell Science,* 123(22), pp. 3944-3955.

Boyd, J. & Gordon, T., 2001. The neurotrophin receptors, trkB and p75, differentially regulate motor axonal regeneration.. *Journal of Neurobiology,* Volume 49, pp. 314-325.

Brazier, M., 1959. The historical development of neurophysiology.. In: J. Field, ed. *Handbook of Physiology.*. Washington, D.C.: Williams & Wilkins Co., pp. 1-58.

Brockhausen, J. et al., 2008. Neural agrin increases postsynaptic ACh receptor packing by elevating rapsyn protein at the mouse neuromuscular synapse.. *Developmental Neurobiology,* Volume 68, pp. 1153-1169.

Brockhausen, J. et al., 2008. Neural agrin increases postsynaptic ACh receptor packing by elevating rapsyn protein at the mouse neuromuscular synapse.. *Developmental Neurobiology,* Volume 68, pp. 1153-1169.

Brooks, S. & Faulkner, J., 2001. Severity of contraction-induced injury is affected by velocity only during stretches of large strain.. *Journal of Applied Physiology,* 91(2), p. 661–666.

Bruneau, E., Sutter, D., Hume, R. & Akaaboune, M., 2005. Identification of Nicotinic Acetylcholine Receptor Recycling and Its Role in Maintaining Receptor Density at the Neuromuscular Junction In Vivo.. *Journal of Neuroscience,* 25(43), pp. 9949-9959.

Burnett, M. & Zager, E., 2004. Pathophysiology of peripheral nerve injury: A brief review.. *Neurosurgical Focus,* 16(5).

Cadot, B. et al., 2012. Nuclear movement during myotube formation is microtubule and dynein dependent and is regulated by Cdc42, Par6 and Par3.. *EMBO Reports,* Volume 13, p. 741–749.

Campagna, J. & Fallon, J., 2006. Lipid rafts are involved in C95 (4,8) agrin fragment-induced acetylcholine receptor clustering. *Neuroscience,* 138(1), pp. 123-132.

Campbell, W. W., 2008. Evaluation and management of peripheral nerve injury.. *Clinical Neurophysiology,* 119(9), pp. 1951-1965.

Cartaud, J. et al., 1973. Presence of a lattice structure in membrane fragments rich in nicotinic receptor protein from the electric organ of Torpedo marmorata.. *FEBS Lett,* Volume 33, pp. 109-113.

Chang, C. C. & Lee, C. Y., 1963. Isolation of neurotoxins from the venom of Bungarus multicinctus and their modes of neuromuscular blocking action.. *Archives internationales de pharmacodynamie et de thérapie,* Volume 144, pp. 241-257.

Changeux, J.-P., 2012. The Nicotinic Acetylcholine Receptor: The Founding Father of the Pentameric Ligand-gated Ion Channel Superfamily. *The Journal of Biological Chemistry,* 287(48), pp. 40207-40215.

Changeux, J.-P., Kasai, M. & Lee, C.-Y., 1970. Use of a Snake Venom Toxin to Characterize the Cholinergic Receptor Protein. *Proceedings of the National Academy of Sciences of the United States of America,* 67(3), pp. 1241-1247.

Chan, J. et al., 2017. *What happens at the Human Neuromuscular Junction after a Traumatic Nerve Injury? A Temporal Profile of Human Motor Endplate Degradation after Brachial Plexus Injury.* Orlando, PRS Global Open.

Chao, T., Frump, D., Lin, M. & Caiozzo, V., 2013. Matrix Metalloproteinase 3 Deletion Preserves Denervated Motor Endplates after Traumatic Nerve Injury. *Annals of Neurology,* Volume 73, pp. 210-223.

Chen, F., Kuziemko, G. & Stevens, R., 1998. Biophysical characterization of the stability of the 150-kilodalton botulinum toxin, the nontoxic component, and the 900-kilodalton botulinum toxin complex species.. *Infection and Immunity,* 66(6), p. 2420–2425.

Cheng, X. et al., 2015. The longitudinal epineural incision and complete nerve transection method for modeling sciatic nerve injury.. *Neural Regeneration Research,* 10(10), pp. 1663-1668.

Chen, L. et al., 1992. The functional recovery of peripheral nerves following defined acute crush injuries.. *Journal of Orthopaedic Research,* 10(5), pp. 657-664.

Chhabra, A., Ahlawat, S., Belzberg, A. & Andreseik, G., 2014. Peripheral nerve injury grading simplified on MR neurography: As referenced to Seddon and Sunderland classifications.. *The Indian Journal of Radiology & Imaging,* 24(3), p. 217.

Chiu, A. & Sanes, J., 1984. Development of basal lamina in synaptic and extrasynaptic portions of embryonic rat muscle. *Developmental Biology,* 103(2), pp. 456-467.

Choi, E. et al., 2016. Neural ablation and regeneration in pain practice.. *Korean Journal of Pain,* 29(1), pp. 3-11.

Cloud-Clone, 2013. *Enzyme-linked Immunosorbent Assay Kit For Muscle, Skeletal, Receptor Tyrosine Kinase (MUSK) Instruction manual.* 11 ed. Katy, TX: s.n.

Colledge, M. & Froehner, S., 1998. To muster a cluster: Anchoring neurotransmitter receptors at synapses. *Proceedings of the National Academy of Sciences of the USA,* Volume 95, pp. 3341-3343.

Corringer, P.-J. & Changeux, J.-P., 2008. Nicotinic acetylcholine receptors.. *Scholarpedia,* 3(1), p. 3468.

Cossins, J. et al., 2006. Diverse molecular mechanisms involved in AChR deficiency due to rapsyn mutations. *Brain*, Volume 129, pp. 2773-2783.

Dasgupta, B. & Sugiyama, H., 1976. Molecular forms of neurotoxins in proteolytic Clostridium botulinum type B cultures.. *Infection and Immunity*, 14(3), p. 680–686.

Dave, M., Yagain, V. & Anadkat, S., 2012. Unilateral Third/Accessory Head of the. *International Journal of Morphology Gastrocnemius Muscle: a Case Report*, 30(3), pp. 1061-1064.

de Paiva, A. et al., 1999. Functional repair of motor endplates after botulinum neurotoxin type A poisoning: biphasic switch of synaptic activity between nerve sprouts and their parent terminals.. *Proceedings of the National Academy of Sciences of the United Staes of America*, 96(6), p. 3200–3205.

Deane, M., Gregory, M. & Mars, M., 2014. The creation of a measurable contusion injury in skeletal muscle.. *Journal of the South African Veterinary Association*, 85(1), p. 1031.

Deschenes, M., 2011. Motor unit and neuromuscular junction remodelling with aging.. *Current Aging Science*, Volume 4, pp. 209-220.

Deschenes, M., Hurst, T., Ramser, A. & Sherman, E., 2013. Presynaptic to Postsynaptic Relationships of the Neuromuscular Junction are Held Constant Across Age and Muscle Fiber Type.. *Developmental Neurobiology*, pp. 744-753.

Deschenes, M., Roby, M., Eason, M. & Harris, M., 2010. Remodelling of the nerumuscular junction precedes sarcopenia related alterationms in the myofibres.. *Experimental Gerontology*, Volume 45, p. 389–393.

Distefano, G. et al., 2013. Neuromuscular Electrical Stimulation as a Method to Maximize the Beneficial Effects of Muscle Stem Cells Transplanted into Dystrophic Skeletal Muscle. *PLOS ONE*, 8(3).

Doyle, G. T. P., 2008. Tourniquets: a review of current use with proposals for expanded prehospital use.. *Prehospital Emergency Care*, Volume 12, pp. 241-256.

Dressler, D. & Benecke, R., 2003. Autonomic side effects of botulinum toxin type B treatment of cervical dystonia and hyperhidrosis.. *European Neurology*, 49(1), pp. 34-38.

Dunn, K., Kamocka, M. & McDonald, J., 2011. A practical guide to evaluating colocalization in biological microscopy. *American Journal of Physiology Cell Physiology*, 300(4), pp. 723-742.

Ekundina, V. & Eze, G., 2015. Common artifacts and remedies in histopathology. *African Journal of Cellular Pathology*, Volume 4, pp. 6-12.

Eleopra, R. et al., 1998. Different time courses of recovery after poisoning with botulinum neurotoxin serotypes A and E in humans.. *Neuroscience Letters*, 256(3), p. 135–138.

Eston, R. & Reilly, T., 2009. *Kinanthropometry and Exercise Physiology Laboratory Manual*. 3 ed. New York(New York): Routledge.

Evans, W. & Cannon, J., 1991. The metabolic effects of exercise-induced muscle damage.. *Exercise Sport Science Review*, Volume 19, pp. 99-125.

Fahim, M., 1997. Endurance exercise modulates neuromuscular junction of C57BL/6NNia aging mice.. *Journal of Applied Physiology*, Volume 83, pp. 59-66.

Fambrough, D. M., 1979. Control of acetylcholine receptors in skeletal muscle.. *Physiological Reviews*, 59(1), pp. 165-227.

Ferreira, T. & Rasband, W., 2012. *ImageJ*. [Online]
Available at: https://imagej.nih.gov/ij/docs/guide/user-guide.pdf
[Accessed 10 November 2017].

Ferre, J., Mayayo, E. & Brunet, R., 1987. Morphometric study of the neuromuscular synapses in the adult rat with special reference to the remodelling concept.. *Biology of the Cell*, Volume 60, pp. 133-144.

Folker, E. & Baylies, M., 2013. Nuclear positioning in muscle development and disease. *Frontiers in Physiology*, Volume 4, p. 363.

Fortuna, R. et al., 2011. Changes in contractile properties of muscles receiving repeat injections of botulinumtoxin (Botox).. *Journal of Biomechanics*, 44(1), p. 39–44.

Froehner, S. et al., 1981. Immunofluorescence localization at the mammalian neuromuscular junction of the Mr 43,000 protein of Torpedo postsynaptic membrane.. *Proceedings of the National Academy of Science USA*, Volume 78, pp. 5230-5234.

Fuglevand, A., Macefield, V. & Bigland-Ritchie, B., 1999. Force-Frequency and Fatigue Properties of Motor Units in Muscles that Control Digits of the Human Hand. *Journal of Neurophysiology*, 81(1), pp. 1718-1729.

Garcia-Osta, A. et al., 2006. MuSK expressed in the brain mediates cholinergic responses, synaptic plasticity, and memory formation.. *Journal of Neuroscience*, Volume 26, pp. 7919-7932.

Gautam, M. et al., 1996. Defective neuromuscular synaptogenesis in agrin-deficient mutant mice.. *Cell*, Volume 85, pp. 525-535.

Gautam, M. et al., 1995. Failure of postsynaptic specialization to develop at neuromuscular junctions of rapsyn-deficient mice.. *Nature*, Volume 377, pp. 232-236.

Gerrits, H., De Haan, A. & Hopman, M., 1999. Contractile properties of the quadriceps muscle in individuals with spinal cord injury.. *Muscle Nerve*, Volume 22, p. 1249 –1256.

Gervásio, O., Armson, P. & Phillip, s. W., 2007. Developmental increase in the amount of rapsyn per acetylcholine receptor promotes postsynaptic receptor packing and stability.. *Developmental Biology*, 305(1), pp. 262-275.

Gervasio, O. & Phillips, W., 2005. Increased ratio of rapsyn to ACh receptor stabilizes postsynaptic receptors at the mouse neuromuscular synapse.. *Journal of Physiology*, Volume 562, pp. 673-685.

Gibson, W., 2010. *Zero History*. 1st ed. New York: Putnam Adult.

Gillani, S. C. J. S. T. H. D., 2012. The effect of ischemia reperfusion injury on skeletal muscle.. *Injury*, Volume 43, p. 670–675.

Gillespie, S., Balasubramanian, S., Fung, E. & Huganir, R., 1996. Rapsyn Clusters and Activates the Synapse-Specific Receptor Tyrosine Kinase MuSK. *Neuron,* 16(5), pp. 953-962.

Glass, D. et al., 1996. Agrin acts via a MuSK receptor complex.. *Cell,* Volume 85, pp. 513-523.

Goldspink, G., 2012. Age-Related Loss of Muscle Mass and Strength. *Journal of Aging Research,* Volume 158279.

Gomez, A. et al., 2016. Silencing of Dok-7 in Adult Rat Muscle Increases Susceptibility to Passive Transfer Myasthenia Gravis. *The American Journal of Pathology,* 186(10), pp. 2559-2568.

Gonzalez-Freire, M., de Cabo, R., Studenski, S. & Ferrucci, L., 2014. The neuromuscular junction: aging at the crossroad between nerves and muscle. *Frontiers in Aging Neuroscience,* 6(208).

Grady, R. et al., 2005. Syne proteins anchor muscle nuclei at the neuromuscular junction. *PNAS,* 102(12), pp. 4359-4364.

Guo, Q. et al., 2018. Transcriptomic Landscapes of Immune Response and Axonal Regeneration by Integrative Analysis of Molecular Pathways and Interactive Networks Post-sciatic Nerve Transection.. *Frontiers in Neuroscience,* Volume 12.

Hainline, B. W., 2014. Peripheral nerve injury in sports.. *Continuum (Minneap Minn),* 20(6), pp. 1605-1628.

Hamjian, J. & Walker, F., 1994. Serial neurophysiological studies of intramuscular botulinum-A toxin in humans.. *Muscle and Nerve,* 17(12), p. 1385–1392.

Hartmann, R., Carregal-Romero, S., Parak, W. & Rivera-Gil, P., 2012. Investigating Nanoparticle Internalization Patterns by Quantitative Correlation Analysis of Microscopy Imaging Data. In: J. G. V. de la Fuente, ed. *Nanobiotechnology: Inorganic Nanoparticles vs Organic Nanoparticles.* Oxford: Elsevier, pp. 181-196.

Head, S. I. & Arber, M. B., 2013. An active learning mammalian skeletal muscle lab demonstrating contractile and kinetic properties of fast- and slow-twitch muscle. *Advances in Physiology Education,* Volume 37, p. 405–414.

Heckman, C. & Enoka, R., 2012. Motor unit.. *Comprehensive Physiology,* 4(2), pp. 2629-2682.

Hubbard, S. & Gnanasambandan, K., 2013. Structure and activation of MuSK, a receptor tyrosine kinase central to neuromuscular junction formation. *Biochimica et Biophysica Acta,* Volume 1834, pp. 2166-2169.

Ikeda, M. & Oka, Y., 2012. The relationship between nerve conduction velocity and fiber morphology during peripheral nerve regeneration.. *Brain Behaviour,* 2(4), pp. 382-390.

Inaba, K. S. S. R. S. Z. J. W. M. H. T., 2015. Tourniquet use for civilian extremity trauma.. *Journal of Trauma Acute Care Surgery,* Volume 79, p. 232–237.

Inoue, A. et al., 2009. Dok7 activates the muscle receptor kinase MuSK and shapes synapse formation.. *Science Signalling,* 2(59).

Jang, Y. & Van Remmen, H., 2006. Age-associated alterations of the neuromuscular junction.. *Experimental Gerontology,* Volume 46, pp. 193-198.

Johnson, E., Hammer, R. & Herz, J., 2005. Abnormal development of the apical ectodermal ridge and polysyndactyly in Megf7-deficient mice.. *Human Molecular Genetics,* Volume 14, pp. 3523-3538.

Kang, H. et al., 2014. Terminal Schwann Cells Participate in Neuromuscular Synapse Remodeling during Reinnervation following Nerve Injury. *The Journal of Neuroscience,* 34(18), pp. 6323-6333.

Kang, H. et al., 2014. Terminal Schwann Cells Participate in Neuromuscular Synapse Remodeling during Reinnervation following Nerve Injury. *The Journal of Neuroscience,* 34(18), pp. 6323-6333.

Kang, J., Zamorano, D. & Gupta, R., 2011. Limb salvage with major nerve injury: current management and future directions.. *Journal of the American Academy of Orthopaedic Surgery,* Volume 19, pp. S28-S34.

Karczmar, A., 1967. Pharmacologic, toxicologic, and therapeutic properties of anticholinesterase agents.. In: W. Root & F. Hofman, eds. *Physiological Pharmacology.* New York: Academic Press, pp. 163-322.

Karczmar, A., Lindstrom, J. & Christopoulos, A., 2007. History of Research on Nicotinic and Muscarinic Cholinergic Receptors. In: A. Karczmar, ed. *Exploring the Vertebrate Central Cholinergic Nervous System.* Boston: Springer, pp. 151-162.

Kawabuchi, M., Tan, H. & Wang, S., 2011. Age affects reciprocal cellular interactions in neuromuscular synapses following peripheral nerve injury.. *Ageing Research Review,* Volume 10, pp. 43-53.

Kim, N. & Burden, S., 2008. MuSK controls where motor axons grow and form synapses. *Naturak Neuroscience,* 11(1), pp. 19-27.

Ko, C., 2001. International Encyclopedia of the Social & Behavioral Sciences. In: N. Smelser & P. Baltes, eds. *International Encyclopedia of the Social & Behavioral Sciences.* Oxford: Pergamon Press, pp. 10595-10600.

Koman, L., Brashear, A. & Rosenfeld, S., 2001. Botulinum toxin type a neuromuscular blockade in the treatment of equinus foot deformity in cerebral palsy: a multicenter, open-label clinical trial.. *Paediatrics,* Volume 108, p. 1062–1071.

Kragh, J. J. S. K. S. D. M. R. B. L., 2012. Historical review of emergency tourniquet use to stop bleeding.. *American Journal of Surgery,* Volume 203, p. 242–252.

Krarup, C. et al., 2016. Remodeling of motor units after nerve regeneration studied by quantitative electromyography.. *Clinical Neurophysiology,* 127(2), pp. 1675-1682.

Kulakowski, S., Parker, S. & Personius, K., 2011. Reduced TrkB expression results in precocious age-like changes in neuromuscular structure, neurotransmission, and muscle function.. *Journal of Applied Physiology,* Volume 111, pp. 844-852.

Kumar, P., Ferns, M. & Meizel, S., 2006. Identification of agrinSN isoform and MuSK in sperm.. *Biochemical Biophysiological Research,* Volume 342, pp. 522-528.

Kummer, T., Misgeld, T. & Sanes, J., 2006. Assembly of the postsynaptic membrane at the neuromuscular junction: paradigm lost.. *Current Opinion in Neurobiology,* 16(1), pp. 74-82.

Lagache, T., Sauvonnet, N., Danglot, L. & Olivo-Marin, J., 2015. Statistical Analysis of Molecule Colocalization in Bioimaging. *Journal of the International Society for Advancement of Cytometry*, Volume 87A.

Lee, S., Russ, D. & Binder-Macleod, S., 2009. Force Frequency Relation of Skeletal Muscle. In: M. Binder, N. Hirokawa & U. Windhorst, eds. *Encyclopedia of Neuroscience.* Heidelberg: Springer, p. 111.

Lee, Y., Rudell, J. & Ferns, M., 2009. Rapsyn interacts with the muscle acetylcholine receptor via α-helical domains in the α, β, and ε subunit intracellular loops.. *Neuroscience*, 163(1), pp. 222-232.

Lewis, R., 2013. Myasthenia gravis: New therapeutic approaches based on pathophysiology. *Journal of the Neurological Sciences*, 333(1-2), pp. 93-98.

Lindstedt, S., LaStayo, P. & Reich, T., 2001. When active muscles lengthen: properties and consequences of eccentric contractions.. *News in Physiological Sciences*, Volume 16, p. 256–261.

Lindstrom, J., Walter, B. & Einarson, B., 1979. Immunochemical similarities etween subunits of acetylcholine receptors from Torpedo, Electrophorus, and mammalian muscle.. *Biochemistry*, Volume 18, pp. 4470-4480.

Lin, W. et al., 2001. Distinct roles of nerve and muscle in postsynaptic differentiation of the neuromuscular synapse.. *Nature*, Volume 410, pp. 1057-1064.

Lin, W. et al., 2005. Neurotransmitter acetylcholine negatively regulates neuromuscular synapse formation by a Cdk5-dependent mechanism. *Neuron*, 46(4), pp. 569-579.

Liu, X. et al., 2018. Changes in inflammatory and oxidative stress factors and the protein synthesis pathway in injured skeletal muscle after contusion.. *Experimental and Therapeutic Medicine*, Volume 15, pp. 2196-2202.

Li, Y. & Thompson, W., 2011. Nerve terminal growth remodels neuromuscular synapses in mice following regeneration of the postsynaptic muscle fiber.. *Journal of Neuroscience*, 31(37), pp. 13191-13203.

Lovering, R., 2013. *http://www.treat-nmd.eu/*. [Online]
Available at: http://www.treat-nmd.eu/downloads/file/sops/cmd/MDC1A_M.2.2.002.pdf
[Accessed 20th October 2017].

Lovering, R. & Brooks, S., 2014. Eccentric exercise in aging and diseased skeletal muscle: good or bad?. *Journal of Applied Physiology*, 116(11), p. 1439–1445.

Luo, A. T. C. H. S. Z. D. Z. A. G. Q. G. R. C. J., 2018. Changes in expression of autophagy-related factors during acute contusion repair of skeletal muscle.. *Chinese Journal of Applied Physiology*, 34(2), pp. 97-101.

M.A, R. & s, M., 2011. *Histopathology in Hematoxylin & Eosin stained muscle sections SOP.* Basel: s.n.

Mackinnon, S. & Dellon, A., 1988. Diagnosis of nerve injury.. In: *Surgery of the peripheral nerve.*. New York: Thieme Medical Publishers, pp. 74-79.

Macpherson, P., Schork, M. & Faulkner, J., 1996. Contraction-induced injury to single fiber segments from fast and slow muscles of rats by single stretches.. *American Journal of Cellular Physiology,* Volume 271, pp. 1438-1446.

Magill, C., 2009. Reinnervation of the Tibialis Anterior Following Sciatic Nerve Crush Injury: A Confocal Microscopic Study in Transgenic Mice.. *Experimental Neurology,* Volume 207, pp. 385-393.

Ma, J., Elsaidi, G. & Smith, T., 2004. Time course of recovery of juvenile skeletalmuscle after botulinumtoxin A injection: an animal model study.. *American Journal of PhysicalMedicine and Rehabilitation,* 83(10), p. 774–809.

Ma, J. et al., 2017. DNA-Mediated Gene Therapy in a Mouse Model of Limb Girdle Muscular Dystrophy 2B. *Molecular Therapy: Methods & Clinical Development,* Volume 7, pp. 123-131.

Manders, E. et al., 1992. Dynamics of 3-dimensional replication patterns during the S-phase, analyzed by double labeling of DNA and confocal microscopy.. *Journal of Cell Science,* Volume 103, pp. 857-862.

Manders, E., Verbeek, F. & Aten, J., 1993. Measurement of colocalization of objects in dual-color confocal images.. *Oxford Journal of Microscopy,* Volume 169, pp. 375-382.

Martinez-Martinez, P. et al., 2009. Silencing rapsyn in vivo decreases acetylcholine receptors and augments sodium channels and secondary postsynaptic membrane folding.. *Neurobiology of Disease,* Volume 35, pp. 14-23.

Masaru, I. & Yoshihisa, K., 2006. Muscarinic Acetylcholine Receptors. *Current Pharmaceutical Design,* 12(28), pp. 3573-3581.

McMahan, U., 1990. The agrin hypothesis.. *Cold Spring Harbor Symposia on Quantitative Biology,* Volume 55, pp. 407-418.

Menorca, R., Fussell, T. & Elfar, J., 2013. Peripheral Nerve Trauma: Mechanisms of Injury and Recovery. *Hand Clinics,* 29(3), pp. 317-330.

Meunier, F., Lisk, G., Sesardic, D. & Dolly, J., 2003. Dynamics of motor nerve terminal remodeling unveiled using SNARE-cleaving botulinum toxins: the extent and duration are dictated by the sites of SNAP-25 truncation.. *Molecular and Cellular,* 22(4), p. 454–466.

Misiaszek, J. & Pearson, K., 2002. Adaptive changes in locomotor activity following botulinumtoxin injection in ankle extensormuscles of cats.. *Journal of Neurophysiology,* 87(1), p. 229–239.

Mohammadi, J. et al., 2016. Comparison of repair of peripheral nerve transection in predegenerated muscle with and without a vein graft.. *BMC Neurology,* 16(237).

Morgan, D. & Allen, D., 1999. Early events in stretch-induced muscle damage.. *Journal of Applied Physiology,* Volume 87, pp. 2007-2015.

Mori, S. et al., 2017. Immunization of mice with LRP4 induces myasthenia similar to MuSK-associated myasthenia gravis.. *Experimental Neurology,* Volume 297, pp. 158-167.

Muller, J. et al., 2007. Phenotypical spectrum of DOK7 mutations in congenital myasthenic syndromes. *Brain*, Volume 130, pp. 1497-1506.

Muller, J. et al., 2010. Dok-7 promotes slow muscle integrity as well as neuromuscular junction formation in a zebrafish model of congenital myasthenic syndromes.. *Human Molecular Genetics*, 19(9), pp. 1726-1740.

Murakami, H., 2011. *1Q84.* New York: Knopf.

Myburgh, K., Kruger, M. & Smith, C., 2012. Accelerated skeletal muscle recovery after in vivo polyphenol administration.. *Journal of Nutritional Biochemistry*, Volume 23, p. 1072–1079.

Myckatyn, T. & Mackinnon, S., 2004. A review of research endeavors to optimize peripheral nerve reconstruction.. *Neurological Research*, 26(2), pp. 124-138.

Nachmansohn, D., 1955. Mechanisms of Impulse Transmission Across Neuromuscular Junctions. *American Journal of Physical Medicine*, 34(1), pp. 33-45.

Ngo, S., Noakes, P. & Phillips, W., 2007. Neural agrin: a synaptic stabiliser.. *International Journal of Biochemical Biology*, 39(5), pp. 867-867.

Nguyen, Q., Sanes, J. & Lichtman, J., 2002. Pre-existing pathways promote precise projection patterns.. *Natural Neuroscience*, Volume 5, pp. 861-867.

Nickel, E. & Potter, L. T., 1973. Ultrastructure of isolated membranes of Torpedo electric tissue.. *Brain Research*, Volume 57, pp. 508-517.

Nikolica, A. et al., 2016. Electrophysiological findings in patients with low density lipoprotein receptor related protein 4 positive myasthenia gravis. *European Journal of Neurology*, Volume 0, pp. 1-7.

Noakes, P. et al., 1993. 43k protein and acetylcholine receptors colocalize during the initial stages of neuromuscular synapse formation in vivo.. *Developmental Biology*, Volume 155, pp. 275-280.

Noller, C. et al., 2016. A Practical Approach to Quantitative Processing and Analysis of Small Biological Structures by Fluorescent Imaging. *Journal of Biomolecular Techniques*, 27(3), pp. 90-97.

Okada, K. et al., 2006. The muscle protein Dok-7 is essential for neuromuscular synaptogenesis.. *Science*, Volume 312, pp. 1802-1805.

Otsuka, K. et al., 2015. Collagen Q and anti-MuSK autoantibody competitively suppress agrin/LRP4/MuSK signaling. *Scientific Reports*, 13928(5).

Ozturk, C., 2015. Peripheral nerve surgery models sciatic nerve crush injury model.. *In Plastic and reconstructive surgery*, pp. 513-517.

Pannérec, A. et al., 2016. A robust neuromuscular system protects rat and human skeletal muscle from sarcopenia.. *Aging*, 8(4), pp. 712-728.

Pasteuning-Vuhman, S. et al., 2017. Natural disease history of mouse models for limb girdle. *PLoS One*, 12(8).

Patton, B., 2003. Basal lamina and the organization of neuromuscular synapses.. *Journal of Neurocytology,* 32(8), pp. 883-903.

Paulsen, G. et al., 2010. Time course of leukocyte accumulation in human muscle after eccentric exercise.. *Medical Science in Sport Exercise,* Volume 42, p. 75–85.

Pavic, R. et al., 2011. Rat siatic nerve crush injury and recovery tracked by plantar test and immuniohistochemistry analysis.. *Collegium Antropologicum,* 35(1), pp. 93-100.

Pearson, J. & Sabarra, A., 1974. A Method for Obtaining Longitudinal Cryostat Sections of Living Muscle Without Contraction Artifacts. *Stain Technology,* 49(3), pp. 143-146.

Pick, J., 1954. The Evolution of Homeostasis: The Phylogenetic Development of the Regulation of Bodily and Mental Activities by the Autonomic Nervous System. *Proceedings of the American Philosophical Society,* 95(5), pp. 298-303.

Plate, J. et al., 2014. Age-related changes affect rat rotator cuff muscle function.. *Journal of Shoulder and Elbow Surgery,* Volume 23, pp. 91-98.

Pratt, S. L. R., 2014. A stepwise procedure to test contractility and susceptibility to injury for the rodent quadriceps muscle.. *Journal of Biological Methods,* 1(2).

Pratt, S. et al., 2013. Effects of in vivo injury on the neuromuscular junction in healthy and dystrophic muscles.. *The Journal of Physiology,* 591(2), pp. 559-570.

Punga, A. et al., 2011. Muscle-selective synaptic disassembly and reorganization in MuSK antibody positive MG mice. *Experimental Neurology,* Volume 230, pp. 207-217.

Punga, A. & Reugg, M., 2012. Signaling and aging at the neuromuscular synapse: lessons learnt from neuromuscular diseases.. *Current Opinion on Pharmacology,* 12(3), pp. 340-346.

Purves, D. et al., 2011. *Neuroscience.* 5th ed. Sunderland, USA: Sinauer Associates.

Rader, E. et al., 2006. Raising the antioxidant levels within mouse muscle fibres does not affect contraction-induced injury.. *Experimental Physiology,* Volume 91, pp. 781-789.

Raftery, M. A. et al., 1974. The biochemistry of an acetylcholine receptor.. *Journal of Supramolecular Structure,* Volume 2, pp. 582-592.

Ramarao, M., Bianchetta, M., Lanken, J. & Cohen, J., 2001. Role of Rapsyn Tetratricopeptide Repeat and Coiled-coil Domains in Self-association and Nicotinic Acetylcholine Receptor Clustering. *Journal of Biological Chemistry,* 276(10), pp. 7475-7483.

Rich, M. & Lichtman, J., 1989. In vivo visualization of pre- and postsynaptic changes during synapse elimination in reinnervated mouse muscle.. *Journal of Neuroscience,* Volume 9, pp. 1781-1805.

Rinkevich, Y. et al., 2016. Denervation of Mouse Lower Hind Limb by Sciatic and Femoral Nerve Transection. *Bio-Protocol,* 6(13).

Robinson, G. & Madison, R., 2009. Influence of terminal nerve branch size on motor neuron regeneration accuracy.. *Experimental Neurology,* 215(2), pp. 228-235.

Rochester, L., Chandler, C. & Johnson, M., 1995. Influence of electrical stimulation of the tibialis anterior muscle in paraplegic subjects.. *Paraplegia,* Volume 33, p. 437– 449.

Ronchi, G. et al., 2009. Functional and morphological assessment of a standardized crush injury of the rat median nerve.. *Journal of Neuroscience Methods*, 179(1), pp. 51-57.

Rubinstein, I. et al., 1998. Involvement of Nitric Oxide System in Experimental Muscle Crush Injury. *Journal of Clinical Investigation,* 101(6), p. 1325–1333.

Rudolf, R. K. M. L. S. D. M., 2014. Degeneration of neuromuscular junction in age and dystrophy. *Frontiers in Aging Neuroscience,* 6(99).

Rydevik, B. & Lundborg, G., 1977. Permeability of intraneural microvessels and perineurium following acute, graded experimental nerve compression.. *Scandinavian Journal of and Reconstructive Surgery,* 11(3), pp. 179-187.

Saitoh, T., Oswald, R., Wennogle, L. P. & Changeux, J. P., 1980. Conditions for the selective labelling of the 66,000 Dalton chain of the acetylcholine receptor by the covalent noncompetitive blocker 5-azido-[3H]trimethisoquin.. *FEBS Lett,* Volume 116, pp. 30-36.

Sakuma, M. et al., 2016. Lack of motor recovery after prolonged denervation of the neuromuscular junction is not due to regenerative failure. *European Journal of Neuroscience,* 43(3), pp. 451-462.

Sanes, J. & Chiu, A., 1983. The Basal Lamina of the Neuromuscular Junction. *Cold Spring Harbor Symposia on Quantitative Biology ,* Volume 48, pp. 667-678.

Sanes, J. & Lichtman, J., 2001. Induction, assembly, maturation and maintenance of a postsynaptic apparatus.. *Natural Review of Neuroscience,* 2(11), pp. 791-805.

Santos, A. & Caroni, P., 2003. Assembly, plasticity and selective vulnerability to disease of mouse neuromuscular junctions.. *Journal of Neurocytology,* 32(5), pp. 849-862.

Sarica, S. & Altun, I., 2018. The effects on peripheral nerve damage of the application of local and systemic erythropoietin.. *Bratislav Medical Journal,* 119(9), pp. 602-607.

Sarikcioglu, L. et al., 2007. Effect of severe crush injury on axonal regeneration: A functional and ultrastructural study.. *Journal of Reconstructive Microsurgery*, 23(3), pp. 143-149.

Sawyer, R., 2017. s.l.:CBC.

Schmelzer, J., Zochodne, D. & Low, P., 1989. Ischemic and reperfusion injury of rat peripheral nerve.. *Proceedings of the National Academy of Sciences of the United States of America,* 86(5), pp. 1639-1642.

Schoen, M. et al., 2007. Ischemic preconditioning prevents skeletal muscle tissue injury, but not nerve lesion upon tourniquet-induced ischemia.. *Journal of Trauma,* Volume 63, pp. 788-797.

Scott, W. et al., 2006. Contractile Properties and the Force-Frequency Relationship of the Paralyzed Human Quadriceps Femoris Muscle. *Physical Therapy*, 86(6), pp. 788-799.

Sealock, R., Barnaby, E. & Froehner, S., 1984. Ultrastructure localization of the Mr 43,000 protein and the acetylcholine receptor in Torpedo postsynaptic membranes using monoclonal antibodies.. *Journal of Cellular Biology,* Volume 98, pp. 2239-2244.

Seddon, H., 1943. Three types of nerve injury.. *Brain,* 66(4), pp. 237-288.

Shen, J., Ma, J. & Elsaidi, G., 2005. Gene expression of myogenic regulatory factors following intramuscular injection of botulinum A toxin in juvenile rats. *Neuroscience Letters,* 381(3), pp. 207-210.

Shen, J. et al., 2006. How muscles recover from paresis and atrophy after intramuscular injection of botulinum toxin A: Study in juvenile rats.. *Journal of Orthopaedic Research,* 24(5), pp. 1128-1135.

Shi, L., Fu, A. & Ip, N., 2012. Molecular mechanisms underlying maturation and maintenance of the vertebrate neuromuscular junction.. *Trends in Neuroscience,* 35(7), pp. 441-453.

Sieck, D. et al., 2012. Structure-activity relationships in rodent diaphragm muscle fibers vs. neuromuscular junctions.. *Respiratory Physiology & Neurobiology,* Volume 180, pp. 88-96.

Silva, D. et al., 2010. End-to-side nerve repair using fibrin glue in rats.. *Acta Cirúrgica Brasileira,* 25(2), pp. 158-162.

Simon-Chazottes, D. et al., 2006. Mutations in the gene encoding the low-density lipoprotein receptor LRP4 cause abnormal limb development in the mouse.. *Genomics,* Volume 87, pp. 673-677.

Singh, B., 2006. Botulinum neurotoxin structure, engineering, and novel cellular trafficking and targeting.. *Neurotoxicity Research,* 9(2-3), p. 73–92.

Song, D. et al., 2018. Effect of high frequency electromagnetic wave stimulation on muscle injury in a rat model.. *Injury,* 49(6), pp. 1032-1037.

Spiro, A., Shy, G. & Gonatas, N., 1966. Myotubular myopathy. Persistence of fetal muscle in an adolescent boy.. *Archives of Neurology,* Volume 14, p. 1–14.

Stephan, A. et al., 2008. Neurotrypsinj cleaves agrin locally at the synapse.. *FASEB Journal,* 22(6), pp. 1861-1873.

Stone, M. et al., 2007. Absence of keratin 19 in mice causes skeletal myopathy with mitochondrial and sarcolemmal reorganization.. *Journal of Cellular Science,* Volume 120, p. 3999–4008.

Stratton, S., Heckman, R. & Francis, R., 1984. Therapeutic Ultrasound: Its Effects on the Integrity of a Non-Penetrating Wound. *Journal of Orthopaedic & Sports Physical Therapy,* 5(5), pp. 278-281.

Strochlic, L., Cartaud, A. & Cartaud, J., 2005. The synaptic muscle-specific kinase (MuSK) complex: new partners, new functions. *BioEssays,* 27(11), pp. 1129-1135.

Sulaiman, W. & Gordon, T., 2014. Neurobiology of peripheral nerve injury, regeneration, and functional recovery: From bench top research to bedside application.. *The Ochsner Journal,* 13(1), pp. 100-108.

Sunderland, S., 1951. A classification of peripheral nerve injuries producing loss of function.. *Brain,* 74(4), pp. 491-516.

Swartling, C. et al., 2001. Side-effects of intradermal injections of botulinum A toxin in the treatment of palmar hyperhidrosis: a neurophysiological study.. *European Journal of Neurology,* 8(5), p. 451–456.

Takamori, M., 2012. Structure of the neuromuscular junction: function and cooperative mechanisms in the synapse. *Annals of the New York Academy of Science,* Volume 1274, pp. 14-23.

Thomas, M. et al., 2014. Early oxidative shifts in mouse skeletal muscle morphology with high-fat diet consumption do not lead to functional improvements. *Physiological Reports,* 2(9).

Tomas, J., Fenoll, R., Mayayo, E. & Santafe, M., 1990. Branching pattern of motor nerve endings in a skeletal muscle of the adult rat.. *Journal of Anatomy,* Volume 168, p. 123–135.

Tomazoni, S. et al., 2017. Effects of photobiomodulation therapy and topical non-steroidal anti-inflammatory drug on skeletal muscle injury induced by contusion in rats—part 1: morphological and functional aspects. *Lasers in Medical Science,* 32(9), p. 2111–2120.

Tran, T. et al., 2011. Tourniquet-induced acute ischemia-reperfusion injury in mouse skeletal muscles: Involvement of superoxide.. *European Journal of Pharmacology,* Volume 650, pp. 328-334.

Tsai, S. C. H. C. C. C., 2013. Molecular Mechanisms of Treadmill Therapy on Neuromuscular Atrophy Induced via Botulinum Toxin A. *Neural Plasticity.*

Tsai, S. H. Y. L. M. H. H. H. C. T. Y., 2018. Effects of dextrose prolotherapy on contusion-induced muscle injuries in mice.. *International Journal of Medical Sciences,* 15(11), pp. 1251-1259.

Tsai, S., Tung, Y. & Chen, H., 2013. Treadmill running upregulates the expression of acetylcholine receptor in rat gastrocnemius following botulinum toxin A injection.. *Journal of Orthopaedic Research,* 31(1), p. 125–131.

Tu, H. et al., 2017. Morphological regeneration and functional recovery of neuromuscular junctions after tourniquet-induced injuries in mouse hindlimb.. *Frontiers in Physiology,* 8(207).

Turturro, A. et al., 1999. Growth curves and survival characteristics of the animals used in the biomarkers of aging programme.. *Journals of Gerontology: Series A, Biological Sciences and Medical Sciences,* Volume 54, pp. 492-501.

Unwin, N., 2005. Refined structure of the nicotinic acetylcholine receptor at 4 Å resolution.. *Journal of Molecular Biology,* Volume 346, pp. 967-989.

Valdez, G. et al., 2010. Attenuation of age-related changes in mouse neuromuscular synapses by caloric restriction and exercise.. *Proceedings of the National Academy of Sciences of the USA,* Volume 107, p. 14863–14868.

Valenzuela, D. et al., 1995. Receptor tyrosine kinase specific for the skeletal muscle lineage: expression in embryonic muscle, at the neuromuscular junction, and after injury.. *Neuron,* Volume 15, pp. 573-584.

Varejão, A. et al., 2004. Functional and morphological assessment of a standardized rat sciatic nerve crush injury with a non-serrated clamp.. *Journal of Neurotrauma,* 21(11), pp. 1652-1670.

Vargas, M. & Barres, B., 2007. Why is wallerian degeneration in the CNS so slow?. *Annual Review of Neuroscience,* Volume 30, pp. 153-179.

Vignaud, A. et al., 2010. Impaired skeletal muscle repair after ischemia-reperfusion in mice.. *Journal of Biomedical Biotechnology.*

Wang, F. et al., 1996. Assembly of Human Neuronal Nicotinic Receptor α5 Subunits with α3, β2, and β4 Subunits. *Journal of Biological Chemistry,* Volume 271, pp. 17656-17665.

Weill, C. L., McNamee, M. G. & Karlin, A., 1974. Affinity labeling of purified acetylcholine receptor from Torpedo californica.. *Biochemical and Biophysical Research Communities,* Volume 61, pp. 997-1003.

White, D., 2011. *Biopolis Dresden Imaging Platform.* [Online]
Available at: https://www.biodip.de/w/images/6/67/2011-10-Basics_of_Imaging_Processing_Course.pdf
[Accessed 14 December 2017].

Wilson, M. & Deschenes, M., 2005. The neuromuscular junction: anatomical features and adaptations to various forms of increased, or decreased neuromuscular activity.. *International Journal of Neuroscience,* Volume 115, pp. 803-828.

Winkler, T. et al., 2011. Time course of skeletal muscle regeneration after severe trauma. *Acta Orthopaedica,* 82(1), p. 102–111.

Witzemann, V., Brenner, H. & Sakmann, B., 1991. factors regulate AChR subunit mRNAs at rat neuromuscular synapses.. *Journal of Cellular Biology,* Volume 114, pp. 125-141.

Wright-Carpenter, T. et al., 2004. Treatment of muscle injuries by local administration of autologous conditioned serum: animal experiments using a muscle contusion model.. *International Journal of Sports Medicine,* 25(8), pp. 582-587.

Yamanashi, Y., Higuchi, O. & D, B., 2008. Dok-7/MuSK signaling and a congenital myasthenic syndrome. *Acta Myologica,* Volume 27, pp. 25-29.

Yampolsky, P. et al., 2010. Time Lapse in Vivo Visualization of Developmental Stabilization of Synaptic Receptors at Neuromuscular Junctions. *The Journal of Biological Chemistry,* 285(45), pp. 34589-34596.

Yampolsky, P., Pacifici, P. & Witzemann, V., 2010. Differential muscle-driven synaptic remodeling in the neuromuscular junction after denervation.. *European Journal of Neuroscience,* 31(4), pp. 646-658.

Young, B., O'Dowd, G. & Woodford, P., 2013. Basic Tissue Types; Muscle. In: A. Hall, ed. *Wheater's Functional Histology.* Philadelphia: Elsevier Church Livingstone.

Zhang, B. et al., 2008. LRP4 serves as a co-receptor of agrin. *Neuron,* 60(2), pp. 285-297.

Zhu, D., Xiong, W. & Mei, L., 2006. Lipid rafts serve as a signaling platform for nicotinic acetylcholine receptor clustering.. *Journal of Neuroscience,* 26(18), pp. 4841-4851.

Zhu, Z. et al., 2014. Sarcolemmal ATP-sensitive potassium channels modulate skeletal. *Journal of General Physiology,* 143(1), pp. 119-134.

Zimmerman, B. & Granger, D., 1994. Mechanisms of reperfusion injury. *The American Journal of the Medical Sciences,* 307(4), pp. 284-292.

ADDENDA

Addendum A

H&E Automated Staining Protocol

Slides were soaked in each reagent for 2 minutes before being transferred to the next reagent. Once protocol was completed, slides were left to air dry before coverslips were mounted.

1. Distilled water (room temperature)
2. Mayer's Hematoxylin
3. Warm tap water
4. Scott's Tap Water
5. 95% Alcohol
6. Eosin Y
7. 95% Alcohol
8. 100% Alcohol
9. 100% Alcohol

Mayer's Hematoxylin

Scott's Tap Water – 10% in dH_2O

Eosin Y – 5% in dH_2O; diluted 20X in 90% alcohol

Addendum B

IHC Staining Protocol

1. Fix in paraformaldehyde (PFA) for 8 minutes [only longitudinal sections].
2. Permeabilise with triton X for 15 minutes.
3. Wash in PBS for 3 x 5 minutes.
4. Block with donkey serum for 1 hour.
5. Wash in PBS for 3 x 5 minutes.
6. Incubate with primary antibody overnight at 4° C.
7. Wash in PBS for 3 x 5 minutes.
8. Incubate with secondary antibody for 4 hours at RT.
9. Wash in PBS for 3 x 5 minutes.
10. Stain with α-Bungarotoxin (conjugated) for 1 hour at RT.
11. Wash in PBS for 3 x 5 minutes.
12. Stain with Hoechst for 15 minutes.
13. Wash in PBS for 3 x 5 minutes.
14. Mount with Dako fluorescent mounting media.

PFA – 1% in dH_2O

Triton X – 0.1%

PBS – 1X

Blocking Serum – 5% Donkey Serum + 0.2% Triton X (make up in 1% BSA)

Primary and Secondary Antibodies made up in 1% BSA

α-Bungarotoxin – 1 in 500 (make up in 1% BSA)

Hoechst – 1 in 1000 (make up in 1% BSA)

Addendum C

Endplate Selection Criteria

As described in Section 2.4.4.4, certain criteria were used to select which endplates were viable for image analysis. The criteria were strictly adhered to in an effort to ensure continuity of conditions across all images. Figure C.1 shows images of endplates that are viewed side-on (as opposed to en face). This is commonly seen in cross-sections, as the AChR is orientated along the length of the muscle fibre, and thus must be viewed in longitudinal sections. Due to the bulging shape of the *gastrocnemius*, distal fibres can be sectioned in diagonal or cross-sections even when in longitudinal orientation. Therefore it is important to ensure that NMJs are in en face view to be included in the image analysis to avoid inaccurate measurements of the TOA and TSA.

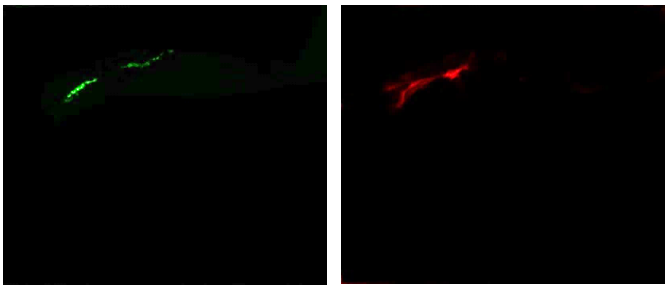

Figure C.1 AChR and Rapsyn viewed from the side. AChR is not in en face view.

Figure C.2 shows images of damaged AChRs that are situated amongst sites of extreme tissue destruction. As a result, immunohistochemical staining of the synaptic components produces widespread fluorescent signal due to the injury-induced debris. The extensive fluorescent reactivity is an inaccurate representation of positive antibody signal as the specificity is reduced in the presence of immense debris. Areas of considerable disruption to the tissue can be identified by clusters of myonuclei (stained blue with DAPI), surrounded by intense dispersed signal of the respective synaptic protein of interest.

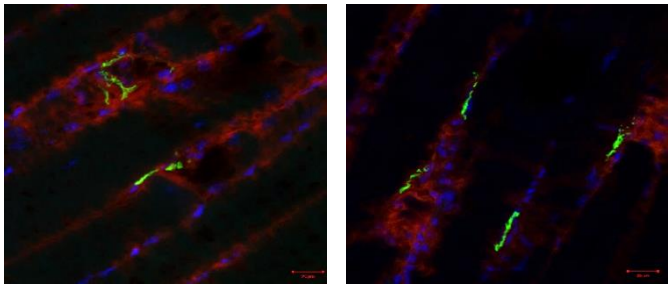

Figure C.2 AChR and Rapsyn imaged amongst debris. AChR located near injury-induced debris.

Certain conditions can also result in diffuse background signal across the entirety of the muscle fibre. This is as a result of a mismatch in reactivity of the given primary and its appropriate secondary. Troubleshooting to address the problem will usually rectify the issue. Therefore, images with high background signal (see Figure C.3) must be excluded from image analysis to prevent inaccurate quantification.

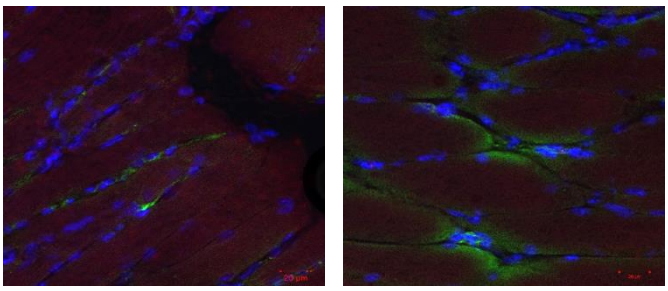

Figure C.3 Rapsyn channel producing high background signal.

Addendum D

ELISA Kit Protocol

Reagent Preparation:

1. Bring all kit components and samples to room temperature (18° - 25° C) before use. If the kit will not be used up in one time, please only take out strips and reagents for present experiment and leave the remaining strips and reagents in required condition.
2. **Standard -** Reconstitute the **Standard** with 1.0mL of **Standard Diluent,** kept for 10 minutes at room temperature, shake gently (not to foam). The concentration of the standard in the stock solution is 10ng/mL. Please prepare 7 tubes containing 0.5mL Standard Diluent and produce a double dilution series according to the picture shown below. Mix each tube thoroughly before the next transfer. Set up 7 points of diluted standard such as 10ng/mL, 5ng/mL, 2.5ng/mL, 1.25ng/mL, 0.625ng/mL, 0.312ng/mL, 0.156ng/mL, and the last EP tube with **Standard Diluent** is the blank as 0ng/mL
3. **Detection Reagent A and Detection Reagent B -** Briefly spin or centrifuge the stock Detection A and Detection B before use. Dilute them to the working concentration 100-fold with **Assay Diluent A** and **B**, respectively.
4. **Wash Solution** - Dilute 20mL of Wash Solution concentrate (30×) with 580mL of deionised or distilled water to prepare 600mL of Wash Solution (1×).
5. **TMB substrate** - Aspirate the needed dosage of the solution with sterilised tips and do not dump the residual solution into the vial again.

Assay Procedure:

1. Determine wells for diluted standard, blank and sample. Prepare 7 wells for standard, 1 well for blank. Add 100µL each of dilutions of standard (read Reagent Preparation), blank and samples into the appropriate wells. Cover with the Plate sealer. Incubate for 1 hour at 37oC.
2. Remove the liquid of each well, don't wash.
3. 3. Add 100µL of **Detection Reagent A** working solution to each well, cover the wells with the plate sealer and incubate for 1 hour at 37oC.
4. Aspirate the solution and wash with 350µL of 1× Wash Solution to each well using a squirt bottle, multi-channel pipette, manifold dispenser or autowasher, and let it sit for 1~2 minutes. Remove the remaining liquid from all wells completely by snapping the plate onto absorbent paper. Totally wash 3 times. After the last wash, remove any remaining Wash Buffer by aspirating or decanting. Invert the plate and blot it against absorbent paper.
5. Add 100µL of **Detection Reagent B** working solution to each well, cover the wells with the plate sealer and incubate for 30 minutes at 37oC.
6. Repeat the aspiration/wash process for total 5 times as conducted in step 4.
7. Add 90µL of **Substrate Solution** to each well. Cover with a new Plate sealer. Incubate for 10 - 20 minutes at 37oC (Don't exceed 30 minutes). Protect from light. The liquid will turn blue by the addition of Substrate Solution.
8. Add 50µL of **Stop Solution** to each well. The liquid will turn yellow by the addition of Stop solution. Mix the liquid by tapping the side of the plate. If colour change does not appear uniform, gently tap the plate to ensure thorough mixing.
9. Remove any drop of water and fingerprint on the bottom of the plate and confirm there is no bubble on the surface of the liquid. Then, run the microplate reader and conduct measurement at 450nm immediately.

Addendum E

Combined Body Mass Means

Table E.1 Pre- and post-injury mouse body mass comparison.

	Mean Pre-injury Mass	**SD**	**Mean Post-injury Mass**	**SD**
D0	28.36	1.33	28.36	1.33
D3	26.64	3.00	25.76	2.34
D7	25.96	2.85	26.71	2.57
D14	29.06	1.40	28.34	0.91
Combined	**27,42**	**2,59**	**27,18**	**2,178**

Addendum F

Combined Timepoints Force Testing Data

Table F.1 Significance between Baseline (B) and Injury Groups.

* where P < 0.05; ** where P < 0.01 and *** where P < 0.001			
Frequency	B vs D3	B vs D7	B vs D14
60 Hz	*	ns	ns
75 Hz	ns	ns	ns
90 Hz	**	ns	*
105 Hz	***	**	**
120 Hz	***	***	**

Addendum G

ELISA Standard Curve Data

Standard curve dilutions tested in triplicates (N = 3) of each concentration at 10ng/mL, 5ng/mL, 2.5ng/mL, 1.25ng/mL, 0.625ng/mL, 0.312ng/mL, 0.156ng/mL and a blank well.

Table G.1 Triplicate OD readings for ELISA standard curve dilutions.

Conc	0	0,156	0,312	0,625	1,25	2,5	5	10
R1	0,114	0,161	0,205	0,347	0,788	1,444	2,295	3,206
R2	0,137	0,203	0,275	0,533	0,788	1,416	2,691	3,095
R3	0,146	0,208	0,272	0,406	0,721	1,626	2,036	2,965
Mean	0,132333	0,190667	0,250667	0,428667	0,765667	1,495333	2,340667	3,088667
Zero Mean	0	0,058333	0,118333	0,296333	0,633333	1,363	2,208333	2,956333
SD	0,016503	0,025813	0,039577	0,095049	0,038682	0,114023	0,329879	0,120625

Addendum H

IHC Quantification Descriptive Statistics

Table H.1 TOA measurements for AChR and Rapsyn from IHC images pre- and post-injury.

Cell No.	protein*Treatment; LS Means (Spreadsheet9 in STATS.stw) Current effect: F(3, 36)=332.28, p=0.0000 Type III decomposition						
	protein	Treatment	TOA Mean	TOA Std.Err.	TOA -95.00%	TOA +95.00%	N
1	AChR	0	583,6680	11,96268	559,4066	607,9294	10
2	AChR	3	256,9560	11,96268	232,6946	281,2174	10
3	AChR	7	220,1280	11,96268	195,8666	244,3894	10
4	AChR	14	461,2800	11,96268	437,0186	485,5414	10
5	Rapsyn	0	577,4440	11,96268	553,1826	601,7054	10
6	Rapsyn	3	889,2120	11,96268	864,9506	913,4734	10
7	Rapsyn	7	404,8480	11,96268	380,5866	429,1094	10
8	Rapsyn	14	443,9120	11,96268	419,6506	468,1734	10

Table H.2 TSA measurements for AChR and Rapsyn from IHC images pre- and post-injury.

Cell No.	protein*Treatment; LS Means (Spreadsheet9 in STATS.stw) Current effect: F(3, 36)=128.60, p=0.0000 Type III decomposition						
	protein	Treatment	TSA Mean	TSA Std.Err.	TSA -95.00%	TSA +95.00%	N
1	AChR	0	309,8440	8,957783	291,6768	328,0112	10
2	AChR	3	150,7800	8,957783	132,6128	168,9472	10
3	AChR	7	140,3000	8,957783	122,1328	158,4672	10
4	AChR	14	283,2800	8,957783	265,1128	301,4472	10
5	Rapsyn	0	300,4560	8,957783	282,2888	318,6232	10
6	Rapsyn	3	453,0160	8,957783	434,8488	471,1832	10
7	Rapsyn	7	285,6800	8,957783	267,5128	303,8472	10
8	Rapsyn	14	295,9000	8,957783	277,7328	314,0672	10

Table H.1 Staining Density measurements for AChR and Rapsyn from IHC images pre- and post-injury.

Cell No.	protein*Treatment; LS Means (Spreadsheet9 in STATS.stw) Current effect: F(3, 36)=56.967, p=.00000 Type III decomposition						
	protein	Treatment	SD Mean	SD Std.Err.	SD -95.00%	SD +95.00%	N
1	AChR	0	0,092284	0,004599	0,082957	0,101611	10
2	AChR	3	0,127868	0,004599	0,118541	0,137195	10
3	AChR	7	0,122390	0,004599	0,113063	0,131718	10
4	AChR	14	0,075549	0,004599	0,066222	0,084876	10
5	Rapsyn	0	0,064709	0,004599	0,055381	0,074036	10
6	Rapsyn	3	0,032834	0,004599	0,023506	0,042161	10
7	Rapsyn	7	0,045279	0,004599	0,035952	0,054606	10
8	Rapsyn	14	0,088870	0,004599	0,079543	0,098197	10

Table H.4 TOA measurements for AChR and MuSK from IHC images pre- and post-injury.

Cell No.	protein*Treatment; LS Means (Spreadsheet9 in STATS.stw) Current effect: F(3, 36)=196.87, p=0.0000 Type III decomposition						
	protein	Treatment	TOA Mean	TOA Std.Err.	TOA -95.00%	TOA +95.00%	N
1	AChR	0	309,781	16,40377	276,5130	343,050	10
2	AChR	3	336,027	16,40377	302,7585	369,295	10
3	AChR	7	416,426	16,40377	383,1574	449,694	10
4	AChR	14	365,293	16,40377	332,0243	398,561	10
5	MuSK	0	295,689	16,40377	262,4207	328,957	10
6	MuSK	3	1000,665	16,40377	967,3964	1033,933	10
7	MuSK	7	487,966	16,40377	454,6971	521,234	10
8	MuSK	14	362,138	16,40377	328,8699	395,407	10

Table H.5 TSA measurements for AChR and MuSK from IHC images pre- and post-injury.

Cell No.	protein*Treatment; LS Means (Spreadsheet9 in STATS.stw) Current effect: F(3, 36)=252.70, p=0.0000 Type III decomposition						
	protein	Treatment	TSA Mean	TSA Std.Err.	TSA -95.00%	TSA +95.00%	N
1	AChR	0	133,4582	7,944299	117,3464	149,5700	10
2	AChR	3	106,7208	7,944299	90,6090	122,8326	10
3	AChR	7	118,7885	7,944299	102,6767	134,9003	10
4	AChR	14	124,0123	7,944299	107,9005	140,1241	10
5	MuSK	0	142,8397	7,944299	126,7279	158,9515	10
6	MuSK	3	505,4688	7,944299	489,3570	521,5806	10
7	MuSK	7	297,7373	7,944299	281,6255	313,8491	10
8	MuSK	14	158,6036	7,944299	142,4918	174,7154	10

Table H.6 Staining Density measurements for AChR and MuSK from IHC images pre- and post-injury.

Cell No.	protein*Treatment; LS Means (Spreadsheet9 in STATS.stw) Current effect: F(3, 36)=28.583, p=.00000 Type III decomposition						
	protein	Treatment	SD Mean	SD Std.Err.	SD -95.00%	SD +95.00%	N
1	AChR	0	0,321853	0,011731	0,298061	0,345646	10
2	AChR	3	0,350135	0,011731	0,326342	0,373927	10
3	AChR	7	0,249569	0,011731	0,225776	0,273361	10
4	AChR	14	0,240847	0,011731	0,217054	0,264639	10
5	MuSK	0	0,140225	0,011731	0,116432	0,164017	10
6	MuSK	3	0,022687	0,011731	-0,001106	0,046479	10
7	MuSK	7	0,056155	0,011731	0,032363	0,079948	10
8	MuSK	14	0,124894	0,011731	0,101101	0,148686	10

Table H.7 TOA measurements for AChR and LRP4 from IHC images pre- and post-injury.

Cell No.	protein*Treatment; LS Means (Spreadsheet9 in STATS.stw) Current effect: F(3, 36)=248.41, p=0.0000 Type III decomposition						
	protein	Treatment	TOA Mean	TOA Std.Err.	TOA -95.00%	TOA +95.00%	N
1	AChR	0	335,512	12,93711	309,274	361,750	10
2	AChR	3	403,352	12,93711	377,114	429,590	10
3	AChR	7	456,465	12,93711	430,227	482,703	10
4	AChR	14	239,760	12,93711	213,523	265,998	10
5	LRP4	0	315,932	12,93711	289,694	342,170	10
6	LRP4	3	962,084	12,93711	935,846	988,322	10
7	LRP4	7	1041,679	12,93711	1015,441	1067,917	10
8	LRP4	14	479,599	12,93711	453,362	505,837	10

Table H.8 TSA measurements for AChR and LRP4 from IHC images pre- and post-injury.

Cell No.	protein*Treatment; LS Means (Spreadsheet9 in STATS.stw) Current effect: F(3, 36)=348.84, p=0.0000 Type III decomposition						
	protein	Treatment	TSA Mean	TSA Std.Err.	TSA -95.00%	TSA +95.00%	N
1	AChR	0	230,7350	10,24760	209,9519	251,5181	10
2	AChR	3	161,9440	10,24760	141,1609	182,7271	10
3	AChR	7	177,2919	10,24760	156,5088	198,0750	10
4	AChR	14	201,1598	10,24760	180,3767	221,9429	10
5	LRP4	0	158,1145	10,24760	137,3314	178,8976	10
6	LRP4	3	372,2320	10,24760	351,4489	393,0151	10
7	LRP4	7	650,9833	10,24760	630,2002	671,7664	10
8	LRP4	14	276,0132	10,24760	255,2301	296,7963	10

Table H.9 Staining Density measurements for AChR and LRP4 from IHC images pre- and post-injury.

Cell No.	protein*Treatment; LS Means (Spreadsheet9 in STATS.stw) Current effect: F(3, 36)=21.481, p=.00000 Type III decomposition						
	protein	Treatment	SD Mean	SD Std.Err.	SD -95.00%	SD +95.00%	N
1	AChR	0	0,120488	0,007409	0,105462	0,135514	10
2	AChR	3	0,110026	0,007409	0,095000	0,125052	10
3	AChR	7	0,136520	0,007409	0,121494	0,151546	10
4	AChR	14	0,152695	0,007409	0,137669	0,167721	10
5	LRP4	0	0,124814	0,007409	0,109788	0,139840	10
6	LRP4	3	0,071064	0,007409	0,056038	0,086090	10
7	LRP4	7	0,039740	0,007409	0,024714	0,054766	10
8	LRP4	14	0,153083	0,007409	0,138057	0,168109	10

Table H.10 TOA measurements for AChR and Dok7 from IHC images pre- and post-injury.

Cell No.	protein*Treatment; LS Means (Spreadsheet9 in STATS.stw) Current effect: F(3, 36)=236.70, p=0.0000 Type III decomposition						
	protein	Treatment	TOA Mean	TOA Std.Err.	TOA -95.00%	TOA +95.00%	N
1	AChR	0	333,4573	10,05904	313,0566	353,8580	10
2	AChR	3	360,2440	10,05904	339,8433	380,6447	10
3	AChR	7	249,6189	10,05904	229,2182	270,0196	10
4	AChR	14	416,4618	10,05904	396,0611	436,8625	10
5	Dok7	0	303,2487	10,05904	282,8480	323,6494	10
6	Dok7	3	640,3701	10,05904	619,9694	660,7708	10
7	Dok7	7	368,0908	10,05904	347,6901	388,4915	10
8	Dok7	14	313,4528	10,05904	293,0521	333,8535	10

Table H.11 TSA measurements for AChR and Dok7 from IHC images pre- and post-injury.

Cell No.	protein*Treatment; LS Means (Spreadsheet9 in STATS.stw) Current effect: F(3, 36)=120.99, p=0.0000 Type III decomposition						
	protein	Treatment	TSA Mean	TSA Std.Err.	TSA -95.00%	TSA +95.00%	N
1	AChR	0	226,0360	10,69595	204,3436	247,7284	10
2	AChR	3	166,5910	10,69595	144,8986	188,2834	10
3	AChR	7	200,5151	10,69595	178,8227	222,2075	10
4	AChR	14	229,5639	10,69595	207,8715	251,2563	10
5	Dok7	0	159,7214	10,69595	138,0290	181,4138	10
6	Dok7	3	429,1280	10,69595	407,4356	450,8204	10
7	Dok7	7	237,6196	10,69595	215,9272	259,3120	10
8	Dok7	14	214,9746	10,69595	193,2822	236,6670	10

Table H.12 Staining Density measurements for AChR and Dok7 from IHC images pre- and post-injury.

Cell No.	protein*Treatment; LS Means (Spreadsheet9 in STATS.stw) Current effect: F(3, 36)=2.1438, p=.11174 Type III decomposition						
	protein	Treatment	SD Mean	SD Std.Err.	SD -95.00%	SD +95.00%	N
1	AChR	0	0,124247	0,005726	0,112636	0,135859	10
2	AChR	3	0,095944	0,005726	0,084332	0,107555	10
3	AChR	7	0,117609	0,005726	0,105997	0,129221	10
4	AChR	14	0,113161	0,005726	0,101549	0,124773	10
5	Dok7	0	0,124890	0,005726	0,113278	0,136502	10
6	Dok7	3	0,071230	0,005726	0,059618	0,082842	10
7	Dok7	7	0,103447	0,005726	0,091835	0,115059	10
8	Dok7	14	0,091839	0,005726	0,080227	0,103451	10

Addendum I

Additional IHC Quantification Variables

Figure I.1 Staining Intensity measurements for AChR and rapsyn from IHC images pre- and post-injury.

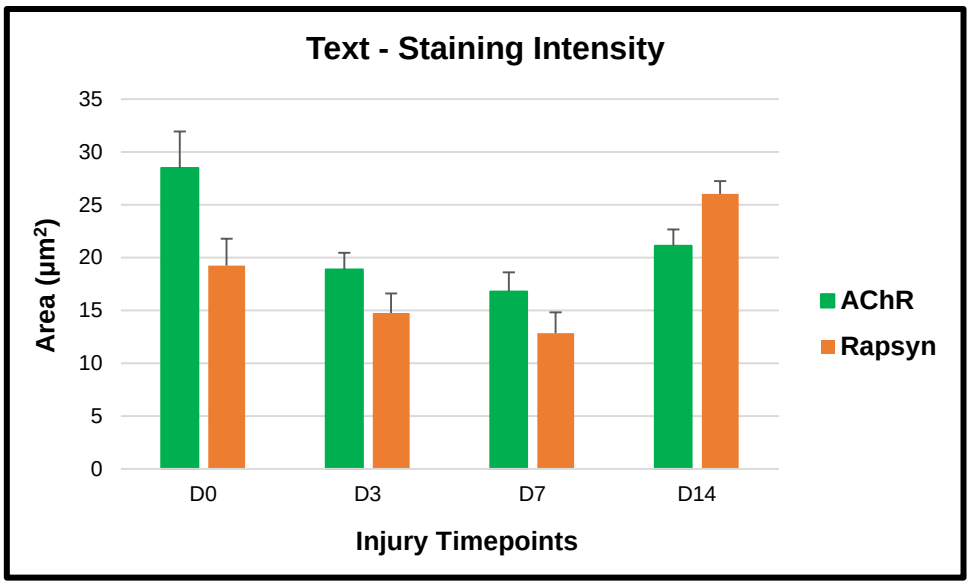

Figure I.2 Total Outline Perimeter (TOP) measurements for AChR and rapsyn from IHC images pre- and post-injury.

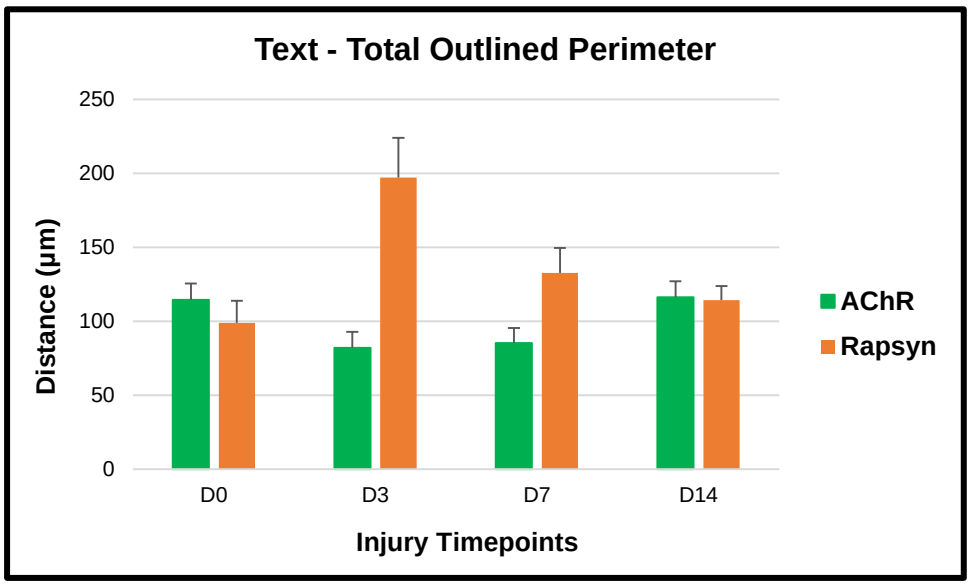

Figure I.3 Staining Intensity measurements for AChR and MuSK from IHC images pre- and post-injury.

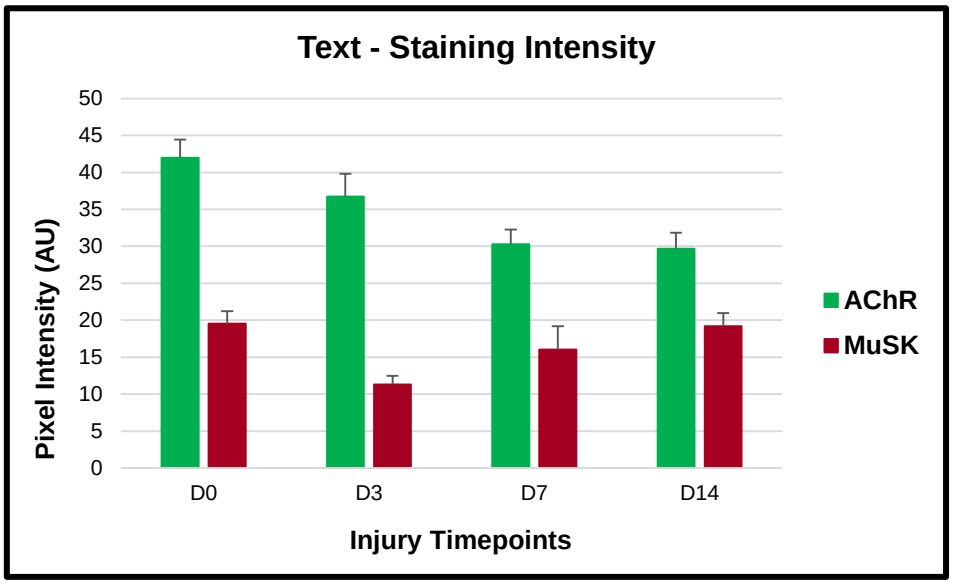

Figure I.4 TOP measurements for AChR and MuSK from IHC images pre- and post-injury.

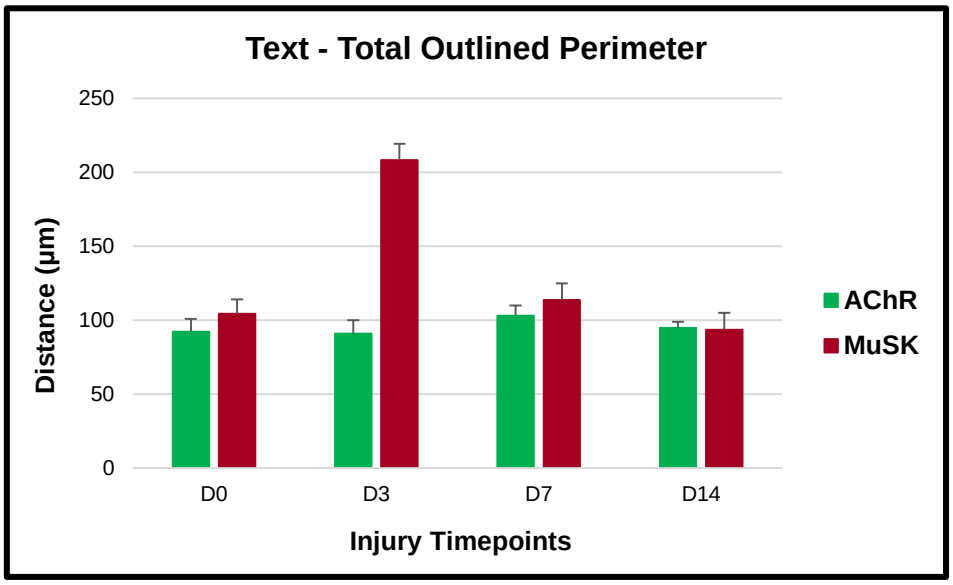

Figure I.5 Staining Intensity measurements for AChR and LRP4 from IHC images pre- and post-injury.

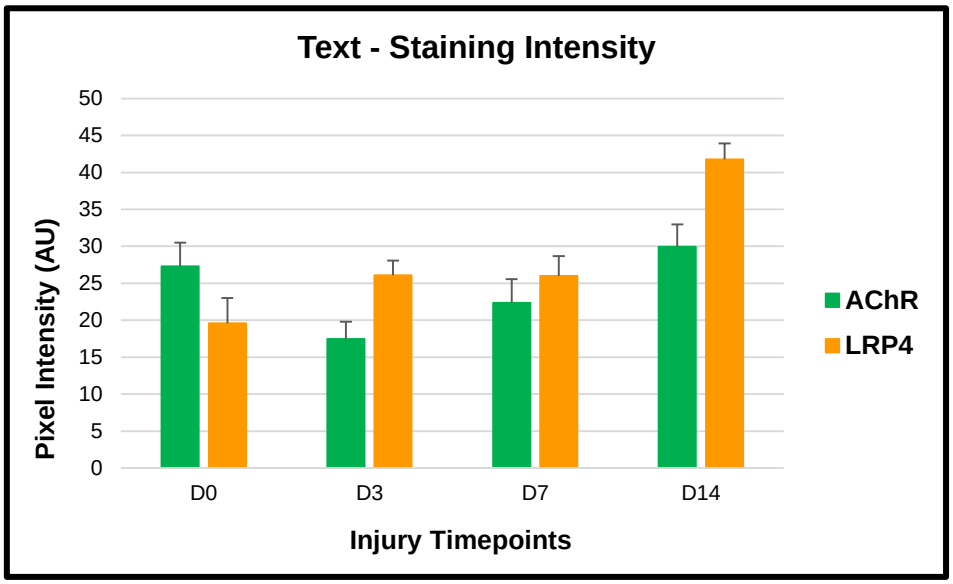

Figure I.6 TOP measurements for AChR and LRP4 from IHC images pre- and post-injury.

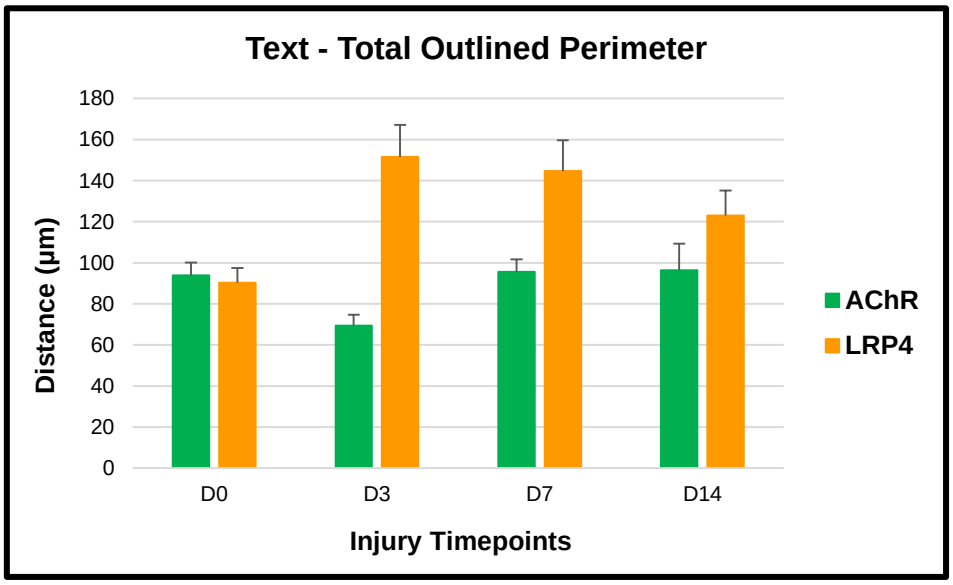

Figure I.7 Staining Intensity measurements for AChR and Dok7 from IHC images pre- and post-injury.

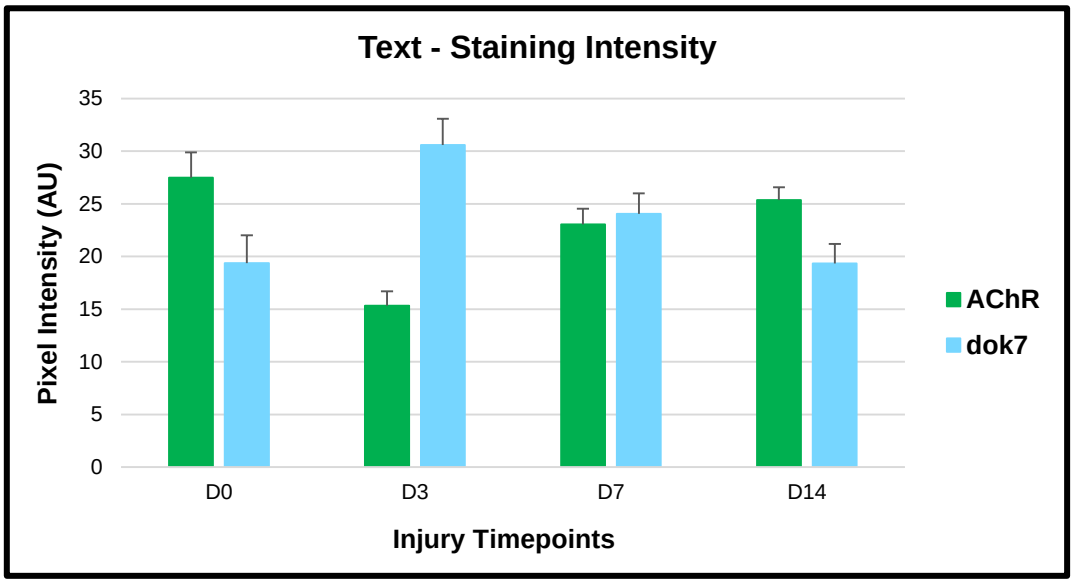

Figure I.8 TOP measurements for AChR and Dok7 from IHC images pre- and post-injury.